University of Alberta

Myelin Water Measurement in the Spinal Cord

by

Evan Patrick Minty ©

A thesis submitted to the Faculty of Graduate Studies and Research in partial fulfillment of the requirements for the degree of Master of Science

Department of Physics

Edmonton, Alberta
Spring 2005

Library and
Archives Canada

Published Heritage
Branch

395 Wellington Street
Ottawa ON K1A 0N4
Canada

Bibliothèque et
Archives Canada

Direction du
Patrimoine de l'édition

395, rue Wellington
Ottawa ON K1A 0N4
Canada

0-494-08118-X

Your file Votre référence
ISBN:
Our file Notre reference
ISBN:

NOTICE:
The author has granted a non-exclusive license allowing Library and Archives Canada to reproduce, publish, archive, preserve, conserve, communicate to the public by telecommunication or on the Internet, loan, distribute and sell theses worldwide, for commercial or non-commercial purposes, in microform, paper, electronic and/or any other formats.

The author retains copyright ownership and moral rights in this thesis. Neither the thesis nor substantial extracts from it may be printed or otherwise reproduced without the author's permission.

AVIS:
L'auteur a accordé une licence non exclusive permettant à la Bibliothèque et Archives Canada de reproduire, publier, archiver, sauvegarder, conserver, transmettre au public par télécommunication ou par l'Internet, prêter, distribuer et vendre des thèses partout dans le monde, à des fins commerciales ou autres, sur support microforme, papier, électronique et/ou autres formats.

L'auteur conserve la propriété du droit d'auteur et des droits moraux qui protège cette thèse. Ni la thèse ni des extraits substantiels de celle-ci ne doivent être imprimés ou autrement reproduits sans son autorisation.

In compliance with the Canadian Privacy Act some supporting forms may have been removed from this thesis.

While these forms may be included in the document page count, their removal does not represent any loss of content from the thesis.

Conformément à la loi canadienne sur la protection de la vie privée, quelques formulaires secondaires ont été enlevés de cette thèse.

Bien que ces formulaires aient inclus dans la pagination, il n'y aura aucun contenu manquant.

Canada

Abstract

Myelin is a modified lipid bilayer that ensheathes axons in the nervous system, where it potentiates nervous signal conduction, and consolidates axonal connections during neurodevelopment. Paradoxically, this latter function also limits nervous system plasticity after spinal cord injury, contributing to permanent disability. The desire to monitor the spatial-temporal characteristics of demyelination in the spinal cord, in the context of putative demyelinating neuroregenerative protocols or of pathological change in demyelinating diseases, have led to an interest in non-invasive image-based myelin quantification methods. We present one strategy: a magnetic resonance based measure that capitalizes on the characteristics of spin-spin (T_2) relaxation of water compartmentalized within tissue microstructure. In this study, techniques for quantifying the short T_2 "myelin water fraction" were successfully applied in the spinal cord both *in vitro* and *in vivo*. Results are discussed in terms of the physical limitations and biological significance of the measured values.

Acknowledgements

I've glanced at many-a-thesis, and have often thought about the mysterious transition that takes place when an academic, fresh (or maybe a little less than fresh) from their hard nosed pursuit of truth, takes a break from their rigor and sits down to express their gratitude to those that helped them along the way. This is the oscar acceptance speech of academia.

I no longer think on these things, as now I too, can truly appreciate a need for closure. This is not just retrospective gratitude, it is retrospective therapy.

"I'd like to thank…" my supervisors, Alex and Jack, whose patience in allowing a student to find his way, is matched only by my parents, who still get to hear about every new way I've found. My friends, who rallied me through completion, and procrastination, with equal enthusiasm. Everyone at the UBC high field MRI center; especially Thor, whose Matlab skills befit the Norse God that is his namesake. You all do T_2 like it is going out of style, instead of coming into style; and it will, the truth can only sit on the sidelines for so long. After all, the truth at low signal to noise, is still the truth.

And to those closest to me, for your discussions about everything other than T_2. You have played no small part in making magnetic resonance the lesser of the lessons learned in the last two years, and I'm a better person for having you in my life…

….. [cut off mid-speech by orchestra]

… "wait.. I'm not finished…"

Table of Contents

Chapter 1: Introduction 1
1.1 The Human Nervous System 1
1.2 The Human Spinal Cord 2
1.3 Myelin Structure and Function 5
    1.3.1 Myelin Structure 5
    1.3.2 Myelin's Role in Action Potential Propagation 6
    1.3.3 Myelin's Role in Nervous System Plasticity 9
1.4 Motivation 10
    1.4.1 Spinal Cord Involvement in Multiple Sclerosis 10
    1.4.2 Myelin and Spinal Cord Injury 12
Chapter 2: Principles of Magnetic Resonance Imaging 16
2.1 A Quantum Mechanical Account of Sample Polarization 16
2.2 Behaviour of **M** in Static and Time Varying Magnetic Fields 20
    2.2.1 Precession 20
    2.2.2 RF Excitation 23
    2.2.3 Relaxation 24
    2.2.4 Induction Signal Detection 26
2.3 The CPMG Pulse Sequence and True T_2 Measurement 27
2.4 Principles of Spatial Localization in MRI 28
    2.4.1 Slice Selection 29
    2.4.2 Frequency and Phase Encoding 30
    2.4.3 **k** Space 32
2.5 Myelin Water Measurement Using MRI 33
    2.5.1 T_2 Relaxation Analysis 34
    2.5.2 NNLS Analysis of Transverse Relaxation in CNS Tissue 37
Chapter 3: Materials and Methods 40
3.1 Human *in vivo* 40
    3.1.1 Subjects 40
    3.1.2 Apparatus 41
    3.1.3 Pulse Sequence and Data Acquisition 42
    3.1.4 T_2 Relaxation Analysis 47
3.2 Bovine *in vitro*: MRI 49
    3.2.1 Samples and Apparatus 49
    3.2.2 Pulse Sequence and Data Acquisition 49
    3.2.3 T_2 Relaxation Analysis 50

3.3 Bovine *in vitro*: NMR 50
3.3.1 Samples 50
3.3.2 Apparatus 50
3.3.3 Pulse Sequence and Data Acquisition 50
3.3.4 T_2 Relaxation Analysis 51
Chapter 4: Results 52
4.1 Bovine *in vitro*: NMR 52
4.1.1 T_2 Decay Curve 52
4.1.2 T_2 Distributions 54
4.2 Bovine *in vitro*: MRI 58
4.2.1 T_2 Decay Curves and Distributions 58
4.2.2 Myelin Water Fractions: Region of Interest Analysis 60
4.2.3 Voxel by Voxel Inversion 61
4.3 Human *in vivo* 63
4.3.1 Decay Curves and T_2 Distributions 63
4.3.2 Regional Changes in Myelin Water Fraction 66
4.3.3 Voxel by Voxel Inversion 72
Chapter 5: Discussion 76
5.1 Signal to Noise Ratio and IR-CPMG 76
5.1.1 SNR of *in vivo* Spinal Cord Quantitative T_2 79
5.1.2 SNR: Simulation and Reality 81
5.2 Accounting for Higher Myelin Water Fractions in the Spinal Cord 87
5.2.1 Non-Biolgical Factors 88
5.2.2 Biological Factors 93
5.3 Conclusions 107
References 109

List of Tables

Table	Description
1.1	Segmental Skin and Muscle Innervation
1.2	MR Correlates of Histology in Post Morten Spinal Cord
2.1	Nuclides commonly used in NMR
3.1	Parameter constraints employed in voxel thresholding
4.1	Spin Density and T_1 Values in White and Grey Matter
4.2	P values resulting from the application of two tailed Students t test
5.1	SNR measures in MR based quantitative T_2
5.2	Mean, Median, and standard deviations of Simulated MWF distributions
5.3	Myelin Water Fractions in the Brain and Spinal Cord
5.4	Characteristics of CSF ROIs used in a partial voluming simulation
5.5	Myelin yield in different CNS regions
5.6	Protein content in myelin in brain and spinal cord

List of Figures

Figure	Description
1.1	Change in diameter and associated white / grey matter distribution along the length of the spinal cord.
1.2	Lamellar arrangement of the myelin sheath
1.3	**a)** The form of the squid action potential (AP) and underlying total conductance *g*, sodium conductance *gNa* and potassium conductance *gK* as determined by the 1952 description by Hodgkin and Huxley. **b)** The first intracellular voltage clamp measurement of an action potential in squid axon.
1.4	Saltatory conduction enabled by the insulative properties of the myelin sheath increases nerve signal conduction velocity. Demyelination, shown below, disrupts this efficient signal transmission.
1.5	Photomicrograph of normal SC white matter (left), and an SC MS white matter lesion (right), clearly showing decreased myelin content in the latter (luxol fast blue stained). Bar = 10µm.
1.6	Percent axonal regeneration (as determined by a retrograde labelling experiment) in myelin suppressed vs. normal control regions. Percentage regeneration in the myelin suppressed group was 31.8±13.38%, while the control group showed 1.49±0.84% axonal regeneration.
2.1	Zeeman energy splitting. There are two possible energy states for a proton in a magnetic field due to the interaction of its magnetic moment and the external magnetic field B. For a large number of protons, the population ratio for the two states depends on their energy difference according to the Boltzmann distribution.
2.2	Two different orientations of a circular loop carrying current ε in a magnetic field **B**. In (**a**) the plane of the loop is orientated perpendicular to the magnetic field and the net torque is zero, while in (**b**) a net torque is applied about the loop center.
2.3	Time evolution showing post-excitation recovery of sample magnetization, in accordance with equations (2.24) and (2.25).
2.4	Characteristic appearance of a free induction decay curve. The sinusoid decays with time constant T_2^*.
2.5	(a) Dephasing of transverse magnetization due to field inhomogenaiety, signal loss is recoverable through the application of a 180° pulse along the y' axis. (b) A train of spin echoes form the basis for a CPMG experiment, through which true T_2 can be measured.
2.6	. Gradient echo 2DFT pulse sequence, and the inducution signals written as a 2DFT matrix.
2.7	(A) Non regularized T_2 distribution, where *s(T)* is represented as a sum of delta functions. (B) Regularized T_2 distribution, where additional constraints were placed on the squared sum of the amplitudes of the contributing delta potentials.
2.8	Typical T_2 distribution derived from Brain tissue, where the resolution of distinct spin spin relaxation times arising from water within the myelin bilayer, in the intra / extracellular space, and in cerebrospinal fluid is possible.
3.1	Observations of the dissemination of focal lesions along the entire length of the spinal cord in MS patients prompted the choice of a midline sagittal scan plane in the human study in light of its potential diagnostic value.
3.2	Poon Henkelman CPMG sequence (above), consisting of 2 crushers of varying amplitudes flanking each 180° composite $(90_x\text{-}180_y\text{-}90_x)$ refocussing pulse. The inversion recovery pulse, consisting of a non slice selective apodized sinc pulse at TI=1200ms, is not shown.
3.3	The composite pulse is designed to provide a more uniform 180° rotation across the slice, in the presence of field inhomogenaiety. This can be seen by comparing a 180° sinc pulse (a), to the composite $(90_x\text{-}180_y\text{-}90_x)$ pulse (b). Contour lines show the fraction of magnetization being refocused in the first echo.

3.4	Inversion recovery curve from CSF voxels. Heart and breathing motion, in addition to CSF flow, contribute to noise in the decay curve, making accurate determination of CSF T_1 from a sagittal spinal slice difficult. Literature values for CSF time were accordingly used in the determination of TI.
3.5	20 echo decay curve in human *in vivo* SC and CSF voxels, acquired using a modified fluid attenuating CPMG sequence. The rapid decay of CSF signal is fit to a short T_2 time and subsequently interpreted as myelin water.
4.1	T_2 relaxation decay curves from 3 NMR experiments on sample #1: echo times were 100μs for the experiment labeled AMP100, 200μs for the experiement labeled AMP200, and 400μs for the experiment labeled AMP400.
4.2	T_2 relaxation decay curves from 3 NMR experiments on sample #2: echo times were 100μs for the experiment labeled AMP100, 200μs for AMP200, and 400μs AMP400. Marked differences in the character of the decay curve during the experiment.
4.3	T_2 relaxation decay curves from 3 NMR experiments on sample #3: echo times were 100μs for the experiment labeled AMP100, 200μs for AMP200, and 400μs for AMP400.
4.4	Regularized NNLS T_2 distribution for spinal cord sample #1.
4.5	Regularized NNLS T_2 distribution for spinal cord sample #2.
4.6	Regularized NNLS T_2 distributions for spinal cord #3.
4.7	Representative decay curves from bovine SC. ROIs are shown (inset) in WM and GM regions. The "WM+GM" decay curve consists of data formed by addition of pixels in the WM and GM ROIs, while the 'Whole Spine" refers to an ROI encompassing the whole spinal cord.
4.8	T_2 distributions resolved from the decay curves shown in Figure 4.7 for ROIs in GM, WM, GM+WM, and whole spine.
4.9	ROI analysis of fresh Bovine SC. (a) 30ms echo image, (b) WM ROIs used in the analysis, (c) myelin water fractions for the 45 WM ROIs and the 10 GM ROIs, (d) distribution of white matter values, (e) distribution of GM values. Mean myelin water fractions (±Standard error) for the two regions was .300 (±0.006), and 0.082 (±0.004).
4.10	Myelin water fractions for pixels within defined WM and GM ROIs in transverse sections of fresh bovine SC. Two distributions are seen for grey matter and white matter respectively. Mean (±SE) values for white matter voxels was 0.269 (±0.001), while for grey matter voxels it was 0.080 (±0.002).
4.11	Myelin water map created from bovine spinal cord. Grey matter regions, seen as hyperintense on the 30ms echo image shown in (a), are clearly resolved as having a lower myelin water fraction in (b).
4.12	Selective visualization of intermediate myelin water fraction values reveals the effects of partial voluming on myelin water content distributions.
4.13	Signal from a Brain CPMG vs. IR prepped spine CPMG experiment. The inversion recovery pulse results in significant costs in signal to noise.
4.14	Relative signal in the IR-CPMG with respect to conventional CPMG, expressed as a function of voxel grey matter content.
4.15	Regularized (a), and non regularized (b) T_2 distributions obtained from NNLS inversion of decay curves (c) from the ROIs shown above. The top distributions / decay curve correspond to the most rostral ROI, and they descend through progressively caudal regions of interest.
4.16	Myelin water fractions measured in progressively caudal regions of interest adjacent to the listed vertebrae. Varations in myelin water content follow a pattern consistent with the physiological distribution of white matter, as determined by the areal fraction of white matter on myelin stained micrographs averaged from neuroanatomy textbooks.
4.17	Scatterplot showing IR-CPMG myelin water fraction versus the areal white matter fraction as measured in tranverse myelin stained photomicrographs. A weighted linear regression found a significant correlation between the two, with R^2 of 0.75, at $P < 0.00006$.
4.18	Average myelin water fractions, binned according to regional differences as determined by t-test results. Error bars indicate standard error.

4.19	10ms echo images from cervical (a), thoracic (b), and lumbar (c) 32 echo acquisitions. Corresponding myelin maps are shown in (d),(e), and (f) respectively.
4.20	Superposition of a myelin map from a lumbar acquisition onto figure 1.1, demonstrating sensitivity of voxel by voxel inversions to reduced myelin content in the lumbar enlargement.
4.21	**(a)** Axial acquisition at vertebral C7 demonstrating sensitivity to myelin content in a spinal cord transverse plane in humans *in vivo*., as can be seen through a comparison with a reference histological transverse slide from the same area **(b)**.
5.1	Incompletely resolved T_2 distribution from human spinal cord *in vivo* showing the parameters T_{2a}, T_{2b}, and h_{dip} employed in the definition of R and S (equations 5.1,5.2)
5.2	The Rice distribution, shown plotted as a function of μ/σ. In the low signal limit the Rice distribution can be approximated by the Rayleigh distribution, while in the high signal limit μ/σ it is approximately Gaussian distributed.
5.3	Distribution of myelin water fraction (0-40ms) in simulated decay curves at different SNR.
5.4	Distributions of Relative peak separation, S, at different SNR levels. There is a tendency towards greater peak separation at lower SNR.
5.5	Example of the distribution in R measured at low SNR. The plotted line shows the cumulative percentage of T_2 distributions at the listed R values, and can be used as a measure of the proportion of spectra in which a separate myelin water T_2 component is being resolved.
5.6	Cumulative percentage of R values in resolved T_2 distributions from simulated decays.
5.7	Distribution of Peak Resolution, R in T_2 spectra in human spine *in vivo*. Shown for comparison is the data (cumulative % in R values) from the simulation study at 100 SNR, which agrees qualitatively with the measured distribution.
5.8	Relative Separation, S, of resolved T_2 distributions in human spine *in vivo*. A greater spread in S values is seen about a mean of 1.44 than observed in simulation studies.
5.9	Distribution of myelin water fractions in human spine *in vivo*. Mean ± SD was 0.22 ± 0.06.
5.10	(a) Calculated fractional white matter signal in voxels with different GM content. In all voxels between the limiting grey matter compositions, the measured fractional WM signal in IR CPMG (dashed curve) is be greater than in a CPMG experiment (solid curve). The difference between the two experiments (IR-CPMG – CPMG) is plotted in (b).
5.11	Binned myelin water fraction measurements adjusted for T_1 effects. Percent overestimate varies with the areal white matter fraction, which is also plotted. T_1 adjusted white matter values assumed a GM MWF of zero.
5.12	Myelin water fractions resolved in partial volumed CSF and SC ROIs. PV1 corresponds to a non-contiguous ROI comprising signal from CSF1, and of the SC at the indicated physiological level.
5.13	Calculated *g* ratios, and corresponding areal fractions from a study on spinal cord fiber morphometry.
5.14	Calculated areal ratios in human medullary pyramid relative to those calculated in the spinal cord of lower vertebrates.
5.15	Fibre diameter distribution in different white matter areas of the bovine nervous system. Diameter μ is in microns. Measured myelin water fractions from referenced studies that have examined that area are shown inset.
5.16	Data simulated using a simple 2 pool model. (a) with a T_{cr} of 10 000; measured distribution characteristics are close to expectations (MWF=19.71). (b) When T_{cr} is reduced by a factor of ten, T_2 peaks broaden and shift to the left, and the short T_2 peak decreases in relative magnitude (MWF=14.03).
5.17	Micrographs from feline spinal cord (left) and corpus callosal tissue (right) taken at the same magnification, showing the difference in fiber size distributions between the two white matter structures.

List of Symbols and Abbreviations

Symbol / Abbrev.	Description
ℓ	Orbital angular momentum
γ	gyromagnetic ratio
χ^2	Chi Square Misfit Value
AM	Arithmetic Mean T_2
CNS	Central Nervous System
CPMG	Carr-Purcell Meiboom Gill
CSF	Cerebrospinal Fluid
DN	Voxel Proton Density
EM	Electromagnetic
fMRI	Functional Magnetic Resonance Imaging
FOV	Field of View
FT	Fourier Transform
g	Fiber G ratio
GalC	Galactocerebroside
GM	Grey Matter
$\mathbf{H}$	NNLS Regularizing Matrix
$\mathbf{I}$	Nuclear spin
IR-CPMG	Inversion Recovery CPMG
$\mathbf{j}$	Total anglular Momentum for a nucleon
$\mathbf{k}$	Reciprocal space vector
kD	Kilo Dalton
kHz	Kilo Hertz
MBP	Myelin Basic Protein
MS	Multiple Sclerosis
MTR	Magnetization Transfer Ratio
MWF	Myelin Water Fraction
NEX	Number of Averages
NNLS	Non Negative Least Squares
PD	Proton Density Weighted Image
PLP	Proteolipid Protein
PNS	Peripheral Nervous System
PP-CPMG	Projection Presaturation CPMG

PV	Partial Voluming
R	T_2 Peak Resolution
R^2	Coefficient of determination
RF	Radio Frequency
ROI	Region of Interest
s	Spin angular Momentum
S	Relative T_2 Peak Separation
SC	Spinal Cord
SCI	Spinal Cord Injury
SDS PAGE	sodium dodecyl sulfate-polyacrylamide gel electrophoresis
SNR	Signal to Noise
SR-CPMG	Saturation Recovery CPMG
T	Tesla
T_1	Spin lattice relaxation time
T_2	Spin-spin relaxation time
TE	Echo Time
TI	Inversion Time
TR	Repetition Time
WM	White Matter

Chapter 1: Introduction

1.1 The Human Nervous System

Animal nervous systems require a remarkable degree of complexity to perform three overlapping functions of sensory input, integration, and motor output. This complexity is reflected by the Nervous System's anatomical intricacy: a single cubic centimeter of the human brain can contain millions of nerve cells (neurons) [1], each of which could potentially be associating with thousands of others. This connectivity acts to create neural networks with a processing capacity that make today's computing technology seem primitive by comparison. Indeed, considering it consists of approximately 100 billion nerve cells each relying on a supportive network of metabolizing, insulating, and phagocytosing glial tissue, the vertebrate nervous system operates in remarkable synchrony to effect responses to external and internal stimuli.

Neurons are highly differentiated cells specialized to receive, conduct, and transmit nerve impulses, also called action potentials. Despite the wide range in nervous cell morphology, nerve cells share some common characteristics. Two types of processes extend from the cell body: dendrites are the receiving (afferent) processes, they conduct cell signals to the cell body. Axons are the transmitting (efferent) processes, conducting signals away from the cell body. The terminals of an axon establish contact with other neurons or with an effector organ at a site called the synaptic junction [1]. At the synaptic junction, electrical or chemical synapses occur between the axon of the presynaptic cell to a dendrite of a post synaptic cell, or in case of motor neurons, from the axon to an effector organ.

The nervous system is divided into two parts based on anatomical and functional features: The Peripheral Nervous system (PNS), consists of the cranial and spinal nerves and their ganglia. The PNS transmits sensory information to the Central Nervous System (CNS) from sensory receptors, and transmits motor signals from the CNS to effector organs. The Central Nervous System, meanwhile, consists of a bilaterally symmetric group of structures in the brain and spinal cord [2]. The spinal cord runs down the neck and back inside a protective column of vertebrae, receiving sensory information from and transmitting motor commands to the PNS. The brain, at the superior end of the spinal cord, contains centers used for the complex integration of homeostasis, perception, movement, and intellect [2].

Protecting the CNS are three layers of connective tissue, called meninges, and the surrounding cerebrospinal fluid (CSF). CSF is produced in the brain by the filtration of blood, it circulates through the ventricles, between the meninges, and in the spinal column to serve both protective (shock absorbing) and circulatory (nutrient, hormone, and white blood cell transport) functions. The presence and motion of CSF can have important implications in magnetic resonance studies.

Central nervous system tissue exhibits characteristic distributions of grey and white matter, as can easily be appreciated in macroscopic sections through both the brain and spinal cord. The basis of this distinction lies in axon morphology. A lipo-protein membrane, myelin, ensheathes some axons giving rise to the glistening white appearance of white matter (WM). Unmyelinated nerve cells, usually embedded in a network of nerve processes [2], retain their native grey colour and form CNS grey matter (GM). The functions and properties of Myelin are of particular relevance to this thesis and merit elaboration; we defer this discussion to a subsequent section of this chapter.

1.2 The Human Spinal Cord

The spinal cord (SC) is a 0.5m long cylindrical part of the CNS that occupies the upper two thirds of the vertebral canal. It serves as a liaison for impulses between the brain and the peripheral nerves, and contains numerous intrinsic neuronal circuits that define several of spinal reflexes. The diameter of the cord varies with the number of outgoing and incoming peripheral nerve fibers: those parts that innervate the upper and lower limbs form spindle-shaped enlargements[1], as can be seen in figure 1.1.

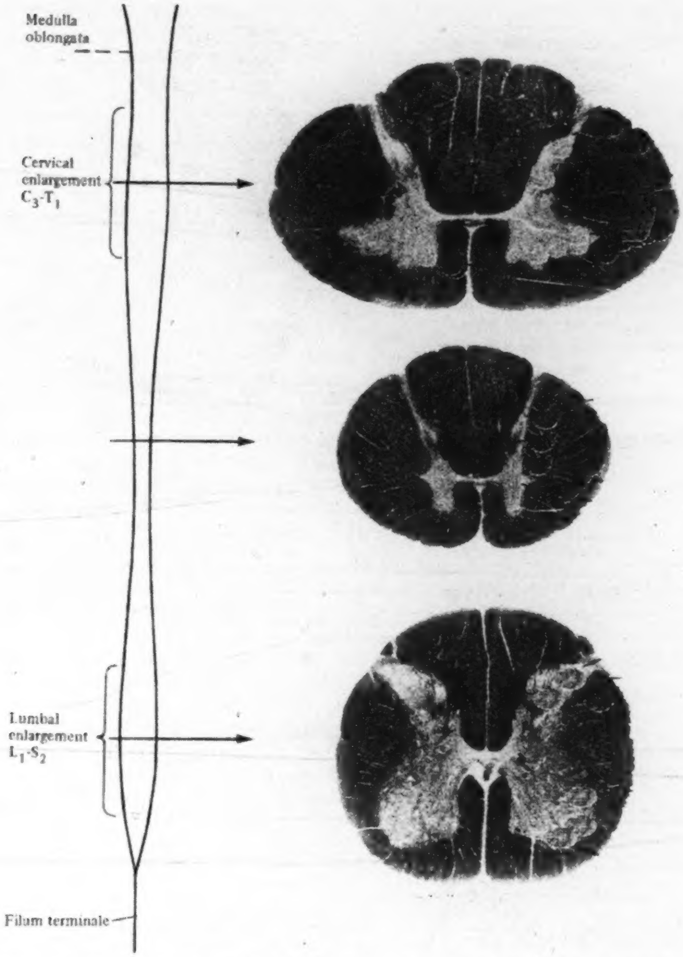
Medulla oblongata
Cervical enlargement C_3-T_1
Lumbal enlargement L_1-S_2
Filum terminale

Figure 1.1 Change in diameter and associated white / grey matter distribution along the length of the spinal cord. Adapted from [1].

As illustrated in figure 1.1 transverse axial sections reveal the characteristic butterfly distribution of grey matter within the spinal cord. Moreover, variations of this general distribution, and therefore the relative GM / WM content, can be observed depending on the caudal section examined. The total amount of white matter decreases in progressively caudal sections, as the long ascending and descending pathways contain fewer axons at lower levels of the spinal cord [1]. However, the *relative* proportion of grey matter in the spinal cord does not reflect this monotonic decrease in absolute white matter content. The majority of neurons in SC GM are interneurons (also termed associated neurons, or intercalated neurons), which are not directly synapsed with sensory or effector organs, but instead serve as intermediaries in relationships between spinal motor and sensory mechanisms. The mentioned diameter enlargements in those areas of the SC responsible for hosting efferent and afferent processes that innervate the extremities also accommodate increased 'cross-talk', reflected in an enlargement of the grey matter butterfly. This intercalation in these areas is crucial to the operation of a spinal reflex: a rapid, unconscious, programmed response to a specific stimulus.

Ventral and dorsal roots come together in the intervertebral foramen to form a spinal nerve; thirty one pairs of these spinal nerves innervate the body in an orderly fashion. The peripheral distribution of the spinal nerves reflects a segmental innervation, whereby each spinal nerve is composed of fibers that innervate one segment (or region) of the skin, muscles or connective tissue of the body [1]. A summary of some key sensory innervations of the skin (dermatomes) and muscles is offered in table 1.1.

Table 1.1: Segmental Skin and Muscle Innervation

Skin Innervation	Muscle Innervation
C3 Neck	C1-C4 neck muscles
C5 Deltoid Region	C3-C5 diaphragm
C6 Radial forearm and thumb	C5-C6 biceps
C8 Border of hand and little finger	C5-C8 muscles of the shoulder joint
T4-T5 nipple	C7-C8 triceps and muscles of the forearm
T10 umbilicus	C8-T1 intrinsic muscles of the hand
L1 groin	T2-T12 axial musclature, muscles of respiration
L3 knee region	L1-L2 thigh flexors
L5 dorsal side of foot and great toe	L2-L3 quadriceps femoris
S1 lateral side of foot and little toe	L5-S1gluteal muscles
S3-S5 genito-anal region	S1-S2 plantar flexors of the ankle
	S3-S5 bladder, sphincters, external genital organs.

1.3 Myelin Structure and Function

Myelin is an extended, modified plasma membrane that ensheathes axons in nervous system white matter. Deposited by oligodentrocytes in the CNS and Schwann cells in the PNS, electron microscopy studies reveal that the sheath is composed of multiple layers, wound radially about the long axis of the axon [3]. The structure and molecular composition of myelin is relevant to both the neurophysiological and the NMR characteristics of myelinated tissue, and is worthy of some description.

1.3.1 Myelin Structure

In the CNS, axons are myelinated in multiple segments by multiple oligodentrocytes, which leave a small, unmyelinated region (called the Node of Ranvier) between each myelinated portion. The lipid composition of adult CNS myelin involves cholesterol, phospholipid, and sphingolipid in a ratio of 4:3:2. Cholesterol and glycolipids have higher concentrations in the outer layers of the myelin sheath, giving their polar moeities greater exposure to the extracellular environment [3]. Phospholipid, the most abundant in myelin conferring a weakly polar ethanolamine head group, is located exclusively on the cytoplasmic side of the membrane due to its relative hydrophobicity. Approximately 50% of the hydrocarbon chains in the lipids are unsaturated (i.e. have one or more double bonds); the resulting 'kinks' in the hydrocarbon chains increase membrane fluidity in the area between the outer and inner membrane layers.

The two major structural proteins of myelin are Myelin Basic Protein (MBP) and Proteolipid Protein (PLP). MBP, while having a highly conservative amino acid sequence, undergoes different degrees of post-translational modifications to produce several forms of MBP molecules [4]. MBP is thought to play a major role in myelin compaction. PLP, meanwhile, is thought to help stabilize the myelin membrane through self-association. Together, PLP and MBP are responsible for the periodic lamellar arrangement of the myelin sheath, as shown in figure 1.2. Both the chemical features of myelin lipid and protein constituents, and the macrostructural arrangement of myelinated tracts within the SC are relevant to magnetic resonance properties of the tissue. We defer this discussion to a subsequent section of this thesis, where they are highlighted in the context of the results of this study.

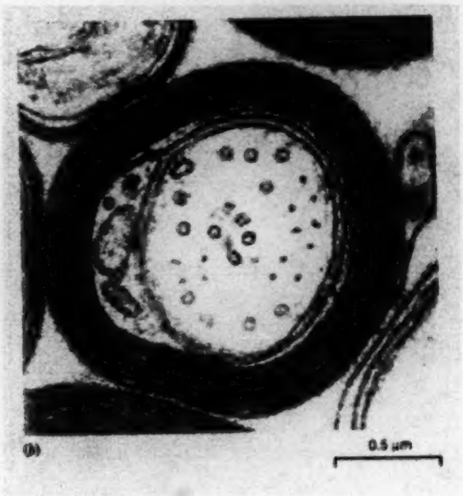

Figure 1.2 Lamellar arrangement of the myelin sheath. Adapted from [4].

1.3.2 Myelin's Role in Action Potential Propagation

The primary role of myelin in nervous system tissue is to increase the propagation velocity of action potentials. To put these insulative properties of myelin in context, a brief description of action potentials in excitable cells is required.

All living cells have an electric potential across their plasma membranes, arising from the differences in the ionic composition of the intracellular and extracellular fluids, the selective permeability of the plasma membrane to ions, and to active transport processes (the sodium-potassium pump). Potential difference across the membrane of most animal cells ranges from –50mV to -100mV (the extracellular fluid is assumed to be at a reference ground potential of zero). The net effect of this voltage and concentration differential is the creation of an electrochemical gradient,

$$\Delta G = RT\ln(C_{in}/C_{out}) + ZFV \tag{1.1}$$

Where R is the ideal gas constant, T is the absolute temperature, C_{in} and C_{out} are the intracellular and extracellular ion concentrations, Z is the ion charge, V is the potential difference across the membrane, and F is the Faraday constant (the amount of electrical charge per mole of elementary charge; equal to 9.65E4 C/mol).

Exciteable cells in the nervous system (muscle and nerve cells) have the ability to use this electrochemical gradient to produce a characteristic, transient membrane depolarization called an action potential. The propagating wave of depolarization arises because the plasma membranes of neurons contain voltage gated ion channels, so named because these channels express different permeabilities to their respective ions at different membrane potentials.

After being initiated by a sensory event creating a local depolarization above a threshold level, the action potential is regenerated by neighbouring voltage gated channels to allow the transmission of the signal along the neuron. Given sufficient depolarization in the surrounding cytosol, activation gates of the sodium channels open, allowing Na^+ to flow into the cell, down it's electrochemical gradient. This influx continues until the effect of the membrane potential (to resist continued Na^+ influx) equals the effect of the sodium concentration gradient (to cause more Na^+ to flow inward) [5]. At this point, ΔG=0, and equation (1.1) can be rearranged to give

$$V_{eq} = -(RT / ZF)\ln(C_{out} / C_{in}) \tag{1.2}$$

Where V_{eq} is the equilibrium potential, which can range from +50mV [2], to +70mV [1]. This change in potential opens the voltage gated potassium channels, allowing K^+ to flow out of the cell, restoring the negative potential of the intracellular environment. Initial sodium and potassium concentrations are then restored by the action of the sodium potassium pump, which removes 3 Na^+ ions from the cytosol in exchange for 2 K^+ from the extracellular fluid. This net intracellular gain of a positive ion occurs at the cost of one molecule of Adenosine Triphosphate (ATP). The hydrolysis of ATP is the ubiquitous energy currency of metabolic processes; yielding $\Delta G° \doteq -7.3$ kcal/mol ATP [6], or 0.32 eV per ATP / ADP conversion. The form and propagation of the action potential and its dependency on underlying sodium and potassium conductances (figure 5.3a) was first described phenomenologically by Hodgkin and Huxley [7] through intracellular measurements on squid axon (figure 5.3b).

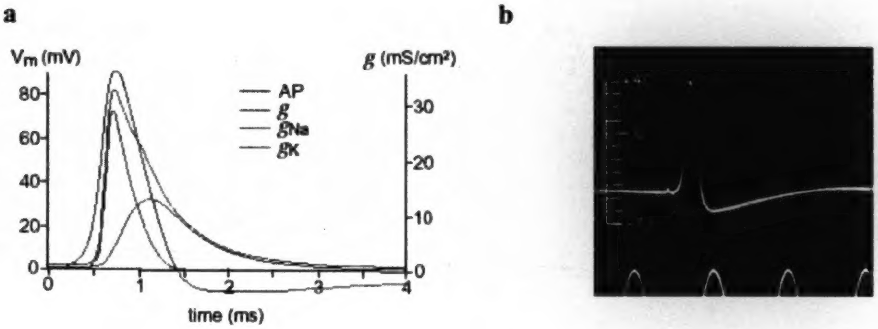

Figure 1.3 a) The form of the squid action potential (AP) and underlying total conductance *g*, sodium conductance *gNa* and potassium conductance *gK* as determined by the 1952 description by Hodgkin and Huxley [7]. **b)** The first intracellular voltage clamp measurement of an action potential in squid axon [7]. Adapted from [8].

In unmyelinated axons, action potentials require continual regeneration due to the effects of current leaks across the axonal membrane. Once given the added insulation of myelin, however, the generated electrical impulse cannot flow radially through the cell membrane, and instead the ion current flows along the axon. Nodes of Ranvier, containing a high concentration of Na^+ activation channels, create a rapid influx of sodium at each node of Ranvier to allow the action potential to 'jump', unattenuated, from one node to the next in a process called 'saltatory conduction'. Saltatory Conduction velocities (100 m/s) are far faster than those afforded to unmyelinated axons (0.4 m/s); the importance of this added efficiency is evidenced by the pathologies of demyelinating diseases such as Multiple Sclerosis and Schizophrenia, where localized lesions can have devastating effects.

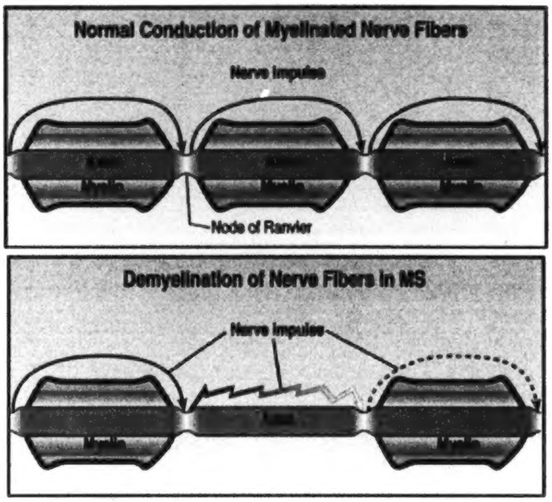
Normal Conduction of Myelinated Nerve Fibers
Nerve Impulse
Axon
Myelin
Node of Ranvier
Demyelination of Nerve Fibers in MS
Nerve Impulse
Axon
Myelin

Figure 1.4 Saltatory conduction (above), enabled by the insulative properties of the myelin sheath, increases nerve signal conduction velocity. Demyelination, shown below, disrupts this efficient signal transmission.

1.3.3 Myelin's Role in Nervous System Development, Maturation, and Plasticity

Although myelin's primary function in the nervous system is the acceleration of action potential propagation, additional functions of the insulating membrane have been elucidated. In the context of SCI, the inhibitory properties of myelin and myelin-associated molecules on neurite outgrowth are of interest.

Neurites are newly forming collateral extensions of axons, which initiate their extension in a form termed a *'growth cone'*. Growth cone collapse resulting from contact with CNS myelin was first noted over a decade ago [9]. SDS PAGE studies have since revealed two myelin associated macromolecules, NI-35 and NI-250 (35kD and 250kD respectively) that have substantial inhibitory activity towards growth cone extension [10]. Both of these factors are expressed in all myelinated regions of the CNS.

This inhibitory activity of myelin on neurite outgrowth suggests the appearance of CNS myelin may compart a function in neuro-development. Moreover, the temporal coincidence between the onset of myelination and the completion of primary axonal growth suggests that myelin plays its major neuro-developmental role in the stabilization of previously formed axonal connections; effectively 'hardwiring' the nervous system to the desired configuration. This hypothesis is supported by findings that axonal sprouting within the adult CNS occurs more readily in lightly myelinated regions (e.g. the substantia gelatinosa of the spinal cord), while heavily myelinated regions only express axonal sprouting prior to myelination [11].

1.4 Motivation: Why Measure Spinal Cord Myelination?

Myelin's multiple roles in neurological function lead to a two-fold motivation for undertaking a study to non-invasively measurement it in the spinal cord. Firstly, it is hoped that the application of quantitative MR based measures of myelination might contribute to the understanding of demyelinating diseases in general, and Multiple Sclerosis in particular. Secondly, myelin's recently elucidated role in neurodevelopment has led to putative neuroregenerative therapies that would benefit from a non invasive measure of spinal cord myelination. Motivations on both fronts, with respect to current developments in both fields, are clarified in the sections below.

1.4.1 Spinal Cord involvement in Multiple Sclerosis

Multiple Sclerosis is the most common chronic disabling disease of the central nervous system in young adults, affecting up to 1 / 1000 persons in the western world [12]. The disease is characterized by focal areas of edema, inflammation, demyelination, and axonal loss, all of which stem from an autoimmune response to CNS myelin in the brain, spinal cord, and optic nerve. A histological section demonstrating demyelination in a spinal cord lesion is shown in figure 1.5.

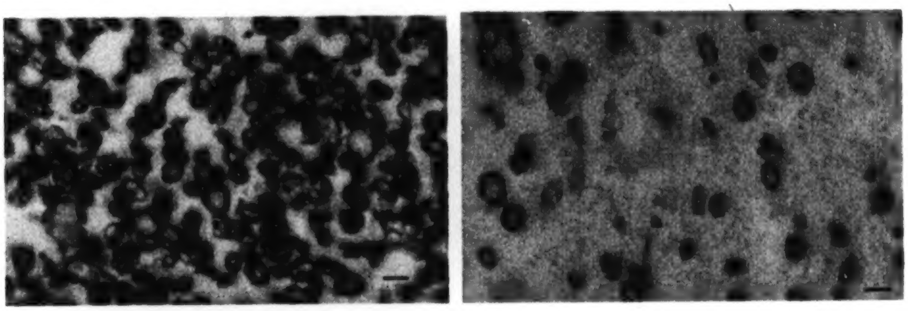

Figure 1.5 Photomicrograph of normal SC white matter (left), and an SC MS white matter lesion (right), clearly showing decreased myelin content in the latter (luxol fast blue stained).
Bar = 10μm. From [13].

Diagnosis is primarily based on clinical findings, laboratory and paraclinical tests. The McDonald criteria [15], the most recently published diagnostic criteria for MS, has for the first time recognized SC MRI as a paraclincal test for MS. MS is a diffuse disease, and accordingly the McDonald criteria requires that MRI findings demonstrate a dissemination in space of focal lesions: the identification of two lesions in the brain is needed for conclusive diagnosis, and the substitution of one SC lesion for one brain lesion is permissable.

However, several authors have suggested that SC MRI can make important contributions to the differential diagnosis of MS [13, 16-20], beyond those that are recognized by current diagnostic standards. In a recent study of 104 recently diagnosed MS patients, it was noted that the criteria for dissemination in space, as outlined in the McDonald criteria for the brain, was met in only 66.3% of patients until the inclusion of SC MRI, at which point over 84% of patients could be definitively diagnosed [21]. In the same study, the diffuse nature of MS was also shown to manifest itself in spinal cord lesion load, giving a distribution of T_1 and T_2 enhancing lesions along the entire imaged length (C2 to T12) of the spinal cord. The case for inclusion of SC imaging in any diagnostic workup for MS is perhaps made most convincingly by considering that in 5% of patients with clinically definite MS, the brain MRI is *normal* [19]. Thorpe *et al* showed that in a study of 20 such patients, all had spinal MRI abnormalities consistent with MS [22].

This increasingly recognized clinical importance of the spinal cord would be for naught without with technological advancements to make SC imaging feasible. Indeed, the popularization of multi-array surface coils [23], anatomically optimized RF coil design [24], and higher clinical field strengths have enabled faster, more reliable SC MRI diagnostics.

The diagnostic capabilities of MRI extend beyond lesion identification however. Several magnetic resonance techniques have been developed to investigate tissue microstructure, effectively probing tissues at spatial resolutions far smaller than a voxel. Many of these techniques are aimed at quantifying myelin, as its degradation in the central nervous system is a central feature of neurological diseases such as Multiple Sclerosis. Recent interest in the clinical relevance of the spinal cord to MS has accordingly resulted in some of these techniques being applied to the area. In one recent study, Mottershead *et al* examined post mortem SC of patients with MS, correlating quantitative techniques (T1 and T2 relaxation measurements, magnetization transfer, diffusion measurements) with histopathological measures (axonal density, myelin area, cellularity) [13]. Their results are summarized in table 1.1.

Table 1.1 MR Correlates of Histology in Post Mortem Spinal Cord

Histological Measure	Correlation		
	Strong	Moderate	Weak
Axonal Density	T1 (-), MTR (-), PD (-), SDI (+)	T2 (-)	mean ADC (-)
Myelin Area	T1 (-), PD (-), MTR (+), T2 (-) SDI (+)	mean ADC (-)	
Cell Count		T1 (+), ADC (+)	

Table 1.1 Summary of results of a study on Post Mortem SC by Mottershead *et al*. The correlation type (postive / negative) is shown in brackets. T1 and T2: longitudinal and transverse relaxation times; MTR: magnetization transfer ratio, a measure of magnetization exchange with semi-solid protons; PD: water proton density; ADC: apparent diffusion coefficient and SDI: diffusion standard deviation index are measures of diffusion anisotropy. Table adapted from results given in [13].

The T_2 measurements made in the Mottershead study consisted of monoexponential fits to two acquired echoes (points along the multi-exponential decay of the MR signal), a technique with established shortcomings in accurate T_2 measurement [25-27]. This present study aims to employ a technique in MR based myelin measurement employing the 32 echo T_2 relaxation derived 'myelin water fraction' – that fraction of total signal posed to originate from water trapped within the myelin bilayer. These measurements would expand preliminary observations made in humans [28-30] and rats [31] *in vivo* by characterizing the myelin water fraction along the entire length of the spinal cord in humans, with consideration given to the technical limitations to imaging in this physiological locale through supporting *in vitro* work. With respect to MS, it would be a valuable contribution towards characterizing pathology of demyelinating diseases in the spinal cord, an increasingly recognized contributor to MS disability.

1.4.2 Myelin and Spinal Cord Injury

Over 200 000 people in North America are afflicted by some disability associated with Spinal Cord Injury (SCI) [32]. While the narrow spinal cord is relatively well protected by surrounding vertebrae, severe mechanical trauma can cause the vertebrae to compress or axotomize (sever) the long neural tracts. Paralysis is the most recognizeable effect of severe SCI; it results from an inability of the body to effect repair of the damaged nerve tracts. Indeed, given the remarkable ability of the body to heal itself, the lack of plasticity observed in response to SCI is shocking: less than 1% of SCI patients recover prior to discharge [33]. This is indicative not only of an inability to effect repair, but a lack of redundancy within neuronal circuits, i.e. insufficient overlap in spinal intercalation for the missing functions to be taken over by surviving tracts [34]. Paralysis effectively restricts patient sensation and mobility according to the level of injury: persons with tetraplegia (51.6% of SCI patients) have sustained injuries to one of the eight cervical segments of the spinal cord; those with paraplegia (46.3% of SCI patients) have lesions in the thoracic, lumbar, or sacral regions [33].

It is estimated that the annual incidence of SCI, not including those who die at the scene of the accident, is approximately 40 cases per million population in North America, or approximately 10,000 new cases each year. While the costs in quality of life and life expectancy of these patients is immeasurable, a price tag can be ascribed to the medical requirements of SCI patients. These lifetime costs vary greatly according to the severity of injury, and represent a tremendous financial burden to patient and society alike. The estimated lifetime cost of high (C1-C4) tetrapalegia, for example, runs in excess of US $2,000,000 [32].

The vertebrate CNS demonstrates a very limited capacity for SC repair following injury, suggesting the absence of growth promoting factors or presence of neurite growth inhibitors relative to the developing CNS [11]. Studies of developing chick embryos have shown that spinal transection prior to day 13 (E13) of the 21 day developmental period results in relatively complete axonal regeneration and functional recovery, while transection after E13 (which coincides with the developmental onset of myelination) results in little / no regenerative activity or functional recovery [9]. Further studies in embryonic avian systems have shown that delaying the onset of myelination through immunological methods extends the permissive period for axonal regeneration and functional CNS repair [35].

More recent reports have indicated that similar immunological protocols can create a transient demyelination in adult rat spinal cord [36], as well as other model systems. This immune system medidated demyelination can be achieved through intraspinal infusion of serum complement proteins and myelin specific anti-Galactocerebroside antibodies (Galactocerbroside, GalC, is a major lipid constituent of the myelin membrane). Experimental models involving transected adult rat spinal cord have shown that this immunological myelin removal facilitates axonal regeneration, as determined by retrograde tract labelling techniques [36]. Not only does this further testify to the inhibitory activity of myelin on axonal sprouting, it indicates that the adult vertebrate nervous system retains an inherent plasticity which enables axonal regrowth in the presence of a favourable extracellular environment. Figure 1.6 illustrates the dramatic effects demyelination has on percent regeneration of axotomized neurons.

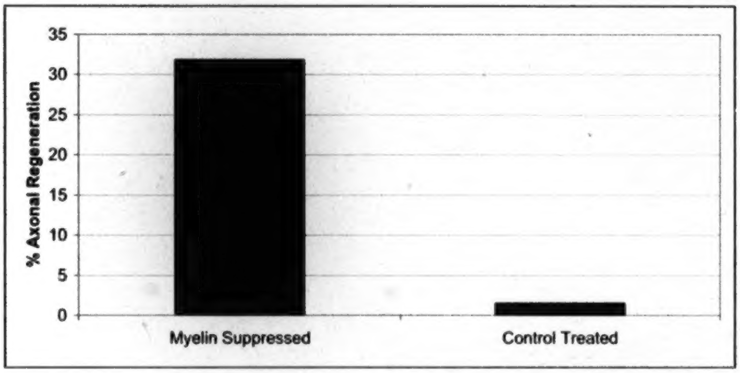

Figure 1.6 Percent axonal regeneration (as determined by a retrograde labelling experiment) in myelin suppressed vs. normal control regions. Percentage regeneration in the myelin suppressed group was 31.8±13.38%, while the control group showed 1.49±0.84% axonal regeneration. Adapted from [36].

The anti-GalC/serum complement protocol developed by iCORD (International Collaboration on Repair Discoveries, UBC) is slated for human clinical trials in the near future. Therefore, non-invasive techniques for the assessment of the spatial and temporal characteristics of the induced transient demyelination are of great interest.

Challenging physiological attributes of spinal column tissue have provided obstacles to SC imaging, let alone quantitative relaxation studies. While greatly benefiting from the development of phased array RF coils [23], motions of CSF, blood, respiration, swallowing, and other patient movement conspire to create artifactual complications [37].

The objective of this current work was to show that novel combinations of hardware, pulse sequences, and data analysis methods could lead to the acquisition of viable relaxation data and physiological reasonable measurements of myelin water, building on our earlier report on the first such measurements made *in vivo* [28]. These results would further validate the use of the 'short T2 myelin water component' as a measure of myelination.

The long term vision of this study takes on additional significance: it represents a departure from the use of methods in MR myelin quantification in the characterization of devastating disease pathology, and takes steps towards their implementation as a window to an amazing healing process. Methods in myelin quantification in MRI could eventually help refine the best protocols for demyelination in a therapeutic regimen for neural regeneration, if their reliability in measuring spinal cord myelin can be demonstrated. It is hoped that this thesis might make a measureable contribution towards these ends, offering those who undertake that study the benefiet of hindsight with respect to applying these techniques *in vivo*.

Chapter 2: Principles of Magnetic Resonance Imaging

Since the characterization of Nuclear Magnetic Resonance phenomena by Purcell [38] and Bloch [39] in 1946, the technique has become an essential tool in probing the chemical composition of macromolecules, and in elucidating anatomical properties of soft biological tissues. An evolution of the MRI modality has resulted in the development of additional techniques that resolve additional information in tissue structure (water diffusion anisotropy, magnetization transfer, spectroscopy) and brain function (fMRI). In this chapter, the physical and mathematical framework behind myelin quantification via the T_2 relaxation derived myelin water signal is explained. We begin with a description of the theoretical foundations of NMR, extend our treatment to include a description of MRI, and finally provide an overview of methods, results, and physiological interpretations of T_2 relaxation analysis.

2.1 A Quantum Mechanical Account of Sample Polarization

The property of spin angular momentum was first proposed by Dirac in 1930, as a consequence of his quantum mechanical description of atomic nuclei. An atom consists of a nucleus and its surrounding electrons, which orbit the nucleus in allowed states or orbitals. Similarly, the nucleons (neutrons and protons) of a nucleus occupy nuclear orbitals, and are subject to rules governing orbital occupation that are similar to the quantum mechanical constraints that exist for the occupation of atomic energy levels by electrons. Three quantum numbers characterize the state of a nucleon: orbital angular momentum ℓ, spin angular momentum s, and total angular momentum $\mathbf{j}$. The nuclear spin, $\mathbf{I}$, is the total angular momentum of the nucleus and is defined as the vector sum of the angular momenta of the individual nucleons $\mathbf{j}_i$.

The Pauli exclusion principle, one of the afformentioned quantum mechanical restrictions on the electronic configuration of an atom, states that no two electrons can occupy the same atomic energy state. Equally applicable to all fermions, it also restricts any two nucleons occupying the same orbital from having the same spin quantum number. Consequently nucleons experience a 'pairing force', in that the most energetically favourable state results from the coupling of nucleons such that their spin and orbital angular momentum sum to zero. Therefore when an atom is composed of an even number of protons and neutrons, its nuclear spin necessarily sums to zero.

The nulling of the net spin of the nucleus has ramifications on its magnetic properties. The nuclear spin and magnetic dipole moment are related by:

$$\boldsymbol{\mu}=\gamma\mathbf{I} \tag{2.1}$$

where γ is the gyromagnetic ratio, specific to the nucleus. (e.g. the gyromagnetic ratio for protons is 2.675 x 10^8 rad/s/T). Nuclear magnetic resonance relies on the interaction of the magnetic dipole moment of the nucleus with an externally applied magnetic field, hence only atoms with non-zero **I** (i.e. an odd number of protons or neutrons) can be candidates for nuclear magnetic resonance experiments. Table 2.1 lists some nuclei that are commonly studied using NMR.

Table 2.1 Nuclides commonly used in NMR

Nucleus	Nuclear Spin **I**	γ (MHz/T)	Isotropic Abundance (%)
^{1}H	1/2	42.6	99.98
^{13}C	1/2	10.7	1.108
^{17}O	5/2	5.8	0.037
^{19}F	1/2	40.0	100
^{23}Na	3/2	11.3	100
^{31}P	1/2	16.7	100

For a particle of spin angular momentum s, the projection of the spin onto the z axis can assume a range of values m_s defined as $m_s = -s, -s+1, -s+2 \ldots s$. Most Magnetic Resonance Imaging applications rely on the MR signal from ^{1}H, the dominant host of which is water, which constitutes 60% of human body mass. We therefore continue our treatment of NMR theory with reference to a spin 1/2 particle.

When the magnetic moment is subject to an applied magnetic field, they interact with energy given by their dot product, known as the Zeeman energy,

$$E=-\boldsymbol{\mu}\bullet\mathbf{B} \tag{2.2}$$

By combining equations (2.1) and (2.2) we can define the Hamiltonian operator of our spin system as [41]:

$$H=-\hbar\gamma\mathbf{B}\bullet\mathbf{I} \tag{2.3}$$

Considering an applied **B** field along the *z* axis, the dot product reduces to

$$H = -\hbar\gamma B_z I_z \tag{2.4}$$

This is known as the Zeeman Hamiltonian. Using the Zeeman Hamiltonian, we find the Schrödinger equation yields the energy of the eigenstate [41]

$$\begin{aligned} &H|m_s\rangle = E|m_s\rangle \\ &-\hbar\gamma B_z I_z|m_s\rangle = -\hbar\gamma B_z m_s|m_s\rangle \\ &\therefore E = -\hbar\gamma B_z m_s \end{aligned} \tag{2.5}$$

For a proton with $m_s = \pm 1/2$ the transition between the two states represents a change in energy of

$$\Delta E = \hbar\gamma B_z \tag{2.6}$$

This introduction of an energy difference between "spin up" (aligned with the applied magnetic field, lower energy) and "spin down" (aligned against the applied magnetic field, higher energy) states is known as Zeeman splitting, and is illustrated in figure 2.1

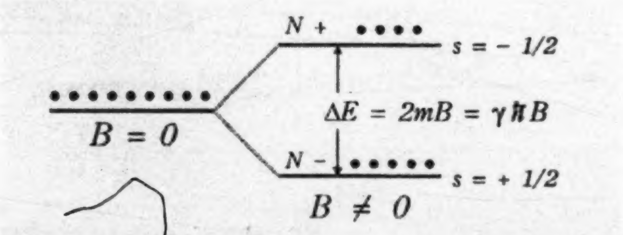

Figure 2.1 Zeeman energy splitting. There are two possible energy states for a proton in a magnetic field due to the interaction of its magnetic moment and the external magnetic field **B**. For a large number of protons, the population ratio for the two states depends on their energy difference according to the Boltzmann distribution. Figure from [40].

Given the Zeeman-split ground state, a slight majority of the nuclei assume the lower energy configuration, with their magnetic moments aligned parallel to the direction of the external field. The ratio of spin up to spin down nuclei can be determined from statistical considerations. Boltzmann's distribution relates the probability for a nucleus to be in a physical state *P(E)* to the energy associated to the state *E*:

$$P(E) = Ce^{-\frac{E}{kT}} \tag{2.7}$$

where *C* is a constant and a property of the system in question, *T* is the absolute temperature, and *k* is the Boltzmann constant (1.38 x 10^{-23} Joule/K). It follows that the population ratio between the two energy states will depend on the energy difference between the states:

$$R = \frac{P(E^-)}{P(E^+)} = e^{\frac{\Delta E}{kT}} = e^{\frac{\gamma\hbar B}{kT}} \tag{2.8}$$

Using a Taylor series approximation, and assuming realistic imaging conditions of T=300K and B=1.5T, we can estimate the population ratio to be:

$$R \approx 1 + \frac{\Delta E}{kT} = 1.0000102 \tag{2.9}$$

Therefore very few (one in 10^5) of the magnetic moments overcome thermal randomization to align themselves in the direction of the applied field. While this fraction is small, there is a large number of contributing dipoles (10^{15} in a 5mm^3 volume) [40]. The net effect of these factors is the creation of a net macroscopic angular momentum, **J**, and net macroscopic magnetization **M**, both in the direction of the applied field.

Statistical considerations also determine the magnitude of this equilibrium value of the macroscopic magnetization. Consider a population of $N=N^+ + N^-$ spins, each with a magnetic moment $\boldsymbol{\mu}$. Using equation (2.9) describing the ratio of spin up to spin down nuclei,

$$\begin{aligned} |\mathbf{M}| &= \mu(N^- - N^+) \\ &= \mu N \frac{R-1}{R+1} \\ &= \mu N \tanh\left(\frac{\Delta E}{2kT}\right) \end{aligned} \tag{2.10}$$

This magnetization is aligned with the z axis, which is by definition the direction of the applied magnetic field.

2.2 Behaviour of M in Static and Time Varying Magnetic Fields

2.2.1 Precession

In the Heisenberg representation, the expectation value of any observable F has an equation of motion given by [40]:

$$\frac{d}{dt}\langle F\rangle = \frac{i}{h}\left\langle\,[H,F]\,\right\rangle = \frac{i}{h}\langle HF - FH\rangle \tag{2.11}$$

where H is the Hamiltonian energy operator, the square brackets [ ] denote the canonical commutation relation [41], and the brackets < > denote the expectation value of an observable O [41]:

$$\langle O\rangle = \langle\Psi|O|\Psi\rangle \tag{2.12}$$

If the observable of interest is $\boldsymbol{\mu}$, then the Hamiltonian is given by equation (2.3), and we may express the equation of motion of $\boldsymbol{\mu}$ as [40]:

$$\frac{d}{dt}\langle\boldsymbol{\mu}\rangle = \frac{i}{h}\langle(-\boldsymbol{\mu}\bullet\mathbf{B})\boldsymbol{\mu} - \boldsymbol{\mu}(-\boldsymbol{\mu}\bullet\mathbf{B})\rangle \tag{2.13}$$

Combining this result with the definition of the magnetic dipole for a single proton, $\boldsymbol{\mu}=\gamma\mathbf{j}$, and the following property of angular momentum operators in quantum mechanics [41],

$$\mathbf{j}\times\mathbf{j} = ih\mathbf{j} \tag{2.14}$$

it can be shown that [40]:

$$\frac{d\langle\boldsymbol{\mu}\rangle}{dt} = \gamma^2\langle\mathbf{B}\times\mathbf{j}\rangle = \gamma\langle\boldsymbol{\mu}\rangle\times\mathbf{B} \tag{2.15}$$

Equation (2.15) describes a precession of $\boldsymbol{\mu}$ about a central axis collinear with the applied field. For a population of N protons in a sample volume, **M** is related to the statistical average of magnetic dipoles $\boldsymbol{\mu}_{av}$ by $\mathbf{M}=N\boldsymbol{\mu}_{av}$. We can therefore extend this result to describe the motion of the net macroscopic magnetization about the applied magnetic field:

$$\frac{d\mathbf{M}}{dt} = \gamma\mathbf{M}\times\mathbf{B} \tag{2.16}$$

It is noteworthy that an equivalent result falls from a classical treatment, wherein the proton is treated as a spinning charge and is endowed with the electromagnetic properties of a current loop (figure 2.2).

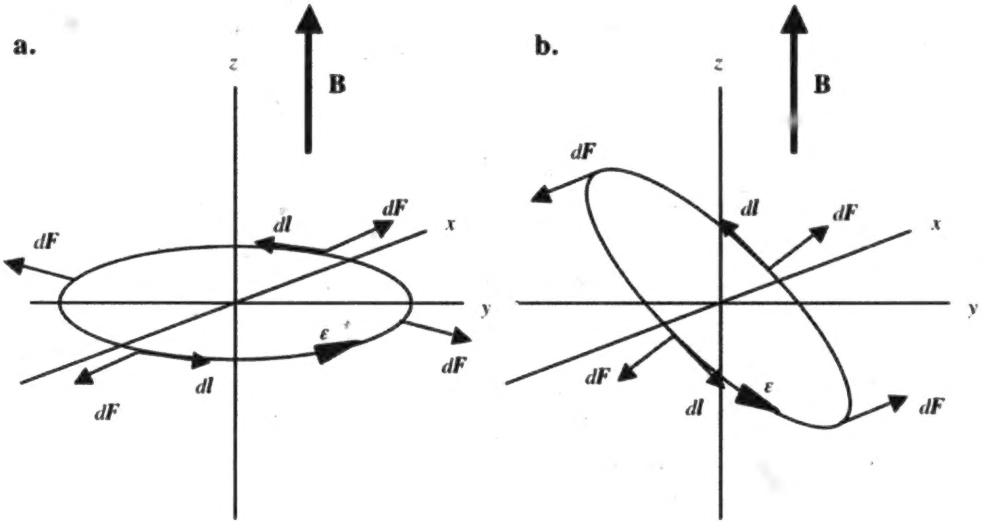

Figure 2.2 Two different orientations of a circular loop carrying current ε in a magnetic field **B**. In (**a**) the plane of the loop is orientated perpendicular to the magnetic field and the net torque is zero, while in (**b**) a net torque is applied about the loop center.

The force $d\mathbf{F}$ experienced by a segment of the current loop $d\mathbf{l}$ in a magnetic field **B** is given by the Lorentz force law [42],

$$d\mathbf{F} = \varepsilon d\mathbf{l}\times\mathbf{B} \tag{2.17}$$

As illustrated in figure 5.2, the differential force contributions acting on the loop sum to zero given a uniform magnetic field. If the loop is orientated out of the plane as in figure

2.2b however, there is a non zero net *torque* applied about the loop center. The differential torque $d\mathbf{T}$ resulting from the differential force $d\mathbf{F}$ is [42]:

$$d\mathbf{T} = \mathbf{r} \times d\mathbf{F} \tag{2.18}$$

where $\mathbf{r}$ is the position vector from the centre of the loop to the point of force application [42]. Combining equations (2.17) and (2.18), and defining the magnetic moment of the current loop $\boldsymbol{\mu}$ as [42]

$$\boldsymbol{\mu} = \varepsilon \pi r^2 \mathbf{n} \tag{2.19}$$

(where $\mathbf{n}$ is a unit vector normal to the loop surface), it can be shown that [42]:

$$\mathbf{T} = \boldsymbol{\mu} \times \mathbf{B} \tag{2.20}$$

The expression for the magnetic moment of a current loop (2.19) holds for the current distribution of a spinning proton, but is not valid for all current geometries. Nonetheless, it can be shown the expression for the net torque (2.20) is a general one, valid for any closed current distribution [42].

Equivalency of (2.20) and the rate of change of the net magnetization derived in the quantum framework (2.16) falls from once again treating a population of dipoles $\mathbf{M}=N\boldsymbol{\mu}_{av}$, and equating the application of a net torque,

$$\mathbf{T} = \mathbf{M} \times \mathbf{B} \tag{2.21}$$

to the rate of change of angular momentum,

$$\mathbf{T} = \frac{d\mathbf{J}}{dt} = \frac{1}{\gamma}\frac{d\mathbf{M}}{dt} \tag{2.22}$$

While the resulting equation of motion is identical to that derived through quantum mechanical considerations, the classical treatment benefits from intuition developed through previous experience with analogous physical systems (e.g. a precessing gyroscope in a gravitational field). This classical picture of magnetization is often sufficient to understand many NMR techniques.

The frequency of the precessions described by (2.15) and (2.16) is of great importance in Magnetic Resonance applications. Transforming equation (2.15) from the stationary frame to a frame of reference ($x'y'z'$) rotating at a yet undetermined angular velocity $\boldsymbol{\omega}$ about the $z=z'$ axis yields:

$$\frac{d\boldsymbol{\mu}}{dt} = \boldsymbol{\mu} \times (\gamma \mathbf{B} + \boldsymbol{\omega}) \tag{2.23}$$

This reduces to the same equation of motion as that for the stationary frame upon the introduction of an effective field $\mathbf{B}_e$ such that

$$\mathbf{B}_e = \mathbf{B} + \frac{\boldsymbol{\omega}}{\gamma} \tag{2.24}$$

The natural frequency of the system is defined as that $\boldsymbol{\omega}$ such that $\mathbf{B}_e=0$, that is,

$$\omega = -\gamma \mathrm{B}\hat{\mathbf{z}} \tag{2.25}$$

This result also falls from the solutions to the differential equations for $d\boldsymbol{\mu}/dt$ and $d\mathbf{M}/dt$, and relates the precession frequency of nuclei in a applied field to properties inherent to the nuclei themselves (the gyromagnetic ratio, γ) and the applied field strength $|\mathbf{B}|$. This frequency is commonly referred to as the Larmor frequency, in honour of the Irish physicist who described the dynamics of precessing systems. The Larmor frequency is an essential consideration in NMR and MRI applications.

2.2.2 RF Excitation

The introduction of an orthogonal time varying magnetic field tuned to the Larmor frequency of the system can perturb the net magnetization vector from thermal equilibrium through a resonance effect. As can be seen from table 2.1, the Larmor frequencies of most nuclei lie in the radio-frequency range, hence the EM pulse used to excite the spins is commonly referred to as an RF pulse.

The effects of an RF pulse ($\mathbf{B}_1$) are best understood from the rotating frame of reference. In this frame, rotating with angular velocity $\boldsymbol{\omega}$ along the $z=z'$ axis, the orthogonal magnetic field of frequency ω transforms to a constant magnetic field pointing in some direction in the *xy* plane, denoted as the *x'* direction by convention. According to equation (2.16) **M** will precess about $\mathbf{B_1}$, tipping it away from thermal equilibrium through an angle α described by

$$\alpha = \gamma B_1 \tau \tag{2.26}$$

Where τ is the duration of the RF pulse of magnitude B_1. Pulse durations needed to flip **M** by π and π/2 are of particular importance in MRI data acquisition. Note that excitation about the *y'* axis can subsequently be achieved by varying the phase of the RF pulse by π/2.

A linear field of frequency ω can be decomposed to two circularly polarized components, one stationary with respect to the rotating frame (that component which effectively perturbs magnetization), the other rotating at 2ω (too far from resonance to effectively interact with the system). In practice, RF excitation occurs in quadrature, utilizing two coils with orthogonal axes. With such a configuration, both components of the circularly polarized field impart a resonance effect in RF excitation.

2.2.3 Relaxation

According to equation (2.16), the perturbed magnetization vector would indefinitely precess about the main field B_o after RF excitation. In reality however, interactions between individual spins and between the spin system and the surrounding lattice structure result in an exchange in energy that acts to restore the thermal equilibrium magnetization. The effects of these interactions are modeled by simple exponential processes, with characteristics times T_1 (longitudinal relaxation time) associated with spin-lattice interactions, and T_2 (transverse relaxation time) associated with spin-spin interactions. Differences in the chemical and magnetic environments in different anatomical tissues confer a difference in the spin-lattice and spin-spin systems, hence images weighted on T_1 and T_2 relaxation times can be useful in distinguishing different soft tissues in MRI. Collectively, the return of the macroscopic magnetization back to its thermal equilibrium value is known as relaxation.

Including relaxation effects into our equation of motion for **M** yields the phenomenological Bloch equation:

$$\frac{d\mathbf{M}}{dt} = \gamma \mathbf{M} \times \mathbf{B} - \frac{M_x\hat{x} + M_y\hat{y}}{T_2} - \frac{(M_z - M_o)\hat{z}}{T_1} \tag{2.27}$$

Where $\hat{x}, \hat{y}, \hat{z}$ are unit vectors along their respective axes and M_x, M_y, and M_z are the components of **M** in those respective directions. Expressing the transverse component of **M** as a single complex variable M_T

$$M_T \equiv M_x + iM_y \tag{2.28}$$

allows expression of the general solutions for the longitudinal and transverse components of magnetization as

$$M_z(t) = M_o + \left(M_z - M_o\right)e^{-\frac{t}{T_1}} \tag{2.29}$$

$$M_T(t) = M_T(0)e^{i\gamma B_o t}e^{-\frac{t}{T_2}} \tag{2.30}$$

Which describe a recovery of the magnetization along the z axis and a simultaneous decay of a precessing transverse component in the xy plane. The time evolution of **M** described by equations (2.29) and (2.30) is shown in figure 2.3

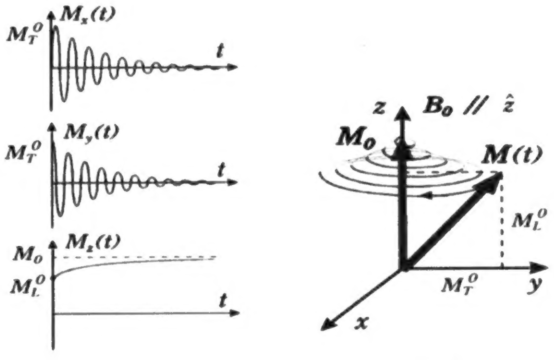

(a) (b)

Figure 2.3 Time evolution showing post-excitation recovery of sample magnetization, in accordance with equations (2.24) and (2.25). Figures from [40].

2.2.4 Induction Signal Detection

By perturbing the magnetization vector the precession described by equation (2.27) can be detected by an induction coil, which is generally the same coil that was used to deliver the RF excitation pulse. Consider an induction coil oriented along the x axis. The magnitude of the voltage induced in this coil is given by Faraday's law:

$$V = \frac{1}{c}\frac{d\phi}{dt} \tag{2.31}$$

Where V is the induced voltage, c is the speed of light, and ϕ is the magnetic flux induced to the coil, which is proportional to the component of the magnetization along the x axis. Given the induction signal dependence on the transverse component of the magnetization, we would naturally expect that the voltage induced in the coil would take the form of equation (2.30): a decaying sinusoid with time constant T_2. In practice however, local magnetic field inhomogeneity within the sample causes spins at different locations to precess at slightly different angular frequencies. As viewed in a frame rotating at the central Larmor frequency, this causes the transverse component to 'fan out', resulting in an accelerated decay of M_T characterized by time constant T_2^*. We can relate T_2^* to T_2 by the inclusion of a term accounting for magnetic field inhomogeneity

$$\frac{1}{T_2^*} = \frac{1}{T_2} + \gamma\Delta B \tag{2.27}$$

where ΔB is a measure of field inconsistency across the sample. The exact form of the T_2^* envelope depends on the specific distribution of Larmor frequencies within the sample. The resulting induction signal, referred to as a free induction decay (FID), adopts a characteristic appearance, shown in figure 2.4

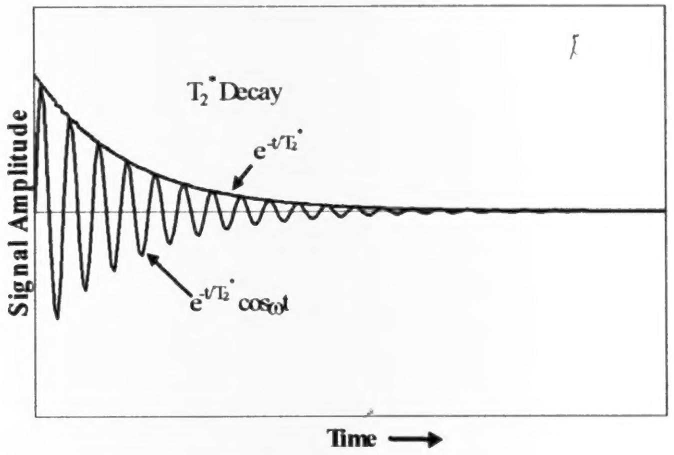

Figure 2.4 Characteristic appearance of a free induction decay curve. The sinusoid decays with time constant T_2*.

2.3 The CPMG Pulse Sequence and True T_2 Measurement

The effects of local field inhomogeneity make the determination of true T_2 difficult. Shortly after the discovery of NMR, Hahn showed that the signal loss due to inhomogeneity-induced dephasing of the transverse magnetization is recoverable, through the creation of spin echoes [43]. The basic precept of Hahn's sequence was adapted by Carr and Purcell [44], and further modified by Meiboom and Gill [45], resulting in the CPMG sequence that has found a commonplace application in NMR and MRI. The CPMG sequence is typically denoted as 90°x'-τ-180°y'-τ-echo, where the x' and y' suffixes indicate that the magnetization vector is flipped about those respective axes. The effects of the application of such a sequence on the magnetization vector are shown in figure 2.5.

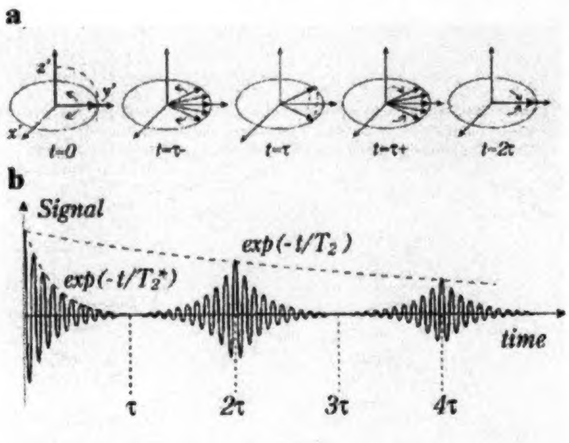

Figure 2.5 (**a**) Dephasing of transverse magnetization due to field inhomogenaiety, signal loss is recoverable through the application of a 180° pulse along the y' axis. (**b**) A train of spin echoes form the basis for a CPMG experiment, through which true T_2 can be measured. From [40].

As can be surmised from figure 2.5, in an experiment involving *n* echoes, the signal intensity of the echoes obeys

$$S(2n\tau) = S(0)e^{-\frac{2n\tau}{T_2}} \tag{2.32}$$

where *S* is the signal intensity. The CPMG sequence is commonly employed in MRI for T_2 measurement. It is noteworthy that the application of the 180° pulse in the y' direction distinguishes the sequence from the CP form, and leads to a cancellation of errors arising from imperfect 180° pulses that otherwise accumulate in a multi-echo experiment.

2.4 Principles of Spatial Localization in MRI

The preceding section illustrated how the measurement of the precession frequency and relaxation of different groups of spins yields information concerning their chemical and biological environment. However little has been mentioned of how that information can be resolved to give a spatial representation of those environments: the ultimate goal of any imaging modality. By introducing a known spatial dependence to the applied magnetic field, we introduce a spatial variation to the spin precession characteristics (e.g. frequency and phase) of the system. This information can be manipulated to produce a point to point mapping of spin environments – an MR image. In this section we briefly outline three techniques used to achieve spatial encoding in MRI: slice selection, frequency encoding, and phase encoding.

2.4.1 Slice Selection

Consider the simple case of a linear field gradient that increases along the z axis such that

$$B = (B_o + zG_z) \tag{2.33}$$

This introduces a z dependence to the spin precession frequency

$$\omega(z) = \gamma(B_o + zG_z) \tag{2.34}$$

Therefore all spins in a plane perpendicular to the z axis will precess with the same Larmor frequency. Using an appropriately tuned RF pulse, a slice of spins with a narrow range of precession frequencies can be excited. To excite a sharp edged slice, a sinc shaped RF excitation pulse is required, according to the FT relationship between the spatial and frequency domains. Slice thickness is modulated by a corresponding choice of RF bandwidth, the relation being described by

$$d = \frac{\Delta\omega}{\gamma G} \tag{2.35}$$

where d is the slice thickness and $\Delta\omega$ is the RF bandwidth.

Two features of the slice select gradient are noteworthy. Firstly, the gradient used to introduce precession frequency spatial dependence can have any orientation, allowing MRI to image in any oblique plane. Secondly, it should be noted that the slice select gradient introduces a continuous variation in Larmor frequencies between the slice endpoints defined by the RF bandwidth. This difference in precession rate creates a relative dephasing of the spins being tipped into the xy plane. The negative lobe accompanying the initial slice select pulse (shown in figure 2.6) serves to refocus this linear dispersion.

2.4.2 Frequency and Phase Encoding

Given a selectively excited slice, there are two remaining orthogonal directions in which spatial encoding is required. Fittingly, gradients in the remaining orthogonal directions to the slice select gradient are employed in resolving this spatial information.

Frequency encoding refers to a post-excitation manipulation of precession frequency, through the introduction of a second gradient, conventionally denoted G_x. For simplicity, we consider a linear frequency encoding gradient, similar to the slice select gradient G_z. This frequency encoding gradient introduces an *x* dependence to the precession frequencies of the spins in the excited slice, and this spatial dependence manifests itself in the received induction signal. Over the brief time of gradient application, we can consider the induction signal to be the spatially integrated complex magnetization given by equation (2.30), with relaxation effects ignored. Accounting for the Larmor frequency variation induced by the new gradient G_x and denoting the spin density distribution along the *x* axis as *P(x)*, we can write the complex signal *C(t)* as

$$C(t) = \int P(x) e^{i\gamma x G_x t} dx \tag{2.36}$$

We then introduce the reciprocal space vector

$$\mathbf{k} = \gamma \mathbf{G} t \tag{2.37}$$

Making this substitution in equation (2.36) yields

$$S(k_x) = \int_{-\infty}^{\infty} P(x) e^{ik_x x} dx \tag{2.38}$$

Taking the inverse Fourier Transform resolves an expression for the 1D projection of the magnetization along the *x* axis:

$$P(x) = \frac{1}{2\pi} \int_{-\infty}^{\infty} S(k_x) e^{-ikx} dk_x \tag{2.39}$$

Frequency encoding demonstrates the utility of the inverse Fourier transform in discerning spatial information from an MRI experiment. This process could potentially be repeated in *y* and other directions, yielding a 2D distribution of spin density after projection reconstruction.

However, the vectoral nature of the MR signal creates complications for this back projection approach, as localized field inhomogeneities create a non-uniform dephasing of magnetization, thus affecting the magnitudes of the spin densities projected onto the axes. Ironically, it is through the utilization of the vectoral nature of MR data that a more refined method in spatial localization takes form: phase encoding. The remaining orthogonal gradient, G_y, can be used to impose a linear phase dispersion through its application for a finite period of time, thereby encoding spatial information in the phase of the magnetization vector. Various vector projections can be then achieved with a single frequency encoding step by its accompaniment with a multitude of phase dispersions, allowing the resolution of a 2D image.

The application of G_y for a time τ creates a known phase rotation

$$\theta = \gamma y G_y \tau \tag{2.40}$$

Typical numbers of phase encoding steps are 64, 128, 256, and 512, as the Fast Fourier Transform algorithm employed handles data arrays with a length power of two. This array is best represented in vectoral form

$$\mathbf{F} \cdot \mathbf{m} = \mathbf{p} \tag{2.41}$$

where $\vec{\mathbf{p}}$ are the vectoral projections along the *y* axis, $\vec{\mathbf{m}}$ is the magnetization associated with each projection, and the elements of **F** are given by:

$$\mathbf{F}_{jk} = \frac{1}{\sqrt{N}} e^{-i\frac{2\pi jk}{N}} \tag{2.42}$$

where *N* is the number of phase encode steps and $-N/2 \leq j,k \leq N/2$. The matrix **F** is unitary, making $\mathbf{F}^{-1}$ its transposed conjugate $(\mathbf{F}^{T})^{*}$. We can use $\mathbf{F}^{-1}$ to resolve the spatial distribution of magnetization along the *y* axis

$$\vec{\mathbf{m}} = \mathbf{F}^{-1}\vec{\mathbf{p}} \tag{2.43}$$

As can be seen by the form of equation (2.42), **F** and $\mathbf{F}^{-1}$ represent the forward and inverse two dimensional Fourier transforms (2DFT). Spatial localization methods in MRI therefore involve 2D image reconstruction from consecutive, commuting inverse fourier transformations, one yielding projections of the vector field with different amounts of phase dispersion in the *y* direction, the second determining the magnetization of each pixel along the vertical direction from the vector projections.

2.4.3 k Space

Given the nature of data analysis involved, the differences between the sampling domains of MRI as compared to other imaging techniques are obvious. Most modalities in medical imaging sample data in the spatial domain, the same domain in which the subject is located. MRI however, samples data in the frequency domain: spatial information is encoded into system precession characteristics through field gradients, and subsequently resolved using Fourier Transform analysis.

Defining the spin density ρ(**r**) as the number of spins at a particular location **r**, and drawing on our definition of the reciprocal space vector **k** (equation 2.37) we can consolidate the relationship between signal and spin density as:

$$\begin{aligned} S(\mathbf{k}) &= \iiint \rho(\mathbf{r}) e^{i\mathbf{k}\cdot\mathbf{r}}\, d\mathbf{r} \\ \rho(\mathbf{r}) &= \iiint S(\mathbf{k}) e^{-i\mathbf{k}\cdot\mathbf{r}}\, d\mathbf{k} \end{aligned} \tag{2.44}$$

i.e. **k** is the *conjugate variable* for **r**. The elements of **k** (k_x, k_y, k_z) are associated with a frequency space where mapping to the spatial domain is one to one. Meanwhile, the applied field gradients G_x, G_y, and G_z can subsequently be interpreted as the velocity of k space sampling along k_x, k_y, and k_z in the frequency domain.

Equation (2.44) is known as the central imaging equation. The well defined relationship consolidates different techniques of spatial localization in MRI (i.e. variations in gradient pulse sequences) as different methods of sampling k space. An example of a commonly employed 2DFT method, involving a slice-selective RF pulse along the *z* direction and requiring the sampling of a two dimensional k space after slice excitation, is shown in figure 2.6.

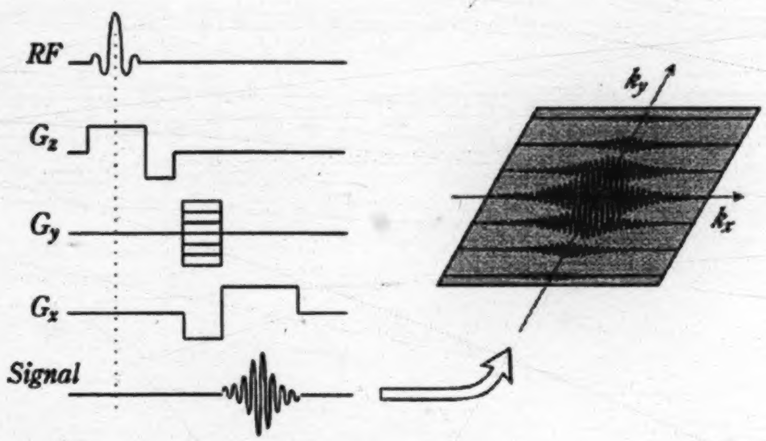

Figure 2.6 Gradient echo 2DFT pulse sequence, and the inducution signals written as a 2DFT matrix. From [40].

Figure 2.6 illustrates the need for sequential gradient activation with specific timing and duration constraints. Repetition time (TR) and Echo time (TE) are two parameters used to characterize these constraints. TR is the time between successive RF excitations, and is hence a measure of the time allowed for relaxation. TE denotes the time between RF excitation and the ensuing echo (i.e. in the typical CPMG sequence $90°x'$-τ-$180°y'$-τ-echo, TE = 2τ). In a multi-echo CPMG experiment, TE also corresponds to the time between successive echoes. Collectively, the temporal constraints imposed on Gradients and RF (reflected in part by TR and TE) delineates a pulse sequence, which are often pictorially represented as in figure 2.6.

2.5 Myelin Water Measurement Using MRI

As was explained in section 2.3, a multi echo CPMG sequence can reverse the signal loss due to inhomogeneity-induced dephasing of the transverse magnetization, yielding a measurement of the true T_2 of the sample. When such a measurement is made on an inhomogeneous sample (i.e. a sample with multiple relaxation environments) the ensuing decay curve contains contributions from protons within each of those environments. Therefore, inherent in a T_2 decay curve from a single CNS voxel is information concerning the number and relative size of diffusion-restricted relaxation environments in the tissue. In this section, we summarize the techniques used to resolve this information, and examine the physiological implications of multi-exponential T_2 relaxation: namely, the quantification of myelin.

2.5.1 T_2 Relaxation Analysis

We seek to resolve the contributing exponentials and their respective time constants from multi-echo T_2 relaxation data. The general integral equation describing multi-exponential T_2 relaxation is

$$y(t_i) = y_i = \int_a^b s(T_2) e^{-\frac{t_i}{T_2}} dT_2 \qquad i=1,2...,N \tag{2.45}$$

where the N data y_i are measured at times t_i, and $s(T_2)$ is the amplitude distribution of the contributing exponentials as a function of their characteristic relaxation time. Nonlinear techniques have shortcomings in their applications with such models, as they require *a priori* assumptions as to the number of contributing exponentials, a starting model to begin iterations, and they often converge to a local minimum, if at all [46]. Linear techniques, meanwhile, assume a large number of T_2 times and solve for the corresponding amplitudes, some of which may be zero. This approach does not involve *a priori* assumptions as to the number of contributing exponentials (which reflect physiological properties of the system), and are guaranteed to converge at the absolute minimum within the defined solution space [46].

Computer implementation of convergence algorithms require the discretization of $s(T_2)$ in equation (2.45). Assuming that the T_2 distribution is a sum of M delta functions with areas s_j and known relaxation times T_j such that

$$s(T_2) = \sum_{j=1}^{M} s_j \delta(T_2 - T_{2,j}) \tag{2.46}$$

This linear system of equations has the general form

$$y_i = \sum_{j=1}^{M} A_{ij} s_j \qquad i=1,2,...,N \tag{2.47}$$

where the A_{ij} form elements of the constraint matrix **A**. Equation (2.47) represents the basic system we wish to solve.

Due to the presence of noise in the acquired data, exact solutions to (2.47) would confer noise related contributions in the resulting distribution $s(T_2)$. Acceptable solutions must therefore misfit the acquired data by an amount consistent with the experimental error [46]. We quantify this misfit using the chi squared statistic:

$$\chi^2 = \sum_{i=1}^{N} \frac{(y_i^p - y_i)^2}{\sigma_i^2} \tag{2.48}$$

where y_i is the measured datum, and y_i^p corresponds to the value predicted by the constructed model. The expected value of the χ^2 statistic – the one associated with an adequate model – is $\chi^2 \cong N$. Substantial deviations from this expected value indicate that the data is either fit too accurately ($\chi^2 << N$, resulting in the afformentioned noise related artifactual contributions to $s(T_2)$), or that the constructed model does not adequately fit the data ($\chi^2 >> N$, resulting in a T_2 distribution that does not accurately represent the T_2 characteristics of the sample) [46].

Nonnegative least squares (NNLS) approaches to solving equation (2.47) involve finding the set of s_j which minimizes the least squares misfit

$$\sum_{i=1}^{N} \left| \sum_{j=1}^{M} A_{ij} s_j - y_i \right|^2 \tag{2.49}$$

When normalized to unit variance, minimization of equation (2.49) also minimizes the χ^2 misfit of equation (2.48). Resulting NNLS solutions tend to converge to a value of $\chi^2 < N$, and consist of a few isolated delta functions [46].

It is more likely, however, that a sample such as CNS tissue exhibits a continuous distribution of T_2 values as opposed to the discrete solutions offered by minimization of equation (2.49), even if relaxation environments are highly compartmentalized. NNLS can be adapted to construct a continuous distribution by introducing additional constraints that regularize solutions, making resulting T_2 spectra less susceptible to noise related artifactual contribution. The introduction of such constraints confers a tradeoff between the model fit to acquired data (as indicated by the χ^2 misfit), and the weighting associated to the desired characteristics of the resulting distribution *s(T₂)*. This tradeoff manifests itself through minimization of

$$\sum_{i=1}^{N}\left|\sum_{j=1}^{M} A_{ij}s_j - y_i\right|^2 + \mu\sum_{k=1}^{K}\left|\sum_{j=1}^{M} H_{kj}s_j\right|^2 \tag{2.50}$$

Where $\mu>0$ is a tradeoff parameter, such that increasing μ ascribes a greater weighting to solving the constraints of matrix **H** at the expense of the χ^2 misfit. **H** is a matrix of additional constraints, reflecting the aforementioned desired properties of the T_2 distribution; for instance if the characteristic of interest is solution curvature, the rows of **H** are set to finite difference approximations of second order derivatives of $s(T_2)$. Prudent choice of μ can therefore result in an acceptable $\chi^2 \cong N$ while simultaneously arriving at a form of $s(T_2)$ that is feasible given the system of interest. Non regularized and regularized solutions are contrasted in figure 2.7.

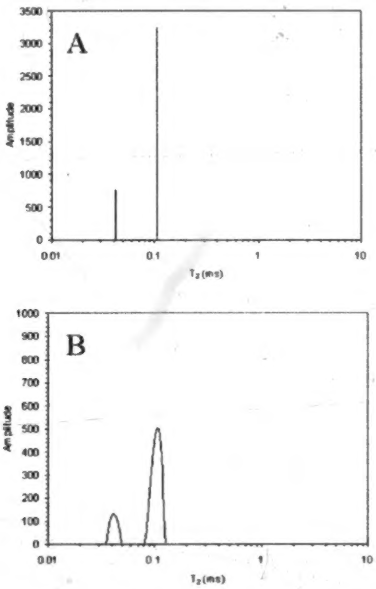

Figure 2.7 (A) Non regularized T_2 distribution, where $s(T)$ is represented as a sum of delta functions. **(B)** Regularized T_2 distribution, where additional constraints were placed on the squared sum of the amplitudes of the contributing delta potentials.

2.5.2 NNLS Analysis of Spin-Spin Relaxation in CNS tissue

Despite the lack of *a priori* assumptions as to the number or location of contributing exponentials, NNLS analysis of CNS multi-echo relaxation data resolves remarkably consistent T_2 distributions across different voxels. An example of a typical NNLS derived T_2 distribution from central nervous system tissue is shown in figure 2.8. At clinical signal to noise levels, normal CNS tissue has three distinguishable water reservoirs, which have been assigned to cerebrospinal fluid, extra and intracellular water and water compartmentalized within the myelin sheath [47, 48].

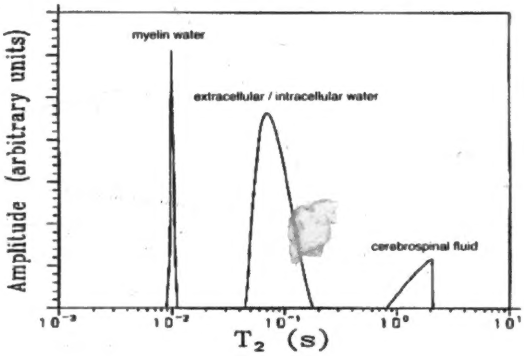

Figure 2.8 Typical T_2 distribution derived from brain tissue, where the resolution of distinct spin spin relaxation times arising from water within the myelin bilayer, in the intra / extracellular space, and in cerebrospinal fluid is possible.

Evidence that the short T_2 component could arise from water trapped within myelin bilayers [49-51] has led to hypotheses that its relative magnitude could at worst be considered a marker for myelination, and at best serve to quantify myelin content in brain white matter. Support for the latter proposition is strengthened by the agreement of "myelin water" measurements of ~ 15% with *in vitro* measurements of myelin water content [52], and with differential calorimetry measurements of bound water [53].

Magnetic resonance studies, meanwhile, have amassed substantial evidence that the short T_2 component is specific to myelin. Its presence was noted in the myelinated trigeminal and optic nerves of the garfish, but not in unmyelinated olfactory nerve of the same species [54]. Its progressive loss was consistent with the demyelination expected to accompany nerve degeneration induced in frog sciatic nerve *in vivo* [55]. These findings are consistent with recent determinations in normal and injured rat sciatic nerve, where the a decrease in the size of the short T_2 component was found to reflect demyelination in Wallerian degeneration, while an increase in short T_2 component size was noted in regeneration following trauma [56]. Similar changes have been visualized *in vivo* through the production of "myelin water maps", which have resolved larger short T_2 fractions on a voxel by voxel basis in areas consistent with white matter distribution [48], and have shown sensitivity to disease processes in MS [57-62].

Evidence of relative sensitivity of the short T_2 component to myelination with respect to other putative MR correlates (such as magnetization transfer, or diffusion tensor imaging) is also mounting. While findings of increased diffusion anisotropy in white matter initially caused speculation that the apparent diffusion coefficient could be sensitive to myelination, subsequent findings of significant diffusion anisotropy in non myelinated garfish nerve [63], and only slightly lower diffusion anisotropy in the spinal cord of myelin difficient rat [64] has led to an increasing consensus that while able to modulate the degree of anisotropy, myelin is likely not the principle determinant of restricted diffusion in nerve tissue [63]. In the context of the role of myelin in neurodevelopment mentioned in chapter 1, it should be noted that myelin associated inhibitors have been suggested as likely contributors to parallel neurite growth [65]. This could imply that correlations between myelination and anisotropy may have much ado with myelin's orientating effects during neurodevelopment.

Meanwhile, there are also indications that changes in the magnetization transfer ratio (MTR) also may not *necessarily* reflect a change in myelination. Similar steady-state MTR characteristics have been reported for myelinic and interaxonal nerve components [66], suggesting that changes in the latter have the potential for getting misinterpreted as a change in myelination given current interpretations of MTR. Furthermore, in experimental models of MS, it was found that while MT changes could be reduced through concomitant reductions in inflammation [67], the size of the short T_2 component was found to be relatively insensitive to the inflammatory response. These findings have since been corroborated by Stanisz *et al.* in a study of the inflammatory response to TNF-α in rat sciatic nerve, in which the authors noted that changes in the T_2 spectrum are most effective way to distinguish inflammation from myelin loss [68].

If successful, the present efforts in measuring the T_2 characteristics of spinal cord tissue in humans *in vivo* would add credence to previous determinations of spatial sensitivity of the short T_2 technique as a marker for myelination. This contribution, in light of the challenges of imaging in the area, would further validate quantitative T_2 as a reliable measure of myelination, and as a potentially useful tool for monitoring disease pathology in all areas of the central nervous system.

Chapter 3: Materials and Methods

T_2 relaxation measurements were made using a multi-echo CPMG sequence [25], as implemented on a GE Signa 1.5T medical imager by MacKay *et. al.* [48]. Twenty, twenty-four and thirty-two echo sequences were employed, the use of the former shortened echo trains stemmed from concerns of RF amplifier loading. After the longer echo train was demonstrated to be within amplifier loading tolerances, it was used to permit more accurate measurement of longer T_2 times [27, 69, 70]. This improves characterization of sample T_2 characteristics and allows a more accurate estimate of the myelin water fraction; subsequent analysis refers exclusively to those 32 echo measurements.

Given that relaxation studies of *in vivo* SC are in their infancy, the human study was complemented by *in vitro* work on bovine spinal cord. The latter studies, free from the technical limitations of *in vivo* imaging in such a physiologically challenging area, allowed for verification of human T_2 measurement in an analogous system at higher SNR, while concomitantly offering an opportunity to explore additional relaxation characteristics of spinal cord tissue.

3.1 Human *in vivo*

3.1.1 Subjects

Twenty two 32 echo relaxation studies were preformed, on normal controls ranging in age from 20-52 years. A sagittal scan plane was chosen in order to permit the measurement of T_2 along the entire length of the spinal cord. Choosing this sagittal profile is not without its challenges however, as capturing the small and mobile SC within a 5mm slice can prove to be difficult, often requiring several localizers and subsequent adjustments in patient positioning. However, given the demonstrated spatial distribution of MS lesion load along the entire length of the spinal cord (figure 3.1), it was reasoned that quantitative T_2 in the sagittal plane could prove to be diagnostically valuable. Localizer images (where the FOV was extended to include C2) were obtained in all subjects in order to determine scan location with respect to spinal vertebrae – counting the vertebrae from C2 is the only reliable way to landmark vertebral segments, even for trained radiologists.

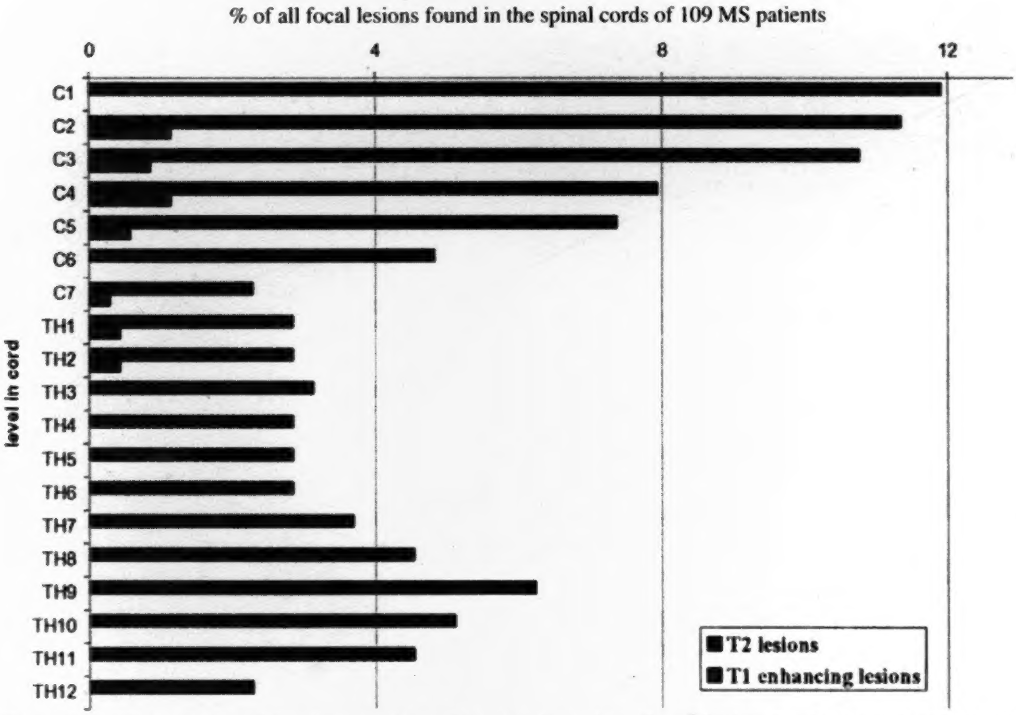

Figure 3.1 Observations of the dissemination of focal lesions along the entire length of the spinal cord in MS patients [17] prompted the choice of a midline sagittal scan plane in the human study in light of its potential diagnostic value. Adapted from [17].

3.1.2 Apparatus

A phased array back RF coil (GE Medical Systems, Milwaukee, WI, USA) was employed to allow imaging along the entire length of the spinal cord. This RF coil consists of an array of six surface coils and acts only to receive the induction signal. Accordingly the Signa body coil was used in RF transmission, ensuring a more uniform excitation profile throughout the spinal cord.

The phased array active coil configuration depends on the physiological area of interest: in this study CTL BOT (a GE interface option corresponding to activation of the lowest 3 coils) was used in Lumbar SC imaging, CTL MID in thoracic imaging, and CTL 12 in anterior thoracic / cervical imaging. In order to prevent mutual interference within the phased array coils during reception, each coil is equipped with its own receive circuit, and coil geometry is arranged such that mutual inductance between neighboring coils is minimized through appropriate coil overlap.

3.1.3 Pulse Sequence and Data Acquisition

32 echo T_2 relaxation studies were performed in a midline sagittal scan plane, chosen to maximize the SC surface area in the scan. Imaging parameters were as follows: 10ms echo spacing (TE, separation between 180° refocusing pulses), 3000ms Repetition Time (TR – time between multi echo acquisitions), 5mm slice thickness, 24×24cm or 28×28 Field of View (FOV), 256×128 acquisition matrix (corresponding to 256 frequency encoding steps in the I/S direction and 128 phase encoding steps in the A/P direction), and 4 NEX (number of averages, or experiments). FOV and matrix size uniquely determine the in-plane resolution of the subsequent MR image – in this experiment the voxel size was 0.937mm×1.875mm×5mm in a 24×24cm FOV, and 1.09375mm×2.1875mm×5mm for experiments with a 28×28cm FOV.

The standard for quantitative T_2 measurement in a clinical setting has become the Poon-Henkelman CPMG sequence [25] shown in figure 3.2.

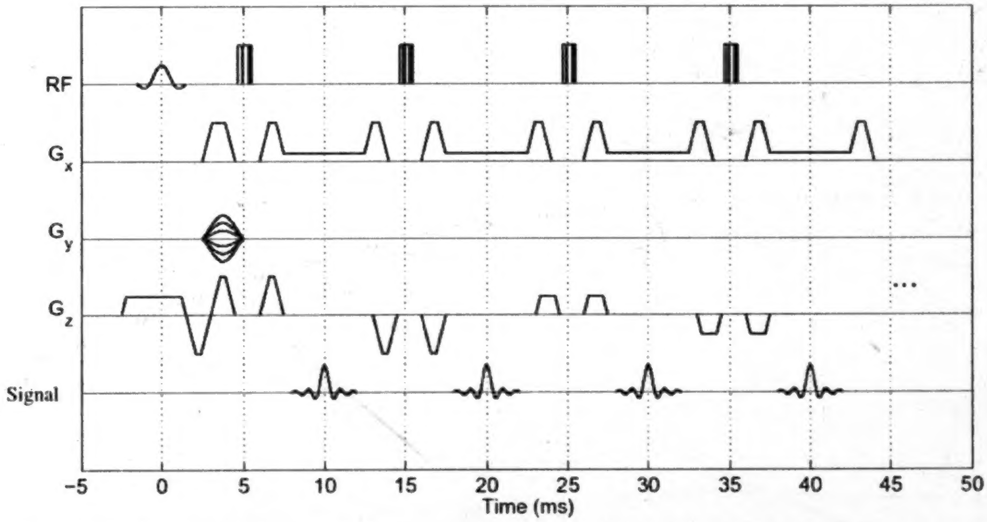

Figure 3.2 Poon Henkelman CPMG sequence (above), consisting of 2 crushers of varying amplitudes flanking each 180° composite (90_x-180_y-90_x) refocussing pulse. The inversion recovery pulse, consisting of a non slice selective apodized sinc pulse at TI=1200ms, is not shown. Adapted from [71].

Several features of this sequence are noteworthy, as they serve to address artifactual complications that arise in quantitative T_2 experiments using more conventional techniques. We touch upon these complications briefly here, and highlight the manner in which they are addressed in the Poon Henkelman implementation.

Out of slice effects

Signal from outside the slice of interest would obviously corrupt analysis and subsequent inference from a quantitative T_2 measurement, where the underlying assumption of the methodology requires that signal from each voxel represent aspects of local microstructure. According to the Fourier relationship between the space and temporal domains, a rectangular slice profile requires a sinc shaped slice selective pulse. Because the RF pulse bandwidth is necessarily constrained in time, limitations in exciting a perfect rectangular slice arise, and result in some ripple within the slice (pass band), and outside the slice (stop band). In order to limit out of slice effects, a large pair of gradients (G_z) flanking each 180° refocusing pulse are employed [25, 72]. These 'crusher' gradients effectively introduce 2π phase dispersion across all voxels; only protons that stay within the slice of interest 'see' both lobes of the gradient and are subsequently refocused to form an echo.

Magnetization Transfer Effects

Multislice techniques are often used in diagnostic MRI sequences, and are particularly valuable in assessing diffuse pathologies that arise from multiple sclerosis. Unfortunately, they are not suitable for quantitative T_2 measurement, as an on resonance RF pulse in the slice of interest is necessarily an off resonance pulse in all other slices in the imaged volume. This off resonance pulse will inadvertently affect the water signal in those slices through partial saturation of the semi-solid pool, and subsequent magnetization exchange with liquid pools (i.e. the magnetization transfer effect). This is of particular concern when quantitative T_2 is aimed at myelin water measurement, as the myelinic component is particularly sensitive to MT exchange dynamics [73, 74]. As result, a single slice is excited through a slice selective apodized sinc pulse of 300ms, and signal from outside the slice of interest is eliminated through the use of the mentioned crusher gradients.

Stimulated Echoes

Loosely defined, stimulated echoes are all echoes that arise from any path other than the 90°-180°-echo CPMG pathway. These are obviously contaminants as they do not decay with the T_2 of the sample, and they are a major complication in T_2 measurement using standard multi-echo imaging methods [75]. Woessner [76] first described these stimulated echoes by considering three echo pathways: a primary (desired) echo due to the desired phase reversal and subsequent refocusing of the magnetization, one stimulated echo resulting from the rotation of temporarily stored longitudinal magnetization back into the transverse plane, and another stimulated echo resulting from magnetization that was unaffected by the first pulse, inverted by the second, and later rephased to form an echo [71, 76].

Both of the latter pathways, and indeed any stimulated echo pathway in a multiecho experiment, can arise from imperfections in 180° refocusing pulses. Magnetization after a non-180° pulse is either distributed into the z axis, or is left to dephase or rephase on the transverse plane [71]. As magnetization in the longitudinal plane does not accrue phase, this introduces a number of magnetization substates, which can be characterized by their net magnetization, phase accumulation, and dephasing / rephasing spin behaviour [77]. This lack of phase coherence leads to refocusing at different timepoints, and the stimulated echo artifact.

Composite pulses can be used to more create a more robust 180° rotation, and hence minimize this effect [26]. The reduction in flip angle error can be shown by comparing the accumulated error that results from a $(180_y^\circ+\delta)$ pulse, to that from a $(90^\circ_x+\delta/2)(180^\circ_y+\delta)(90^\circ_x+\delta/2)$, the simplest composite case. Experimentally, it can be verified by examining flip angle profiles in the presence of B_o and B_1 inhomogenaiety, as shown in figure 3.3.

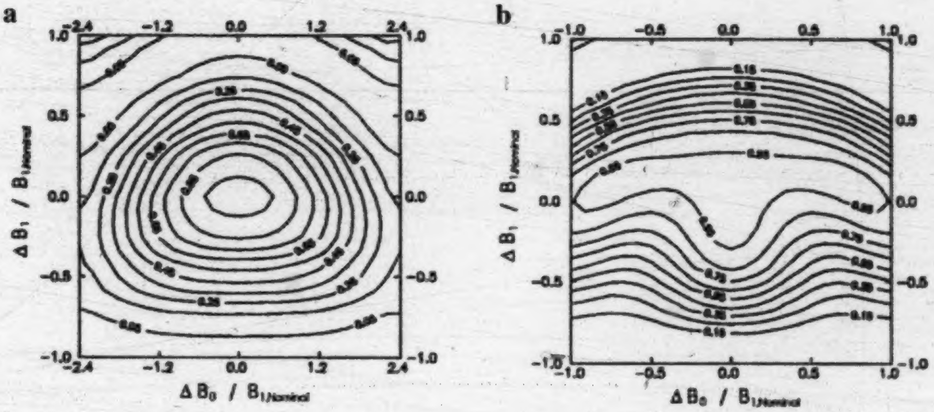

Figure 3.3 The composite pulse is designed to provide a more uniform 180° rotation across the slice, in the presence of field inhomogenaiety. This can be seen by comparing a 180° sinc pulse (**a**), to the composite (90_x-180_y-90_x) pulse (**b**). Contour lines show the fraction of magnetization being refocused in the first echo. Adapted from [26].

As can be seen in figure 3.3, a composite 180° creates a lower phase dispersion under B_o and B_1 heterogeneity [26], leading to a reduction in the stimulated echo artifact, and a more uniform rotation across the slice. While higher order composites do exist [26], the increase in RF power deposition with pulse complexity (e.g. 2π for the mentioned 3 term composite) makes them inappropriate for use *in vivo*.

Spinal Cord MR imaging literature often refers to CSF as a major complicating factor in conventional MRI [37, 78]. Experience in quantitative T_2 has likewise shown that CSF can obscure relaxation measurements. Accordingly, MacKay's implementation of the Poon-Henkelman CPMG sequence (figure 3.2) was adapted through the inclusion of a fluid attenuating inversion pulse at TI = 1200ms (Inversion Time – time delay between inversion pulse and subsequent acquisition).

These inversion pulses (initial 180° rotations to bring all magnetization along $-z$) can be used to null signal from tissues with known T_1 times, given a judicious choice of TI. For a single (perfect) inversion pulse, the equation for tissue null time is well known:

$$\begin{aligned} M_z(t) &= M_o(1-2e^{-t/T_1}) \\ TI &= T_1 \ln(2) \end{aligned} \tag{3.1}$$

For a sequence involving multiple inversion recovery at a finite TR, the calculation of inversion time requires consideration of the saturation effects that occur due to repeated pulse structure. For a repeated inversion recovery pulse, it can be shown that the condition for tissue nulling becomes [42]:

$$TI = T_1 \ln\left(\frac{2}{1+e^{-TR_{eff}/T_1}}\right) \tag{3.2}$$

where TR_{eff} is an effective TR (2690 ms in the current case), which takes into account the train of 32 π pulses used in the CPMG experiment (during which time, no recovery of the magnetization takes place along the z axis). Given a CSF T_1 of 4500ms [42], the desired inversion time becomes 1153ms; in this study a TI of 1200 ms was used. Sagittal T_1 measurements were attempted in order to confirm this CSF T_1 value, but were met with limited success. An inversion recovery curve obtained from CSF voxels in an inversion recovery experiment is shown in figure 3.4. Substantial artefact and flow noise corrupted the image data, prompting the use of literature values for the T_1 of cerebrospinal fluid in the determination of the inversion recovery time TI.

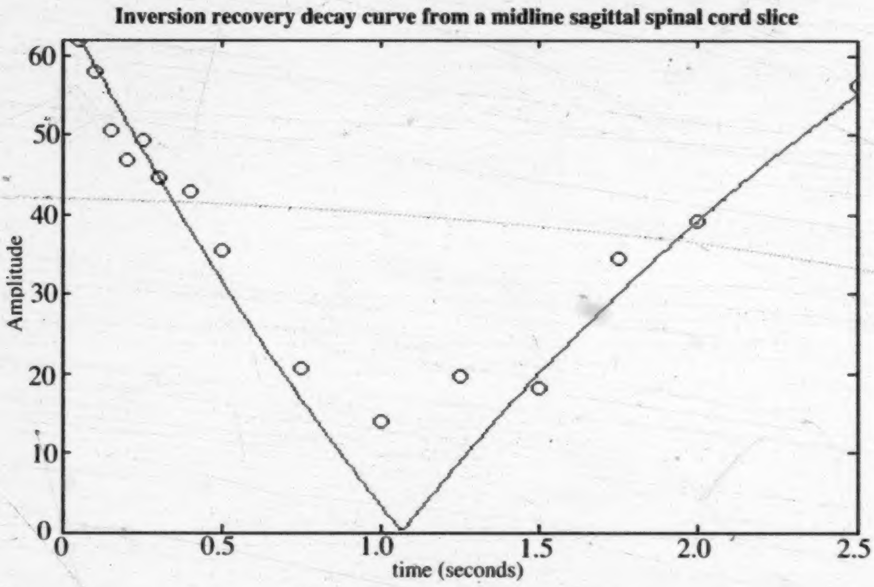

Figure 3.4 Inversion recovery curve from CSF voxels. Heart and breathing motion, in addition to CSF flow, contribute to noise in the decay curve, making accurate determination of CSF T_1 from a sagittal spinal slice difficult. Literature values for CSF time were accordingly used in the determination of TI.

3.1.4 T_2 Relaxation Analysis

Intensity decay curves were fit to the multi-exponential T_2 relaxation model using a least squares method developed in house [46]. . Recall that linear methods require a predefined T_2 partition that correspond to the *M* potential delta function constituents,

$$s(T_2) = \sum_{j=1}^{M} s_j \delta(T_2 - T_{2_j}) \tag{3.3}$$

Accordingly, data was decomposed into a set of 120 exponential terms, spaced logarithmically from 15ms to 2s. Regularized NNLS solutions were produced, with the regularizing algorithm imposing a 'minimization of the sum of the squares of the amplitudes' such that the constraint matrix **H** takes the form of the *j*×*j* identity matrix.

The value of μ given this additional constraint was adjusted such that the resulting χ^2 misfit value was allowed to increase to between 2% and 2.5% of its nominal value. The myelin water fraction, meanwhile, was defined as the fractionate contribution of those exponential terms with a T_2 between 15-40ms to the total signal.

Preliminary (20 echo) SC relaxation studies employing a Head RF coil have indicated that the presence of CSF contiues to complicate accurate MWF measurements, even when a fluid attenuating inversion pulse is used. Figure 3.5 shows 20 echo decay from both SC and attenuated CSF voxels. The rapid decay of CSF signal results in a large MWF when fit by NNLS software.

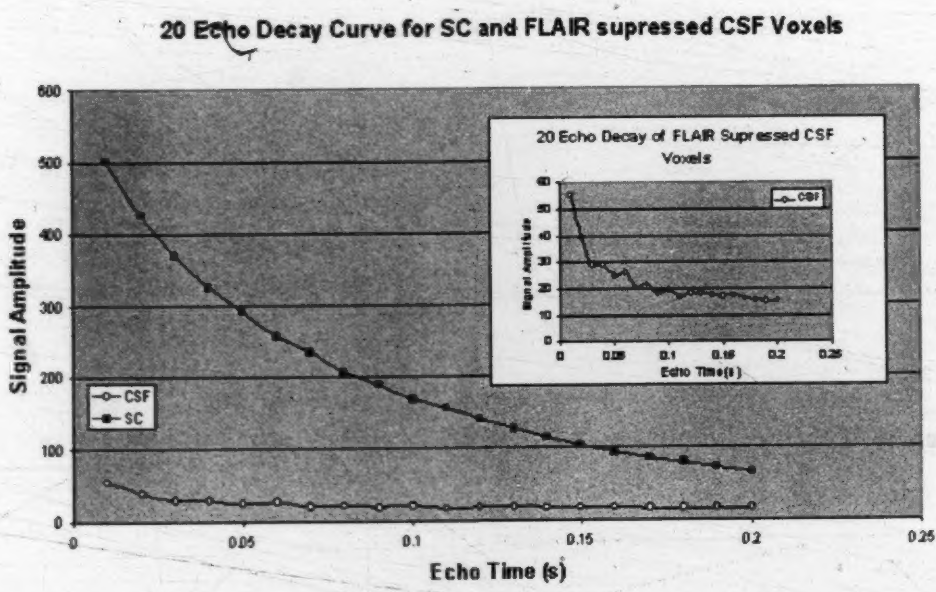

Figure 3.5 20 echo decay curve in human *in vivo* SC and CSF voxels, acquired using a modified fluid attenuating CPMG sequence. The rapid decay of CSF signal is fit to a short T_2 time and subsequently interpreted as myelin water.

Regularized solutions were used to construct 'myelin maps' – pixel by pixel graphical representations of myelin water fractions. Given the potential for misinterpretation of CSF noted above, voxel inclusion in the map was thresholded according to the constraints listed in Table 3.1.

Table 3.1 Parameter constraints employed in voxel thresholding.

Variable	Interpretation	Constraint	Motivation
DN	Voxel proton density. (extrapolation to signal at 0ms)	100-1500 units	Threshold supressed CSF voxels, and other fast relaxing noise artifacts.
GM	Geometric Mean T_2	10-100ms	Threshold unsupressed CSF voxels (CSF $T_2 \sim 2300$ms)
χ^2	Chi squared misfit	0-10	Eliminate pixels with poor fits to a multi-exponential model.
MWF	Myelin Water Fraction	0-0.7	Threshold voxels with extremely high myelin water fractions as biologically unfeasible.

Some representative 'myelin maps' resulting from the application of these thresholds to regularized NNLS solutions are illustrated in the results section.

3.2 Bovine *in vitro:* MRI

As mentioned, the human study was accompanied by *in vitro* experimentation using bovine SC samples in order to make independent measurements free from the constraints imposed by challenging physiological attributes of *in vivo* SC imaging.

3.2.1 Samples and Apparatus

Samples of fresh Bovine SC were acquired soon after slaughter (GrandMaison Beef Farm, Surrey) and were kept cooled in 0.1mM phosphate buffered saline. In an experiment repeated with spinal cords from two different animals, spinal cords were cut and arranged such that 8 (10) axial cross sections could be examined simultaneously. A GE Signa 1.5 T MRI unit was employed, using the Head RF coil to both transmit and receive. Samples were permitted to warm for 1/2 hour before scanning, which took place at 24°C.

3.2.2 Pulse Sequence and Data Acqusition

A 32 echo Poon-Henkelman CPMG T_2 relaxation sequence was employed, with a TE of 10ms, TR of 3000ms, FOV of 12cm X 12cm, acquisition matrix of 256 X 128, a slice thickness of 5mm and a corresponding RF bandwidth of 31.25 kHz, and 4 NEX. As surrounding fluid flow is not an issue *in vitro* no modifications (in the form of inversion recovery pulses) were necessary.

3.2.3 T_2 Relaxation Analysis

Data was decomposed into a set of 120 exponential terms, spaced logarithmically from 15ms to 2s. Both unregularized and regularized were produced, with the same 'minimum energy' regularizer as was used in the Human study, and the same definition of the myelin water fraction.

3.3 Bovine *in vitro:* NMR

Bovine samples were also used for NMR experimentation, which permits measurements at far greater SNR with a more rigorous sampling of the T2 decay curve.

3.3.1 Samples

Different samples from the same spinal cords employed in the MR study were used for NMR experimentation. These were kept cooled, and placed in a 10 mm outer diameter NMR tube. Phosphate buffered saline (0.1mM) was added to the samples to prevent dehydration, and reduce susceptibility artifact at air / tissue interfaces.

3.3.2 Apparatus

A modified Bruker SXP 4-100 NMR spectrometer was employed, operating at 2.1T (90MHz). Data acquisition involved a locally built pulse programmer [79], a Rapid Systems digitizer, a Nicolet 2090AR dual channel digital oscilliscope, and IBM compatible computer. Temperature was set using a Bruker B-ST 100/700 temperature controller which was used in conjunction with a controlled air flow device, and was set to 24°C.

3.3.3 Pulse Sequence and Data Acquisition

T_2 measurements were made on three spinal cord samples using a CPMG [80] sequence

$$90°_x(90°_{-x})-\left(\frac{\tau}{2}-180°_y-\frac{\tau}{2}-\right)_n \tag{3.4}$$

Due to the noise inherent to early datum, acquisition was started at 1ms. Four points were collected for each of the first 224 echoes, followed by every eighth echo up to 512, giving a total of 736 echoes. Experiments were preformed with interpulse delays (τ) of 100μs, 200μs, and 400μs, making the timescale of the measurements 432ms, 736ms, and 1728ms respectively. A delay of 10s allowed a return to thermal equilibrium before reapplications of the pulse sequence. CPMG measurements were made consecutively, starting with the 100μs experiment, and finishing with the experiment with the 400μs echo time. Each echo spacing experiment was preformed 200 times, and T_2 decay data was averaged to create the data set subsequently subjected to NNLS inversion, described in the next section.

3.3.4 T_2 Relaxation Analysis

Decay curves were decomposed using an NNLS routine with a partition of 120 T2 times, logarithmically spaced from 1ms to 5s. Regularized T2 distributions were constructed by allowing χ^2 to increase from 3-4% of it's nominal value. Myelin water fractions were calculated by considering the signal fraction from T_2 components 1-40ms.

Chapter 4: Results

4.1 Bovine *in vitro*: NMR

4.1.1 T_2 decay curves

NMR T_2 relaxation decay curves from each of the three fresh bovine SC samples studied are shown below, in figures 4.1, 4.2, and 4.3.

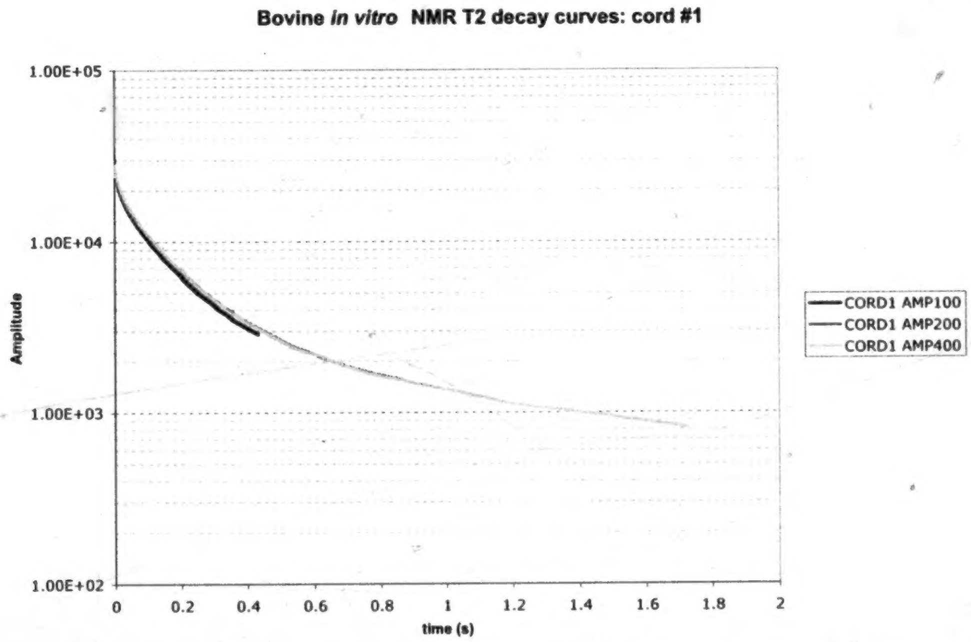

Figure 4.1 T_2 relaxation decay curves from 3 NMR experiments on sample #1: echo times were 100μs for the experiment labeled AMP100, 200μs for the experiement labeled AMP200, and 400μs for the experiment labeled AMP400.

The decay curves from cord #1 show little variability over the time course of the experiment, indicating that tissue integrity was maintained.

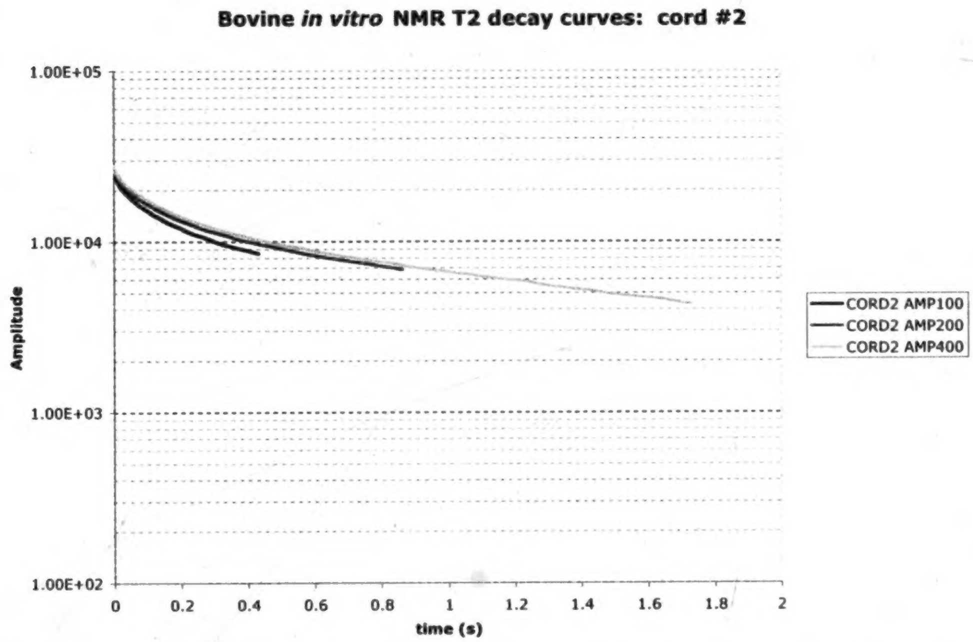

Figure 4.2 T_2 relaxation decay curves from 3 NMR experiments on sample #2: echo times were 100μs for the experiment labeled AMP100, 200μs for AMP200, and 400μs AMP400. Marked differences in the character of the decay curve during the experiment.

Sample 2 produced decay curves that exhibited a marked change from both cord #1 and cord #3, as well as changes during the time course of the measurement. A tendency towards a longer global T_2 time is noted with respect to the other two samples, and a shift towards longer relaxation times can be seen that coincides with the temporal order of the experiment (from the100μs echo time, through the 200μs echo time, to the 400μs echo time). This tendency towards longer relaxation times lacks a biological correlate: conceivable changes in time such as an increase in temperature, tissue degredation, or sample dehydration would be expected to shorten T_2 over time, and with respect to the other samples. A more likely explanation is a poorly tuned 180° pulse: the resulting reduced flip angle maintains less magnetization at the application of each 180 in CPMG sequence. The tendency towards longer T_2 times is therefore a result of the sampling density of the 100μs, 200μs, and 400μs experiments. It is noteworthy that although accidental in this case, this variable flip angle effect has been exploited in linear combination methods for short T_2 component estimation [81].

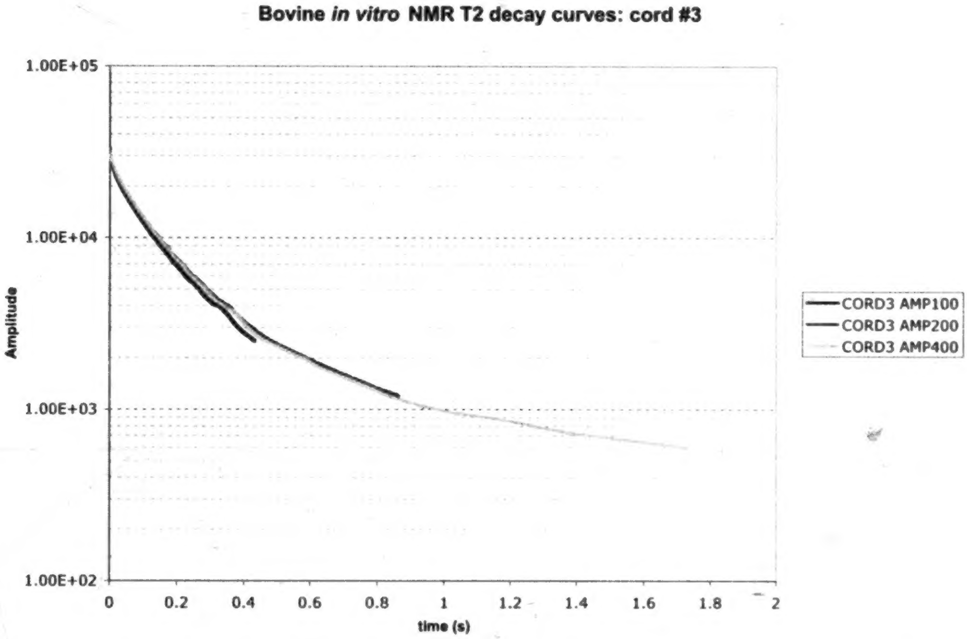

Figure 4.3 T_2 relaxation decay curves from 3 NMR experiments on sample #3: echo times were 100μs for the experiment labeled AMP100, 200μs for AMP200, and 400μs for AMP400.

Some features of the decay curve in the third sample are noteworthy. Decay curves from the experiment roughly coincide, suggesting that the apparatus was tuned and that tissue integrity was maintained. Secondly, there is a marked 'blip' occurring at approximately 0.35s in each experiment. The cause of this jump in the T_2 decay curve is unknown, but we expect that it is artifactual in origin, and probably a digitization error.

4.1.2 T_2 distributions

The decay curves above were subject to the mentioned regularized NNLS analysis, producing distributions shown below in figures 4.4, 4.5, and 4.6.

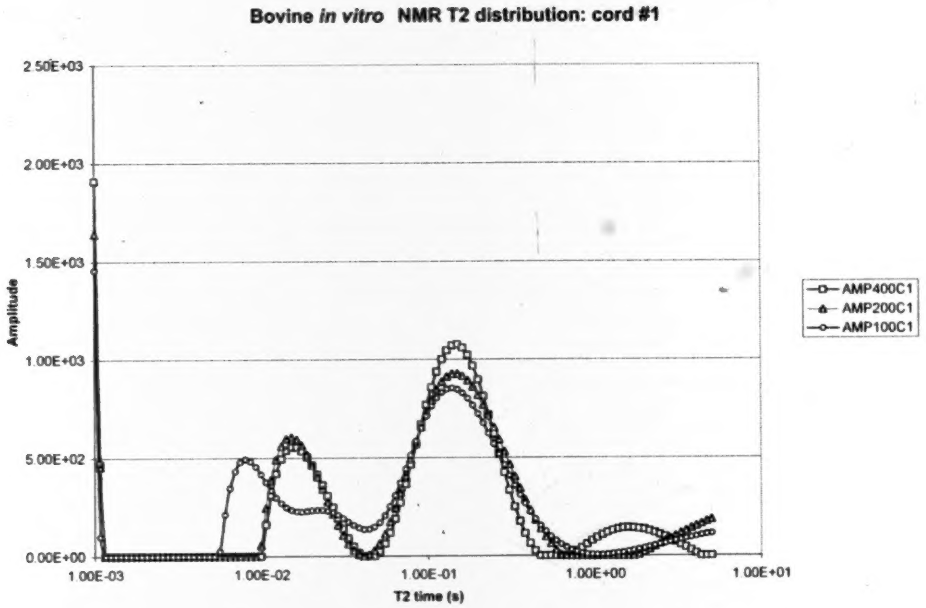

Figure 4.4 Regularized NNLS T_2 distribution for spinal cord sample #1.

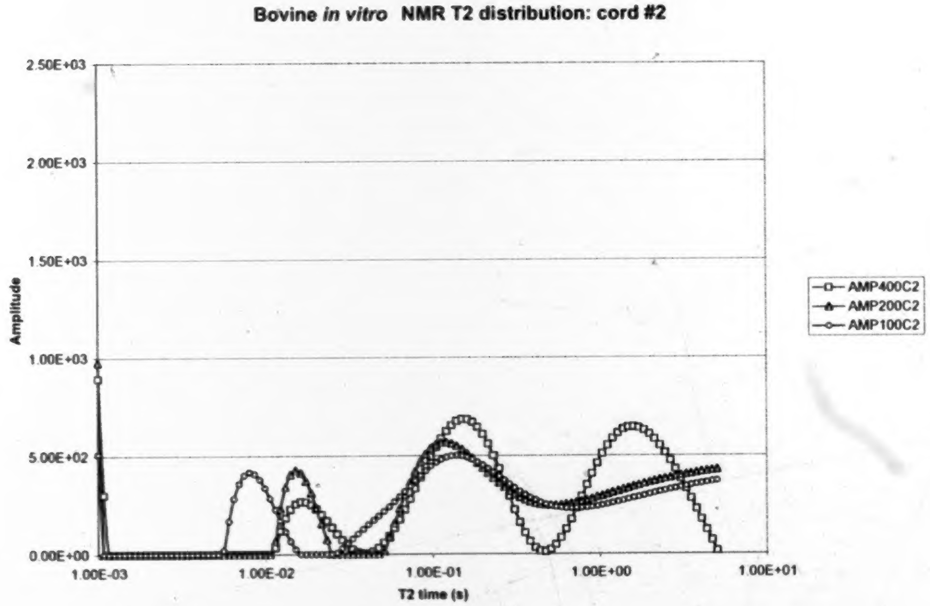

Figure 4.5 Regularized NNLS T_2 distribution for spinal cord sample #2.

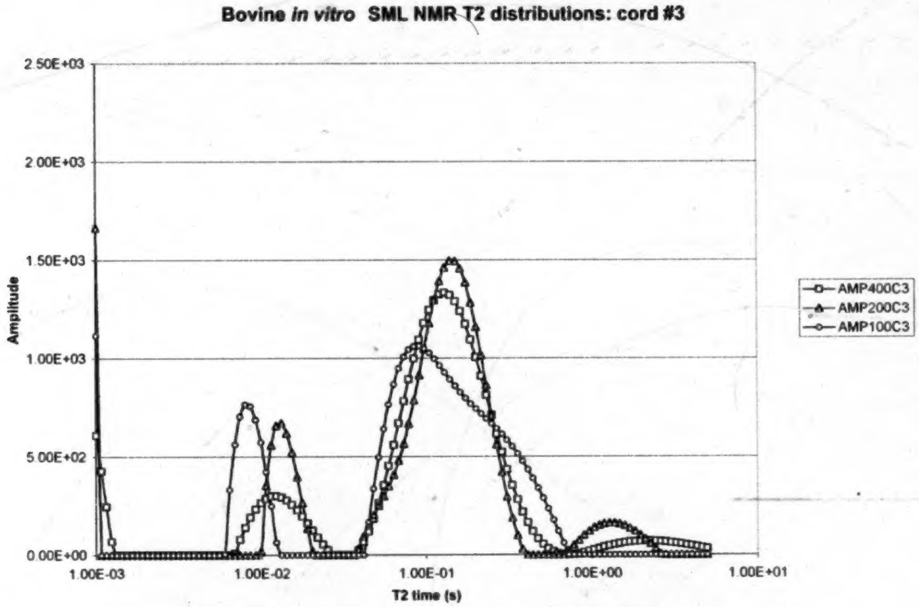

Figure 4.6 Regularized NNLS T_2 distributions for spinal cord #3.

Several features in the distributions above are worthy of further elaboration. Firstly, resolution of the last T_2 component was superior at the 400μs echo time, likely to do the longer acquisition window (1.7s) that this sampling density provides. This is especially marked in the case of cord #2, where AMP100 and AMP200 distributions are suggestive of exchange between the last two reservoirs on a T_2 timescale. That this merging of the latter two components was not observed at the 400μs spacing, however, suggests that this may be an artifact of a smaller acquisition window. The AMP100 experiment consistently resolved short T_2 times that were smaller (< 10ms) that those resolved at 200μs and 400μs (>12ms). This could potentially result from exchange processes that occur on the order of 100μs, however poorer characterization of the T_2 distributions as a whole could influence the determinations of T_2 times at the 100μs echo spacing.

A further anomaly was noted in the tendency for short T_2 peak to 'split' into two peaks, at approximately 8ms and 20ms respectively, depending on the extent of solution smoothing. The appearance of this shorter T_2 peak is not without precedence, it has been resolved in NMR T_2 distributions in crayfish abdominal cord [47], olfactory, trigeminal, and optic nerve of garfish [54], in non-regularized fits of the spinal cord of Hartley guinea pigs [51], in rat sciatic nerve [56], and in bovine brain [82]. Given its consistent resolution, there was initially some consideration that this might represent a novel diffusion restricted resevoir arising due to *in vitro* changes in cellular structure. The swelling of multilammelar mitchondria for instance, which under non-swollen conditions occupy more than 10% of the cytoplasmic volume in a nerve cell [83], offers one potential resevoir that could be diffusion restricted, and would likely have short relaxation times arising from elevated manganese content in mitochondrial fractions [84]. Webb *et al.* also raised the possibility the shortest T_2 represented a non myelin component, and noted that it acted to overestimate the size the resolved short T_2 component in fits of multi-exponential decay to a Gaussian model.

In CNS tissues, another possibility lays in asymmetrical myelin swelling characteristics, observed via X-Ray diffraction [85]. The CNS myelin swelling unit is that of 4 membranes – i.e. double membranes pairs remain in tact, with an accordingly smaller layer of hydration water between them. While it is unlikely that this would create a novel diffusion-restricted component, this could conceivably introduce a broader distribution of T_2 times for the myelinic compartment, to which NNLS might have a propensity to fit to distinct T_2 times. This would be consistent with the view of Stewart *et al.*, who attributed the shorter component as an artifact arising from fitting to a distribution of myelin water T_2 times. However, such a proposition is not consistent with the appearance of the additional short component in PNS nerve, where the swelling unit is that of a single membrane pair. In studies on garfish and crayfish, the shortest T_2 component was assigned to spurious solid signal arising from a pool of motionally averaged lipid protons,

We have included this short T_2 in our estimate of myelin water fraction, due to its spurious appearance in NNLS inversions of bovine spine. Much like Webb *et al* however, we note that it may be acting to increase the size of our measured myelin water fraction.

A failure to resolve separate components for intra and extra cellular water was noted, and marks a difference between these measurements and those made in other nerve samples [54, 86], including previous measurements in guinea pig spinal cord [51]. We feel this is largely a result of a shorter acquisition window and inferior SNR in this study relative to those mentioned, and subsequent reduced resolution of longer T_2 components.

The original motivation in performing NMR measurements was the creation of a 'gold standard' – a description of T_2 characteristics to which subsequent MRI based measures could be compared. Of the samples mentioned, our best fit, as measured by SNR_{fit} (standard deviation of fit residuals divided by extrapolated signal at t=0) was the data from 400μs measurement of cord #1, which gave an $SNR_{fit} > 1000$. Peak T_2 times (% signal) for this trial were 16ms (30.7%), 150ms (61.6%), and 1.59s (7.7%) which we feel represent diffusion restricted pools of myelin water, intra and extra – axonal water, and component buffer respectively. These measurements are substantially higher than those made in guinea pig spinal cord [51] or bovine brain [82] on the same apparatus, however they do mark agreement with similar measures in bovine optic nerve (short T_2 component amplitude of 32%) [74].

4.2 Bovine *in vitro*: MRI

As described in Chapter 3, T_2 relaxation was also measured using 32 echo sequence on a 1.5T clinical MRI scanner. Results from these measurements are shown below.

4.2.1 Decay curves and T_2 distributions

Representative decay curves from white matter, grey matter, and the whole spinal cord are shown in figure 4.7.

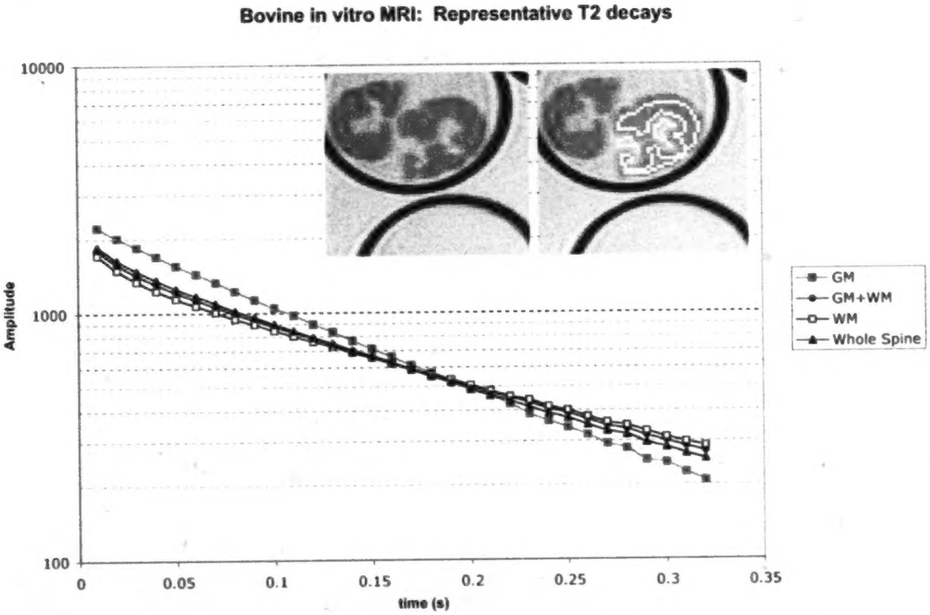

Figure 4.7 Representative decay curves from bovine SC. ROIs are shown (inset) in WM and GM regions. The "WM+GM" decay curve consists of data formed by addition of pixels in the WM and GM ROIs, while the 'Whole Spine" refers to an ROI encompassing the whole spinal cord.

The higher proton density of GM, as evidenced by grey matter's appearance as hyperintense in the inset 30ms echo image, results in a greater initial amplitude as shown in the GM decay curve. The WM and GM ROIs were drawn to avoid partial volumed voxels, as these contain information from tissue borders that would not be representative of either neighboring tissue. These partial volumed pixels do substantially contribute to the measured signal; this can be seen by deviations of the 'whole spine' decay curve from that containing a summation of pure WM and GM voxels.

The contribution of partial volumed voxels to the T_2 characteristics of the sample are also illustrated through the resulting T_2 distributions, shown in figure 4.8.

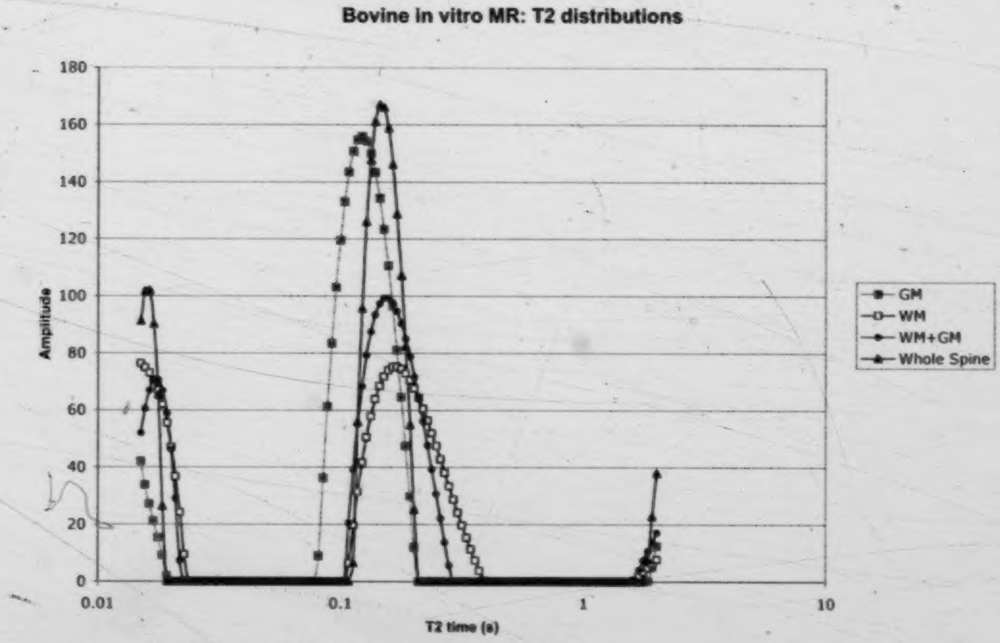

Figure 4.8 T_2 distributions resolved from the decay curves shown in Figure 4.7 for ROIs in GM, WM, GM+WM, and whole spine.

Increased short T_2 components of the 'whole spine' ROI, relative to that formed from a summing signal in from exclusively WM and GM regions, indicate that partial volumed voxels contribute substantially to the measured myelin water fraction. This partial voluming effect may also contribute to the short T_2 component seen in grey matter.

4.2.2 Myelin Water Fractions: Region of Interest Analysis

Regions of interest around areas expected to exhibit consistent tissue characteristics are often used in *in vivo* applications of quantitative T_2 measurement [48, 57, 59-62, 87]. The signal of all pixels within the ROI is averaged, and the resulting signal inverted using NNLS. The use of such volume averaging techniques results in significant gains in signal to noise, that scale with the square root of the number of pixels in the ROI in the limit of tissue homogeneity. Regions of interest were drawn on bovine white matter and grey matter ROIs, and the resulting exponential decay resolved to give the 'myelin water fractions' (10ms < T_2 < 40ms) shown below.

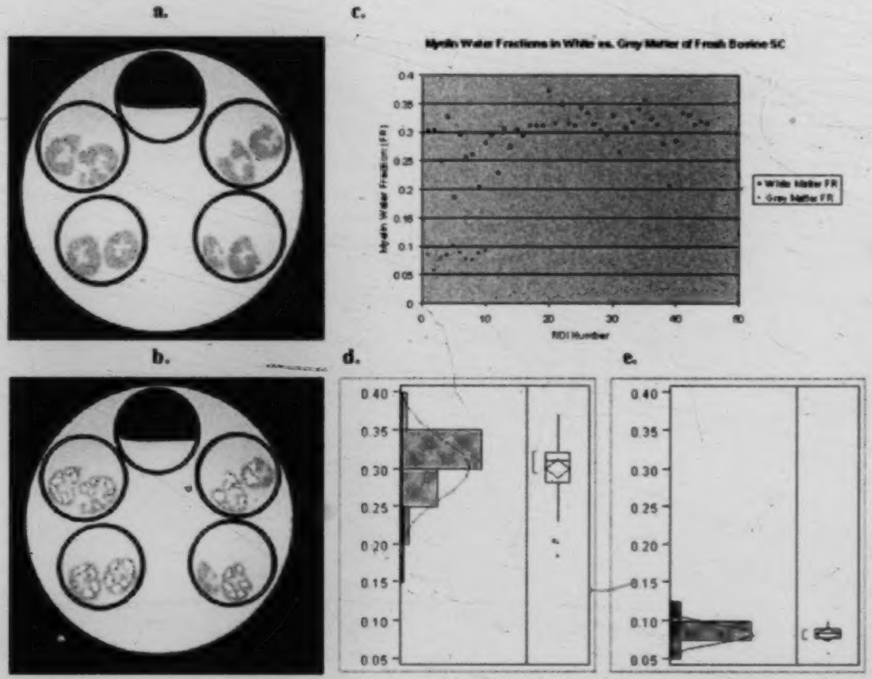

Table 4.9 ROI analysis of fresh Bovine SC. (a) 30ms echo image, (b) WM ROIs used in the analysis, (c) myelin water fractions for the 45 WM ROIs and the 10 GM ROIs, (d) distribution of white matter values, (e) distribution of GM values. Mean myelin water fractions (±Standard error) for the two regions was .300 (±0.006), and 0.082 (±0.004).

Volume averaging trades away potential information about tissue heterogeneity for increased signal to noise. If smaller scale tissue characteristics are of interest, an appropriate analysis would be to invert each voxel individually, and compute solution statistics. ROIs were accordingly drawn around WM and GM areas in all 18 transverse SC sections examined, resolving the distrubutions of short (10-30ms, non regularized fit) T_2 signal fractions within WM and GM shown in figure 4.10

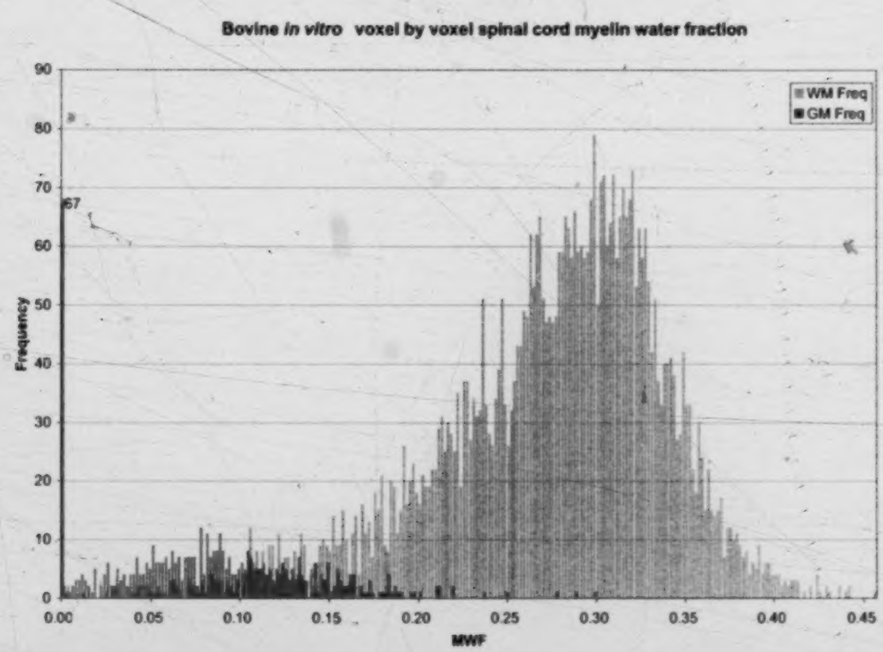

Figure 4.10 Myelin water fractions for pixels within defined WM and GM ROIs in transverse sections of fresh bovine SC. Two distributions are seen for grey matter and white matter respectively. Mean (±SE) values for white matter voxels was 0.269 (±0.001), while for grey matter voxels it was 0.080 (±0.002).

The means for the two methods (average – invert vs. invert – average) are within one standard deviation of each other; we expect that the difference arises from increased noise resulting from the histogram produced through an invert-average methodology.

Substantial tissue heterogeneity was observed given the considerable overlap between white matter and grey matter short T_2 distributions. One potential source of this overlap is probed in the next section.

4.2.3 Voxel by Voxel Inversion

Voxel by voxel inversions can be visualized by assigning grey scale values to solution characteristics. This is often done with the myelin water fraction in the production of 'myelin water maps' [48]. A myelin water map created from bovine SC relaxation data is shown below

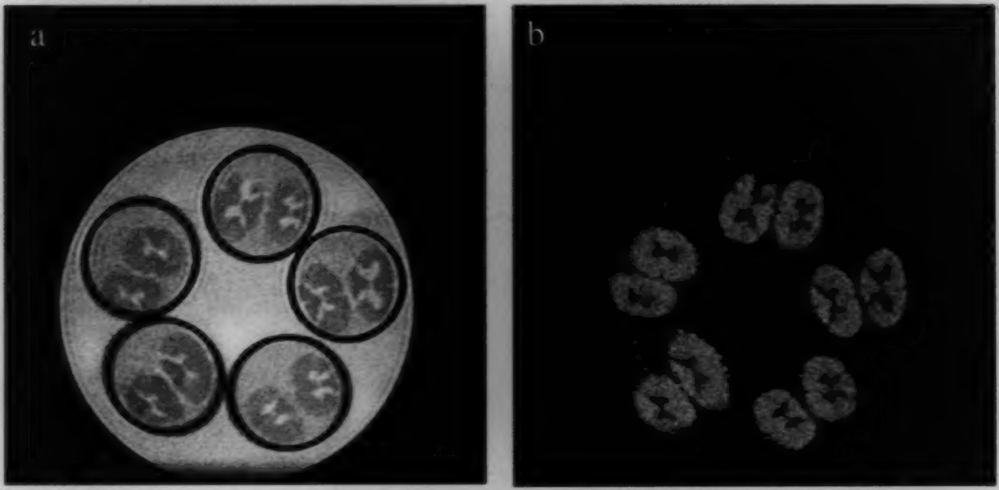

Figure 4.11 Myelin water map created from bovine spinal cord. Grey matter regions, seen as hyperintense on the 30ms echo image shown in (a), are resolved as having a lower myelin water fraction in (b).

Voxel by voxel visualization can also help us explore the nature of the overlap seen in the distributions of what we would normally expect to be completely distinctive tissue types. Selecting for those voxels with 'intermediate' myelin water fractions (0.1 < MWF < 0.2) yields the following:

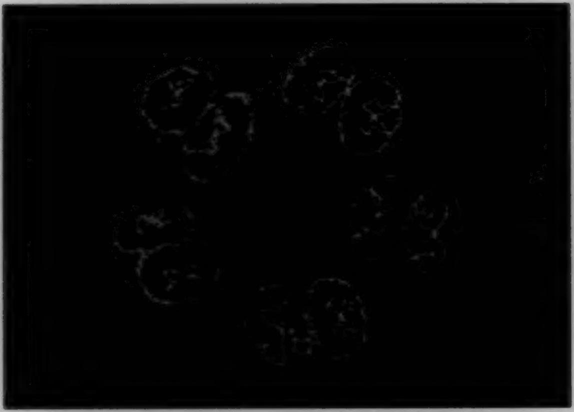

Figure 4.12 Selective visualization of intermediate myelin water fraction values reveals the effects of partial voluming on myelin water content distributions.

Figure 4.12 illustrates the partial voluming effect that occurs on tissue boundariesdue to the obtrusion of a voxel onto tissue borders. Intermediate myelin water fractions are clearly resolved on borders between white matter and grey matter, and white matter and the surrounding PBS.

4.3 Human *in vivo*

As mentioned in Chapter 3, 22 multi-echo T_2 relaxation measurements were made on humans *in vivo* in a sagittal scan plane. Regional T_2 characteristics were compiled, and are described in the sections below.

4.3.1 Decay curves and T_2 distributions

The preparatory inversion recovery pulse at TI = 1200ms, necessitated due to the presence and motion of CSF, results in significant costs in signal to noise. This is illustrated in figure 4.13, where a 32 echo signal from spinal cord is shown with one from brain, where an IR preparatory pulse is not used in the CPMG measurement.

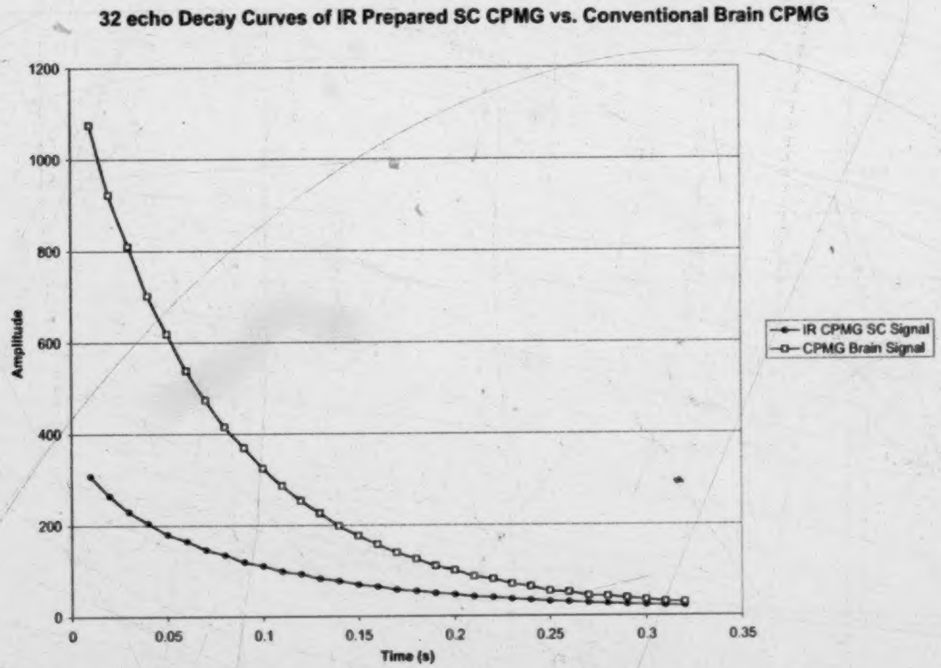

Figure 4.13 Signal from a Brain CPMG vs. IR prepped spine CPMG experiment. The inversion recovery pulse results in significant costs in terms of signal to noise ratio of the acquired decay curve.

The effects of the inversion recovery pulse are clearly seen: a drastic cut in signal amplitude occurs as a result of the preparatory 180° inversion. The theoretical signal (magnetization) available for imaging from the IR-CPMG squence depends the T_1, T_2, and proton density (ρ) of the tissues involved. In the limit of a perfect inversion, this maximum signal can be shown to be [42]

$$\frac{M_{IR-CPMG}}{M_o} = \rho\left|1 + e^{-TR_{eff}/T_1} - 2e^{-TI/T_1}\right| \tag{4.1}$$

Where TR_{eff} is the effective TR, which takes into account the subsequent train of 32 π pulses. Meanwhile, for the CPMG sequence, there is no inversion pulse to exacerbate T_1 effects, giving the following expression for initial signal [42]

$$\frac{M_{CPMG}}{M_o} = \rho(1 - e^{-TR/T_1}) \tag{4.2}$$

If we assume average ρ and T_1 values for brain WM,GM, and CSF given in table 4.1, and sequence-appropriate values for TR and TI, the theoretical signal loss becomes wholly dependent on the relative contribution of the respective (WM, GM, CSF) tissue volumes. If we make the simplification that a voxel will contain only white matter and grey matter (which is particularly well founded in the IR-CPMG case, where the CSF signal is effectively nulled), we can compute the theoretical signal loss of the IR-CPMG relative to the CPMG experiment as a function of the fractional grey matter content. This relationship is plotted in figure 4.14.

Table 4.1 Spin Density and T_1 values in White and Grey Matter

Tissue	Spin Density ρ (relative)	T_1 (ms)
White Matter	0.708	756
Grey Matter	0.832	1200
Cerebrospinal Fluid	1.0	4500

Table 4.1 Spin density and T_1 values used in the calculation of the effects of the IR pulse on signal in a IRCPMG measurement. Values for brain white and grey matter were taken from Whittal *et al.* [27], CSF equivalents from Haacke *et al.* [42].

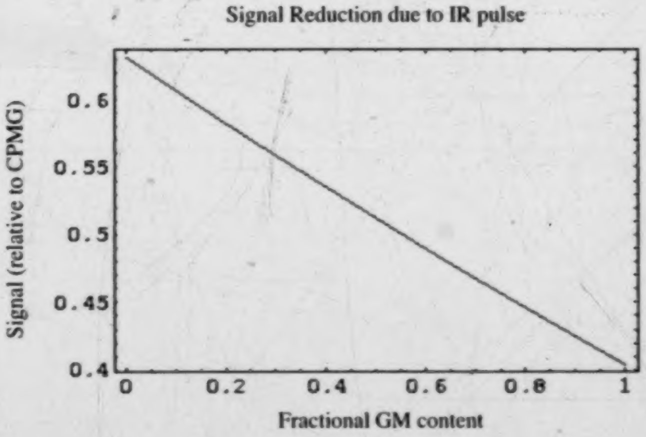

Figure 4.14 Relative signal in the IR-CPMG with respect to conventional CPMG, expressed as a function of voxel grey matter content.

As can be seen in figure 4.14, the signal in the IR-CPMG ranges from 40% (at 100% GM) to 63% (at 100% WM) of its CPMG predecessor. The signal will therefore depend on the relative grey matter content of the voxel, which varies along the cranio-caudal direction in spinal cord as we saw in Chapter 1.

Such cuts in signal amplitude are particularly worrying considering that signal to noise is a particulary important parameter with respect to quantitative T_2 measurement and analysis [69, 70]. We defer a more comprehensive treatment of these issues to the discussion, and simply note here that we found that NNLS *was* able to resolve T_2 distributions despite the significant cutback in SNR; some representative distributions are shown in figure 4.15.

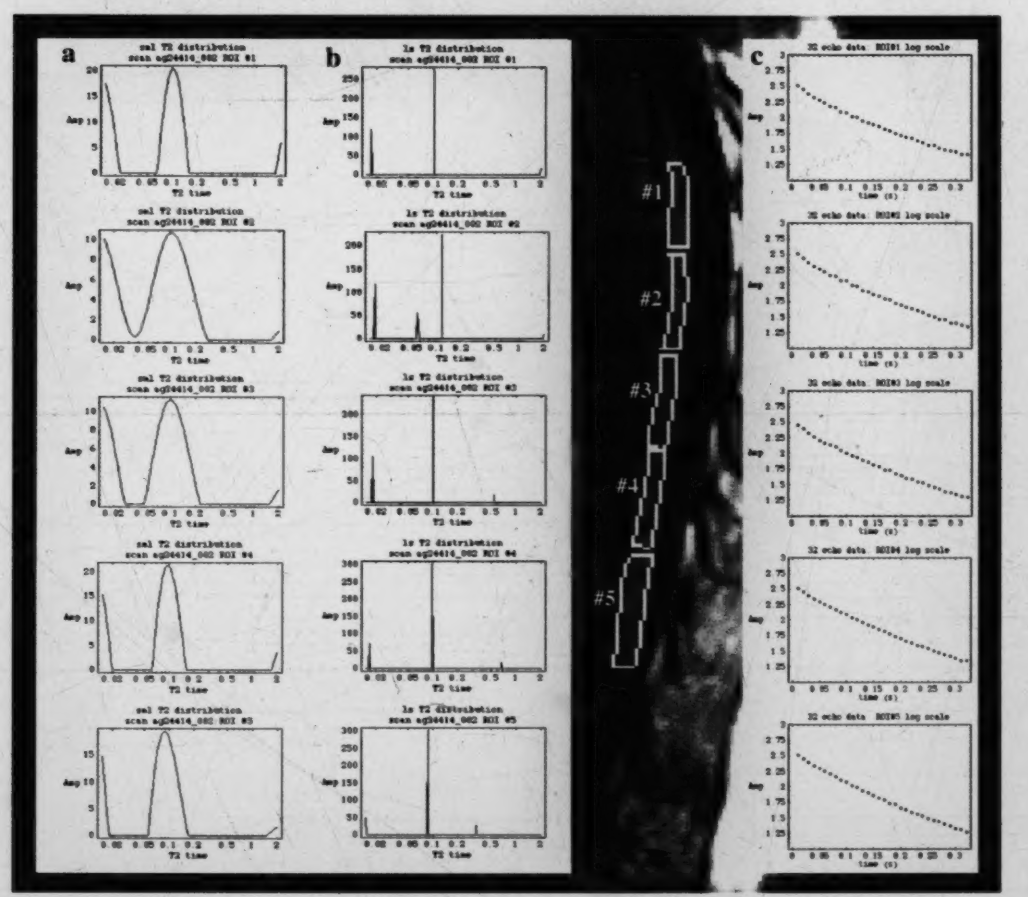

Figure 4.15 Regularized (**a**), and non regularized (**b**) T_2 distributions obtained from NNLS inversion of decay curves (**c**) from the ROIs shown above. The top distributions / decay curve correspond to the most rostral ROI, and they descend through progressively caudal regions of interest.

4.3.2 Regional Changes in Myelin Water Fraction

Regions of interest were drawn on all subjects as shown in figure 4.15. Averaging all scans with respect to SC location (indexed in space with reference to adjacent vertebrae) resolved regional variations in myelin water fraction, shown below in figure 4.16.

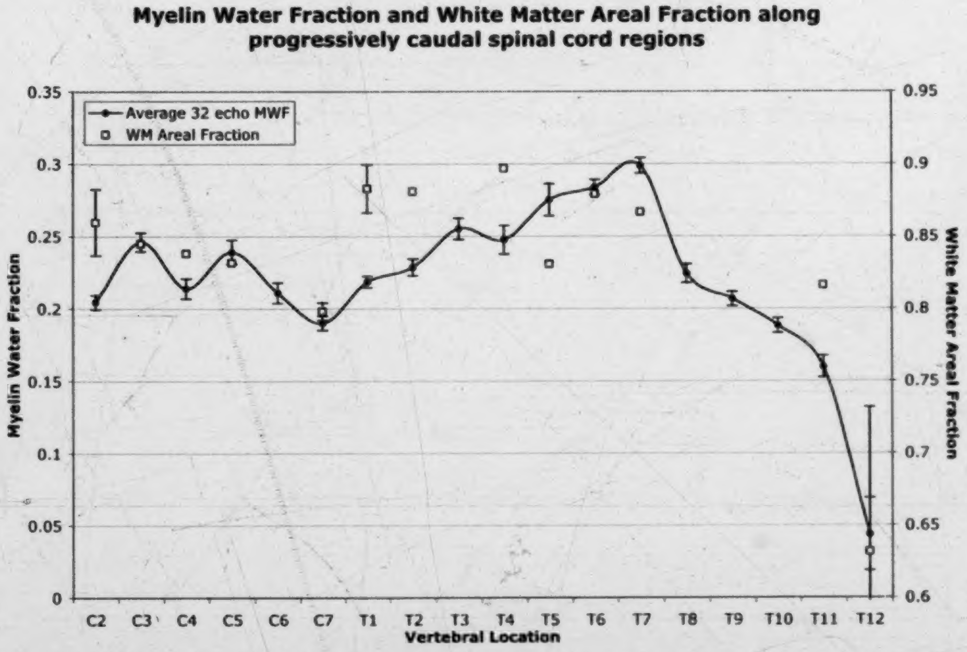

Figure 4.16 Myelin water fractions measured in progressively caudal regions of interest adjacent to the listed vertebrae. Varations in myelin water content follow a pattern consistent with the physiological distribution of white matter, as determined by the areal fraction of white matter on myelin stained micrographs averaged from [88-91]. Error bars in WM Areal Fraction indicate that point in an average from the sources above, points without error bars were only given in [88].

An advantage to myelin water measurement in the spinal cord is that the relative WM / GM content is well defined, and can be easily quantified through histological measures. This makes the spinal cord a particularly attractive system to evaluate the accuracy of myelin water fraction measurement. White matter and Grey matter regions in photomicrographs of myelin stained tranverse spinal cord sections from reference histology textbooks [88-91]. were quantified using a user assisted edge finding algorithm (Image-Pro Plus, Silver Spring MA). Care was taken to account for the multiple SC levels that can be found adjacent to single vertebrae by taking the average of those areal

WM fractions. The resulting values for the areal fraction of white matter, expected to correlate with the myelin water fraction, are also shown on figure 4.16. The correlation between the two is significant: a weighted regression reveals an adjusted R^2 of 0.75, with $P < 0.00006$.

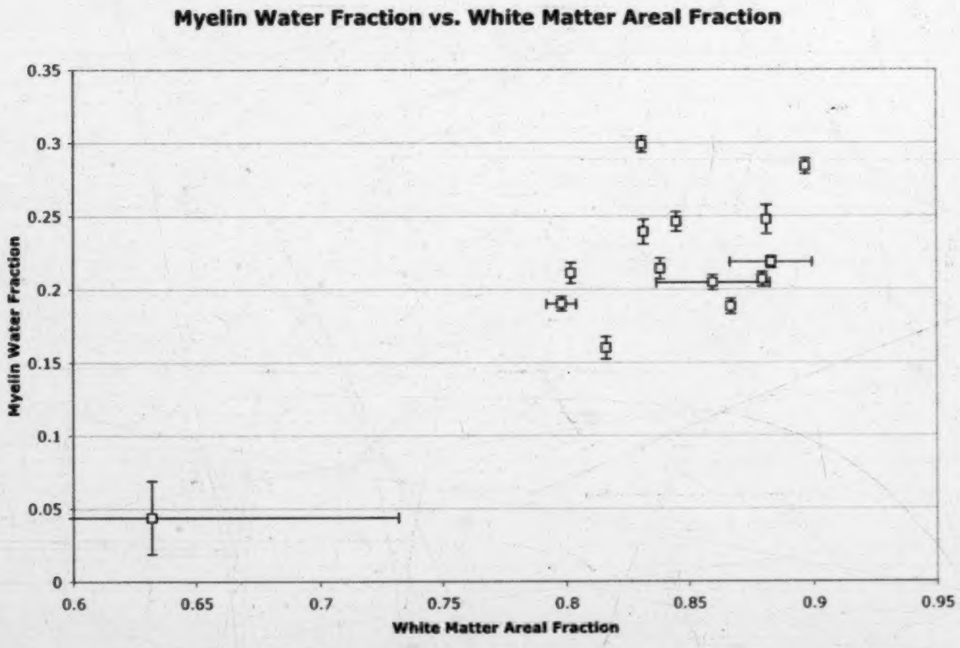

Figure 4.17 Scatterplot showing IR-CPMG myelin water fraction versus the areal white matter fraction as measured in tranverse myelin stained photomicrographs. A weighted linear regression found a significant correlation between the two, with R^2 of 0.75, at $P < 0.00006$.

It is noteworthy, however, that determinations of MWF and WM areal fraction at vertebral T12 (corresponding to SC L2-S5) are largely responsible for this correlation; a weighted regression in the absence of this point reduces the adjusted coefficient of determination to R^2=0.04, with P=.52. Physiologically, vertebral T12 can span spinal cord levels L2 through S5, encompassing diameters from ~8.6mm (lumbar enlargement, ~L3), and to ~3.25mm (S5); this drop in diameter could introduce partial volume effects in the area. Normalizing the measured myelin water fraction to the WM areal fraction for all points yields an average of 0.26 ± SD 0.04; meanwhile a similar normalization at T12 yields an adjusted MWF of 0.07. This suggests that the measurement in that area could be anomalous.

To test mean vertebral ROIs against each other, a two-tailed students t-test was applied, the resulting inter-vertebral P-values are shown in table 4.2. While it has been suggested that in the application of multiple t-tests, P-values should be modified vis a vis a bonferroni adjustment, we agree with the recommendations of Perneger with respect to the application of such techniques [92] and simply caution the reader as to the methodology employed.

Table 4.2 P values from inter-vertebral comparisons of myelin water content

	C2	C3	C4	C5	C6	C7	T1	T2	T3	T4	T5	T6	T7	T8	T9	T10	T11	T12
C2	▨	0.110	0.549	0.136	0.723	0.632	0.366	0.198	0.066	0.169	**0.037**	**0.002**	**0.000**	0.387	0.494	0.600	0.126	**0.006**
C3	0.110	▨	0.327	0.925	0.196	**0.044**	0.235	0.655	0.809	0.973	0.465	0.143	0.060	0.520	0.346	**0.037**	**0.009**	**0.002**
C4	0.549	0.327	▨	0.375	0.790	0.299	0.946	0.531	0.218	0.379	0.117	**0.013**	**0.004**	0.753	0.930	0.276	0.057	**0.005**
C5	0.136	0.925	0.375	▨	0.232	0.060	0.296	0.730	0.733	0.906	0.411	0.118	**0.048**	0.573	0.390	**0.043**	**0.009**	**0.002**
C6	0.723	0.196	0.790	0.232	▨	0.412	0.672	0.345	0.120	0.252	0.062	**0.004**	**0.001**	0.560	0.716	0.381	0.070	**0.004**
C7	0.632	**0.044**	0.299	0.060	0.412	▨	0.090	0.083	**0.028**	0.100	**0.017**	**0.000**	**0.000**	0.234	0.289	0.906	0.220	**0.006**
T1	0.366	0.235	0.946	0.296	0.672	0.090	▨	0.467	0.148	0.326	0.065	**0.002**	**0.000**	0.757	0.968	0.165	**0.026**	**0.000**
T2	0.198	0.655	0.531	0.730	0.345	0.083	0.467	▨	0.473	0.669	0.236	**0.040**	**0.013**	0.791	0.574	0.068	**0.011**	**0.001**
T3	0.066	0.809	0.218	0.733	0.120	**0.028**	0.148	0.473	▨	0.856	0.587	0.219	0.101	0.357	0.215	**0.016**	**0.003**	**0.001**
T4	0.169	0.973	0.379	0.906	0.252	0.100	0.326	0.669	0.856	▨	0.526	0.217	0.112	0.517	0.360	0.051	**0.010**	**0.004**
T5	**0.037**	0.465	0.117	0.411	0.062	**0.017**	0.065	0.236	0.587	0.526	▨	0.624	0.404	0.180	0.100	**0.008**	**0.003**	**0.001**
T6	**0.002**	0.143	**0.013**	0.118	**0.004**	**0.000**	**0.002**	**0.040**	0.219	0.217	0.624	▨	0.675	**0.035**	**0.012**	**0.000**	**0.000**	**0.000**
T7	**0.000**	0.060	**0.004**	**0.048**	**0.001**	**0.000**	**0.000**	**0.013**	0.101	0.112	0.404	0.675	▨	**0.012**	**0.003**	**0.000**	**0.000**	**0.000**
T8	0.387	0.520	0.753	0.573	0.560	0.234	0.757	0.791	0.357	0.517	0.180	**0.035**	**0.012**	▨	0.790	0.145	**0.019**	**0.004**
T9	0.494	0.346	0.930	0.390	0.716	0.289	0.968	0.574	0.215	0.360	0.100	**0.012**	**0.003**	0.790	▨	0.202	**0.025**	**0.003**
T10	0.600	**0.037**	0.276	**0.043**	0.381	0.906	0.165	0.068	**0.016**	0.051	**0.008**	**0.000**	**0.000**	0.145	0.202	▨	0.187	**0.010**
T11	0.126	**0.009**	0.057	**0.009**	0.070	0.220	**0.026**	**0.011**	**0.003**	**0.010**	**0.003**	**0.000**	**0.000**	**0.019**	**0.025**	0.187	▨	0.194
T12	0.268	0.072	0.180	0.070	0.195	0.363	0.117	0.076	**0.041**	0.075	**0.039**	**0.007**	**0.003**	0.095	0.107	0.310	0.879	▨

Table 4.1 P values resulting from the application of two-tailed student's t-tests to SC adjacent to the listed vertebral regions. Significant ($P<0.05$) differences are shown in shaded, bold faced cells. P values shown as zero (0.000) resulted due to rounding to 3 decimal places.

The results comparison via inter-vertebral t-tests suggests a natural grouping of results based on regional differences in myelin water fractions. Cells with more that 5 significant t-tests were grouped with any neighbors also showing more that 5 such results, resulting in 6 groups (3 created from regional differences, 3 created by default). Averaging myelin water fraction in these bins results in more natural progression of myelin water content, shown below in figure 4.18

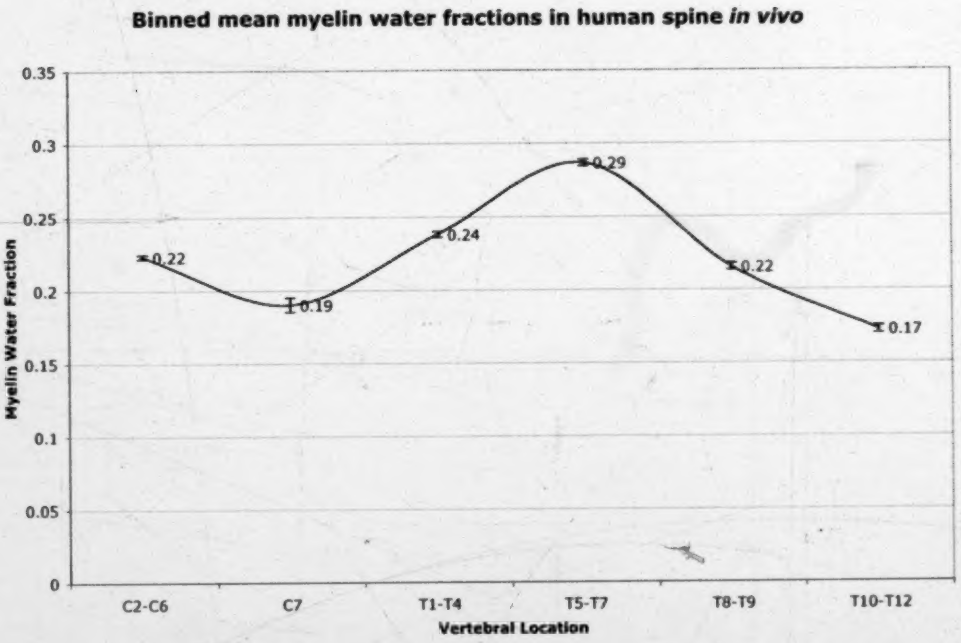

Figure 4.18 Average myelin water fractions, binned according to regional differences as determined by t-test results. Error bars indicate standard error.

The groups formed by binning according to statistical significance ($P < 0.05$) roughly correspond with physiological expectations for the cervical enlargement (~C7), and lumbar enlargements (~T10-T12), and thoracic spinal cord, where the highest myelin water fractions were expected. Myelin water fraction values in thoracic cord are in good agreement with those NMR and MR CPMG measurments with bovine white matter, and bovine optic nerve [74], consistent with the expectation of a small contribution of grey matter to total signal in a sagittal slice through the area. Measured MWF in this study is also consistent with determinations in rat spinal cord [31], and with other recently reported measurements in human spinal cord [29, 30].

4.3.3 Voxel by Voxel Inversion

Voxel by voxel regularized NNLS solutions were computed and subjected to the filtering constraints outlined in table 3.1 to produce graphical representations of the myelin water fraction, shown in figure 4.19.

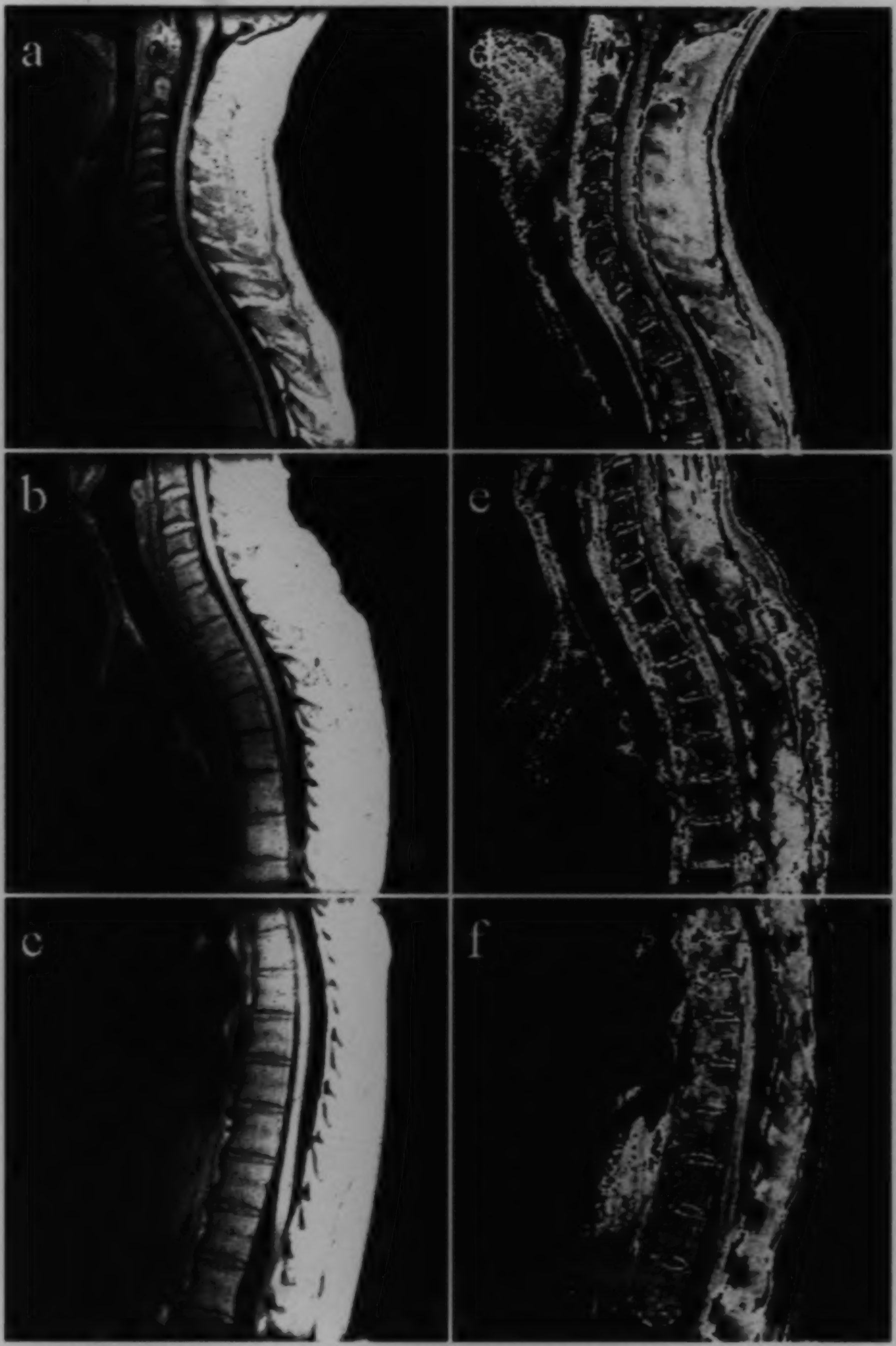

Figure 4.19 10ms echo images from cervical (a), thoracic (b), and lumbar (c) 32 echo acquisitions. Corresponding myelin maps are shown in (d),(e), and (f) respectively.

These myelin maps illustrate some challenges and some noteworthy successes of this spinal T_2 relaxation study. Firstly, unlike head scans, spine scans using the phased array coil encompass a wide array of physiology, some of which (subcutaneous and epidural fat, for example) also have a short T_2 water fraction arising from analogous interactions between water protons and lipid membranes. This is clearly seen in the myelin maps shown in figure 4.19.

The mentioned difficulties in capturing the spinal cord within a single slice encompassing the entire field of view can be seen in (b), where the gradual fading of signal intensity and SC profile indicates it has fallen out of the image plane. This is likewise resolved in the associated myelin map (e), with lower myelin water fractions being resolved caudally.

It is noteworthy that all lumbar myelin maps resolved an inferior central band of reduced myelin water content, the location of which was consistent with the expected location of the lumbar enlargement. This observation is illustrated in figure 4.20.

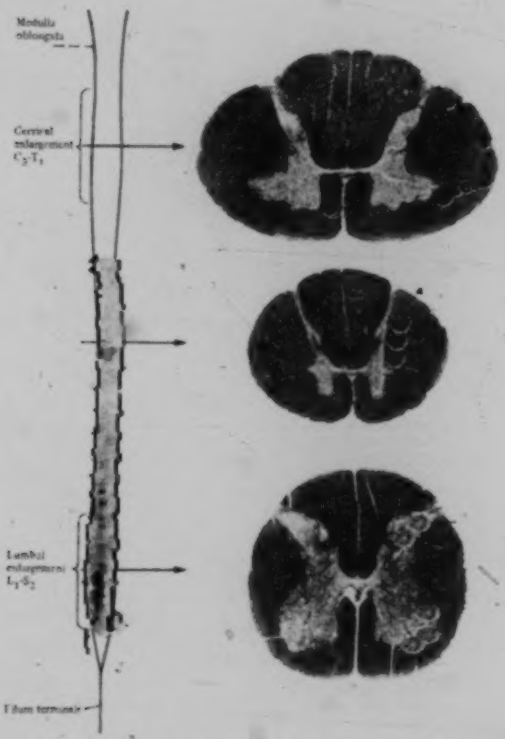
Medulla oblongata
Cervical enlargement C_5-T_1
Lumbar enlargement L_1-S_2
Filum terminale

Figure 4.20 Superposition of a myelin map from a lumbar acquisition onto figure 1.1 (adapted from [1]), demonstrating sensitivity of voxel by voxel inversion to reduced myelin content in the lumbar enlargement.

Similar effects (i.e. a lower voxel by voxel MWF measurment) was not seen in sagittal acquisitions of the cervical enlargement, consistent with the greater WM content in a midline sagittal cervical slice. However, an axial acquisition at C7 does demonstrate sensitivity to white matter distribution in the cervical enlargement, as shown in figure 4.21.

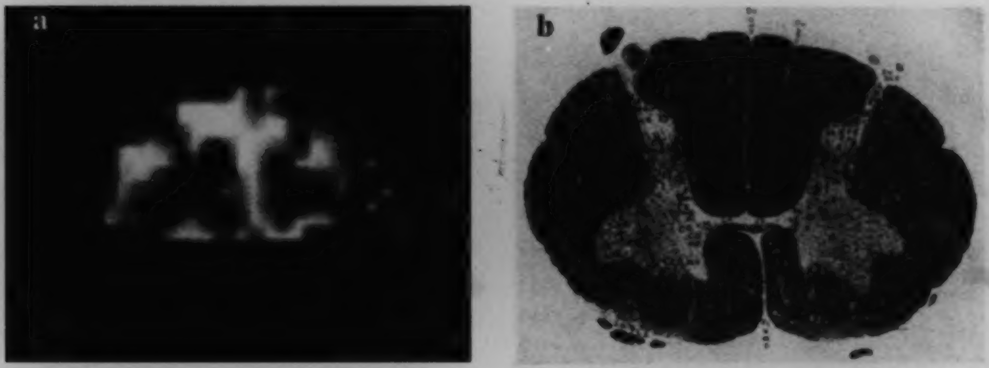

Figure 4.21 (a) Axial acquisition at vertebral C7 demonstrating sensitivity to myelin content in a spinal cord transverse plane in humans *in vivo*., as can be seen through a comparison with a reference histological transverse slide from the same area **(b)** (Adapted from [88]).

Sensitivity to physiological white matter distribution was hoped for in region of interest analysis; this optimism was founded upon the compensatory effect of averaging signal from a group of voxels in the face of reduced SNR, and having these results further refined by inter-study averaging according to physiological location. The resolution of physiologically consistent myelin water determinations *in vivo* on a case by case, pixel by pixel basis is encouraging with respect to potential applications of these techniques in monitoring the heterogeneity of MS pathology, or the spatial / temporal characteristics of putative demyelinating therapies.

Chapter 5: Discussion

5.1 Signal to Noise Ratio and IR-CPMG

As some authors have pointed out, the inversion of multiecho T_2 data into multicomponent temporal distributions imparts requirements in signal to noise [69, 70]. Based on a criterion of 'admissibility' (defined as a solution returning the correct number of components, with a 10% standard deviation in T_2 amplitudes and times) Graham *et al.* used Gaussian distributed inputs to examine solution characteristics at different SNR and sampling protocols. They found that imaging conditions typical of *in vivo* quantitative T_2 measurement (SNR ~ 100, TE=10ms, 32 echoes) were inadequate to resolve T_2 characteristics on a pixel by pixel basis. They suggest, however, that a judicious choice of solution regularizer, in conjunction with consideration of signal from a larger volume, can provide data which, when inverted, provides admissible statistics. Fenrich *et al.* likewise addressed acquisition and processing issues in multi-echo relaxation measurements, which we consider here in the context of T_2. They clarified SNR and sampling requirements by quantifying relationships between adjacent T_2 peaks. Their methods include the definition of the Relative Peak Separation, *S*, as

$$S = \frac{(T_{2a} - T_{2b})}{\frac{1}{2}(T_{2a} + T_{2b})} \tag{5.1}$$

(where and T_{2a} and T_{2b} are adjacent peaks in the T_2 distribution). Meanwhile, they define the Resolution, *R*, to be

$$R = \frac{h_{av} - h_{dip}}{h_{av}} = 1 - \frac{h_{dip}}{h_{av}} \tag{5.2}$$

where h_{av} and h_{dip} are the average height, and the height of the 'dip' between two adjoined T_2 peaks, as shown in figure 5.1.

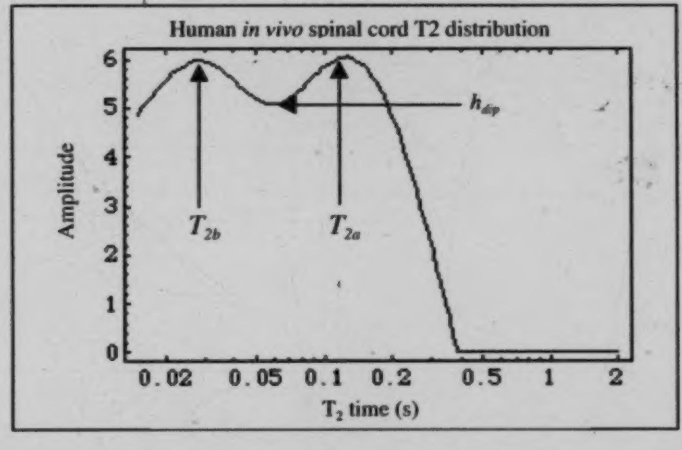

Figure 5.1 Incompletely resolved T_2 distribution from human spinal cord *in vivo* showing the parameters T_{2a}, T_{2b}, and h_{dip} employed in the definition of *R* and *S* (equations 5.1,5.2)

By sampling Gaussian inputs logarithmically at a minimum of 10 points / decade, Fenrich *et al.* characterized the signal to noise requirements for resolution of peaks at different values of *S*. Also citing typical *in vivo* imaging conditions of SNR ~100, they noted that at the 20% peak width of their input data, a relative separation of 1.35 (i.e. $T_{2b}/T_{2a} \sim 5$) was required to obtain R values greater than zero.

T_2 values typically assumed for myelin and intra / extracellular water *in vivo*, namely 10-50ms and 80-120ms, find themselves dangerously close to marginal resolution based on the analysis of Fenrich *et al* at clinical SNR. Nonetheless, quantitative T_2 has demonstrated sensitivity to myelination in different white and grey matter structures, the ability to monitor pathological changes in white matter diseases, and sensitivity to expected white matter content in the spinal cord *in vivo*. We therefore expect that it should be possible to rectify current *in vivo* T_2 techniques with the warnings outlined by the mentioned authors.

Most imaging techniques, including clinical quantitative T_2, create magnitude images from the Fourier transformation of complex *k*-space data. If one assumes that the noise in both real and imaginary channels is Gaussian, it can be shown that the noise in the resulting magnitude image is Rician distributed [93], implying that it can be described with the following probability density function:

$$P(x) = \frac{x}{\sigma^2}\exp\left(-\frac{\mu^2 + x^2}{2\sigma^2}\right) I_o\left(\frac{\mu x}{\sigma^2}\right) \tag{5.3}$$

where σ is the standard deviation, μ is the mean, and $I_o(x)$ is a modified Bessel function of the first kind [71]. The Rice distribution has a characteristic dependency on the ratio of μ/σ, as shown below in figure 5.2

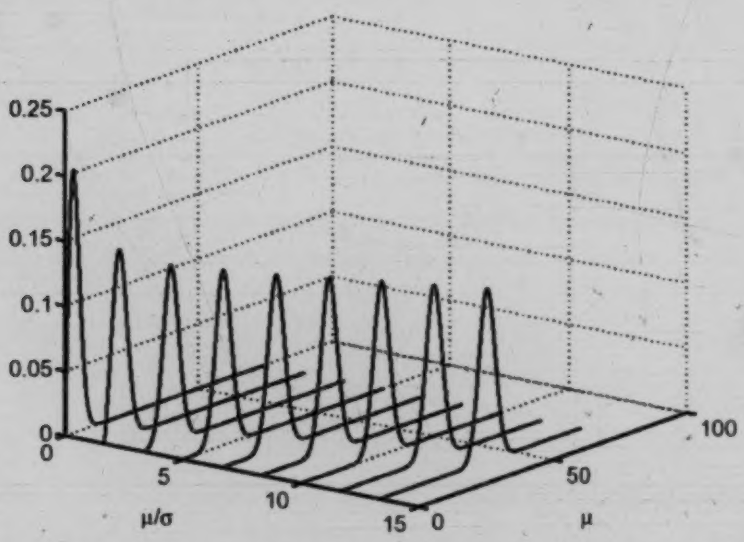

Figure 5.2 The Rice distribution, shown plotted as a function of μ/σ. In the low signal limit the Rice distribution can be approximated by the Rayleigh distribution, while in the high signal limit it is Gaussian distributed.

Concerns regarding SNR in NNLS are well founded, however explicit definitions of SNR is not always offered in quantitative T_2 literature. With respect to curve fitting, two measures of SNR are particularly applicable, and these typically differ from a third SNR typically referred to in other MRI applications. The latter has been coined background signal to noise ratio, SNR_B [94]; Does and Gore define it as the standard deviation of pixels in a background ROI (assumed zero signal) over mean signal intensity from within the sample. This noise is Rician distributed in the low signal limit, and is thus expected to be Rayleigh distributed, with a standard deviation $\sigma_B=(\pi/2)^{-1/2}\mu_B$, where μ_B is the mean signal in the magnitude image. We stray from their definition somewhat, and consider a measure SNR_B to be that of Whittall *et al* [62]; namely, the ratio of extrapolated signal at t=0 to the standard deviation of the (Rayleigh) distributed background noise.

A second measure of noise with respect to curve fitting would be the standard deviation of voxel signal from within a region of interest. Indeed, this measure is of intrinsic importance to our analysis methodology, as it is passed to the NNLS algorithm and used in the determination of the χ^2 misfit statistic. This image standard deviation is expected to be Rician distributed in the 'high' ($\mu/\sigma>2$) signal limit, and is therefore Gaussian. Does and Gore [94] refer to the measure of SNR formed by dividing mean signal intensity by this noise measure as SNR_I, (image SNR); we modify the definition here, and define SNR_I as the mean signal at each echo divided by the standard deviation of pixel intensity at the same echo. This forms a relatively constant ratio during the timecourse of the multi-echo experiment, although we note that defining noise in such a manner introduces an effect from of tissue heterogeneity to the SNR measurement that is not representative of systemic 'noise'.

We have previously alluded to yet another measure of SNR, which is particularly relevant in relaxation measurements. We define SNR_{fit}, as the standard deviation of the fit residuals divided by the extrapolated signal at t=0; it is therefore normalized between scans with different echo spacings. This standard deviation has the most direct connotation in simulation studies, where SNR_{fit} ratios can be approximated through the addition of zero mean Gaussian noise to a simulated decay curve. As we shall see however, it is also very sensitive to particularities of the noise structure.

5.1.1 SNR of *in vivo* quantitative T_2

Measurements of signal to noise typical of *in vivo* head, *in vivo* spine, and *in vitro* spine are reported below in table 5.1. Values for *in vivo* and *in vitro* spine are averages from all ROIs used in this spine study, values reported for *in vivo* brain were determined from an axial head slice of a single subject. In that study, ROIs were drawn on 6 WM structures and in background areas, and co-registered between the conventional and IR CPMG data set.

Table 5.1 SNR measures in MR based Quantitative T_2

	Coil	Signal	Residuals	N_B SNR_B	SNR_I	SNR_{fit}
Brain *in vivo* (CPMG)	Birdcage	1183±54	0.66±0.4	2.37 499.15	11.87±3.02	2222±919
Brain *in vivo* (IR-CPMG)	Birdcage	848±29	0.40±0.09	2.37 357.80	12.26±1.98	2201±553
Spine *in vivo* (IR-CPMG)	Phased Array	422±56	1.03±0.4	4.17 101.19	8.59±1.83	556±229
Spine *in vitro* (CPMG)	Birdcage	1986±64	2.28±0.5	1.62 1226	15.24±2.89	905±184

Table 5.1 Different SNR measures used to evaluate multiecho T_2 data. "Signal" was defined as the extrapolated noise at t=0; "Residuals" was the mean of the absolute difference between the NNLS fit and the experimental data; N_B and SNR_B were the standard deviations of noise in background regions and the ratio between "Signal" and N_B; SNR_I was the ratio between mean signal at an echo by the standard deviation of voxel signals in the ROI; SNR_{fit} is the average between "Signal" and "Residuals" over all the ROIs used.

There are a few features of these noise measurements worthy of further discussion. Firstly, large fluctuations in the SNR_{fit} measure were observed. This could be an artifact of the noise structures to which NNLS is amenable as a fitting algorithm: positivity constraints may play a role in that not all noise can be fitted to the same extent. It could be that our data is simply too noisy for this idyllic measure of SNR to enjoy widespread applicability.

Expectations of Rayleigh noise in background regions were found to be largely unobserved, regardless of the coil used. Ratios of μ_B to σ_B were relatively consistent between studies (average ±SD 4.21±0.46); this puts the determinations of noise in background ROIs in the Gaussian limit of the Rice distribution. This prompted our use of the average value of the background *residuals* (from the fit to background 'signal') as our measure for N_B. That this arises purely from ghosting and artefact suggests that background ROIs do not offer an untainted estimate of systemic noise. It does have value, however, in that it can be used as an indicator of the effects that surrounding physiology and their subsequent ghosting into tissues of interest could have on quantitative measurements on the tissue. In this respect, it points to a formidable obstacle facing *in vivo* quantitative T_2 in the spinal cord, where the value for N_B suggests that substantial flow artefact may complicate a multi-echo measurement.

Indeed, by all measures in table 5.1, IR-CPMG imparts significant costs in signal to noise. The preceeding analysis suggests that this a feature of not only the signal loss due to the IR pulse and signal falloff, but also of increased noise due to ghosting. These observations prompted the simulations explored in the next section.

5.1.2 SNR: Simulation and Reality

Our concerns with signal to noise prompted a simulation study, in which measures employed by Fenrich *et al.* were implemented in order to characterize the ability of a 32 echo sequence to resolve features of the T_2 distribution. The *S* and *R* statistics were defined as per equations (5.1) and (5.2) respectively; non-separated / non-resolved distributions were assigned *R,S* values of zero. A simple simulation program was designed to simulate multi-echo data, sampled 32 times at 10ms intervals. Exponential inputs consisted of delta function constituents at user defined amplitudes and T_2 times. Different SNR ratios were then characterized through the addition of a single resolution of Gaussian noise; the SNR of the simulated data set was defined as the extrapolated signal at t=0, divided by the standard deviation of the added noise. We considered a simple model of nervous system tissue, with T_2 peaks at 20ms (20%), and 80ms (80%), and use the mentioned definitions of *R, S,* and MWF to quantify solution characteristics. To generate adequate statistics, one thousand simulations were preformed at SNR's of 1000, 500, 300, 100, and 50; exponential decays were inverted with the same NNLS procedure used for *in vitro* and *in vivo* analysis.

The distribution of measured MWF exhibits a marked dependence on SNR, which is illustrated in figure 5.3. As SNR decreases, the standard deviation of measured MWF values increases significantly, but perhaps more concerning is the noted reduction of mean MWF at lower SNR. Mean, median, and standard deviations of resolved MWF are shown below in table 5.2.

Table 5.2 Mean, median, and standard deviations of simulated MWF distributions

	1000 SNR	500 SNR	300 SNR	100 SNR	50 SNR
Mean MWF	0.191	0.182	0.175	0.162	0.161
Median MWF	0.192	0.183	0.176	0.163	0.164
SD	0.009	0.015	0.020	0.040	0.071

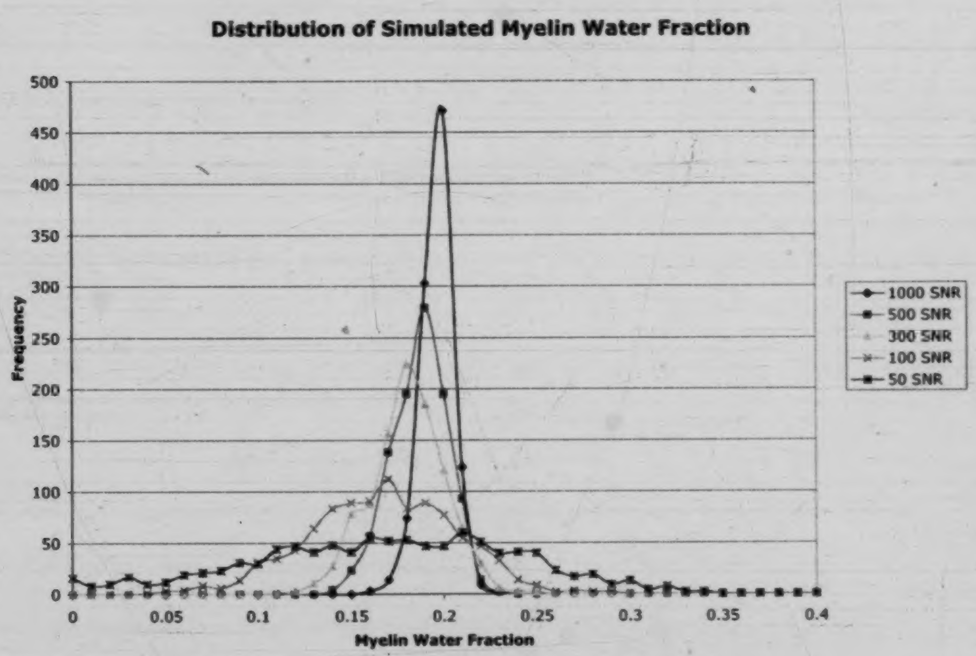

Figure 5.3 Distribution of myelin water fraction (0-40ms) in simulated decay curves at different SNR.

While all mean myelin water fraction are within one standard deviation of the true value of 0.20, there is a noted progression towards lower MWF at reduced SNR. This was not previously seen by Jones [71] in similar simulation studies, where noise was added in quadrature, and the myelin water fraction was defined between 10 - 50ms. It was thought that this lower MWF might have resulted from a failure to resolve a separate myelin water peak. This is not borne out in regression analyses between MWF and the *R* and *S* statistics at lower SNR, however. Even at the lowest SNR of 50, myelin water fractions for unresolved spectra (*R*,*S*=0) were not significantly different from those in spectra with non-zero values of the *R* and *S* statistic. It is noteworthy that this progression towards lower MWF at lower SNR may not be a general trend; similar simulations using inputs corresponding to the delta function components resolved in non-regularized fits to the bovine spine NMR CPMG resolved *increasing* MWF as SNR decreased.

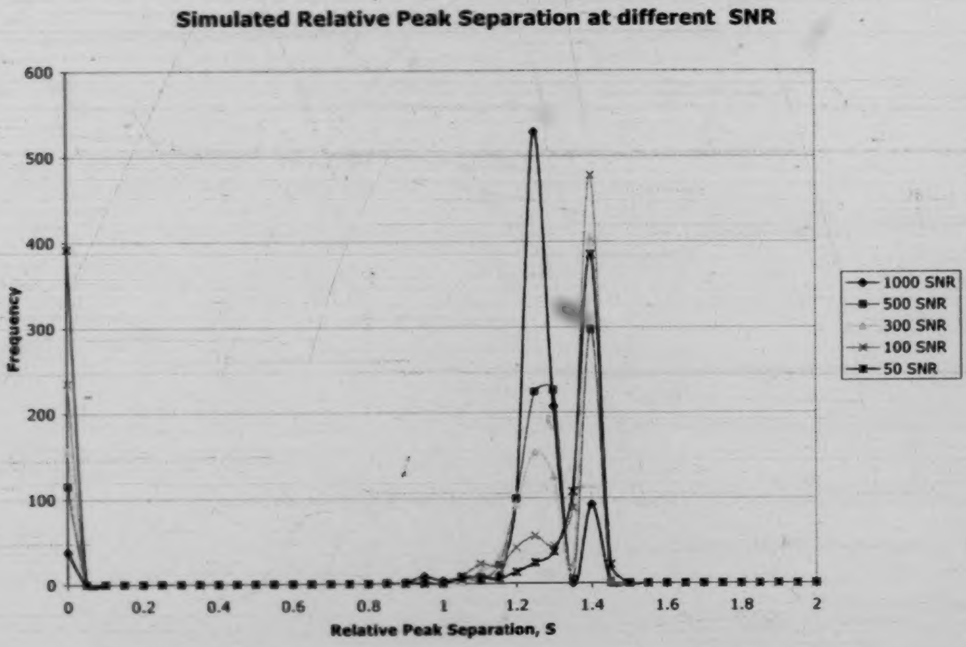

Figure 5.4 Distributions of Relative peak separation, *S*, at different SNR levels. There is a tendency towards greater peak separation at lower SNR.

The Relative Peak Separation, *S*, also shows a marked departure from the true value of 1.2 as SNR decreases. This is likely an effect stemming from an asymmetry in NNLS sensitivity to different noise structures: noise that subtracts from early echoes serves to decrease the value of the shortest T_2, which is often seen pressed against the minimum 15ms partition on the T_2 axis at clinical SNR. These early echoes then, dictate a 'second best fit' of a slightly smaller short T_2, and an accordingly slightly larger intermediate T_2. In this simulation, it appears as though this second best fit occurs with a 15ms short T_2, and an intermediate T_2 of 85ms, giving the observed tendency towards a Relative Separation of 1.4 at lower SNR.

Finally, the peak resolution, *R*, was also computed for the simulated exponential decays, yielding the distributions in peak resolution. An example of this distribution from the 50 SNR case is shown below in figures 5.5, while a cumulative percentage measure is shown in figure 5.6 for all distributions.

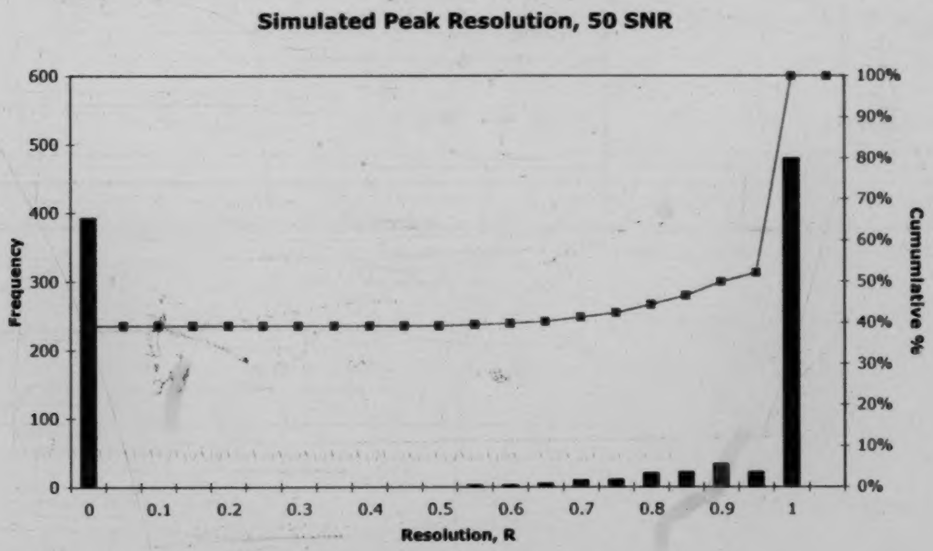

Figure 5.5 Example of the distribution in *R* measured at low SNR. The plotted line shows the cumulative percentage of T_2 distributions at the listed R values, and can be used as a measure of the proportion of spectra in which a separate myelin water T_2 component is being resolved.

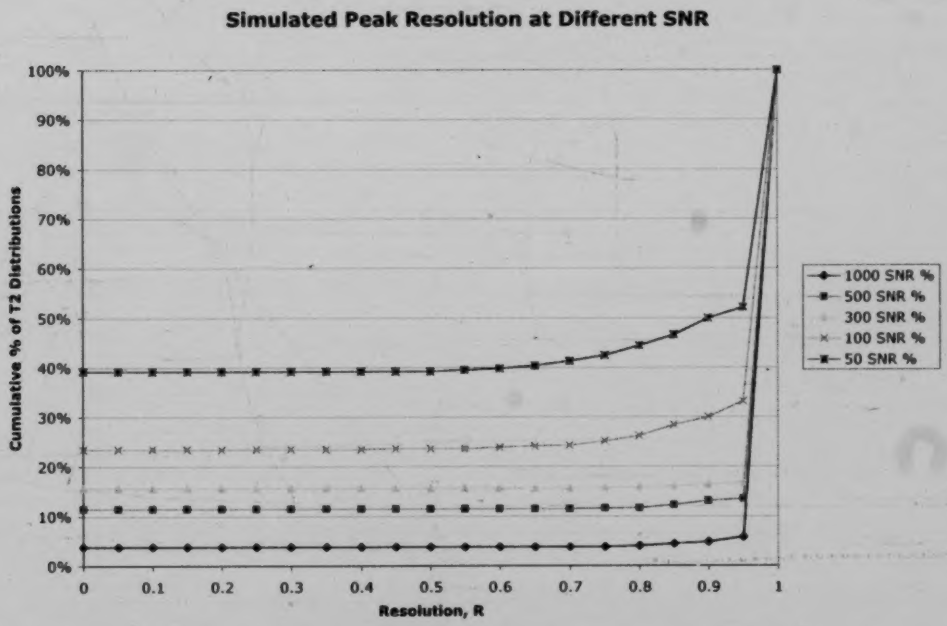

Figure 5.6 Cumulative percentage of *R* values in resolved T_2 distributions from simulated decays.

A sharp transition in *R* between unity and zero was observed in these simulations, the abruptness of which decreases at lower SNR, allowing for more 'intermediate' ($0<R<1$) peak resolutions. This result is in qualitative agreement with simulations preformed by Fenrich *et al* [70], where a logarithmic sampling consisting of >10points per decade was employed (in contrast to the 32 evenly spaced echoes here).

These simulations reveal that SNR concerns in T_2 relaxation studies are well founded, as they can substantially alter measured distribution characteristics. Indeed, their computation may even help to resolve our difficulties in defining the SNR of measured distributions *in vivo*. Given a reasonable expectation of multi-component T_2 in white matter, the *R* statistic in particular could be useful in estimating the signal to noise of our measurements.

Accordingly, the *R* and *S* statistics were computed for the T_2 distributions from all the ROIs used in the human *in vivo* study. These are shown below in figure 5.7 and 5.8 respectively.

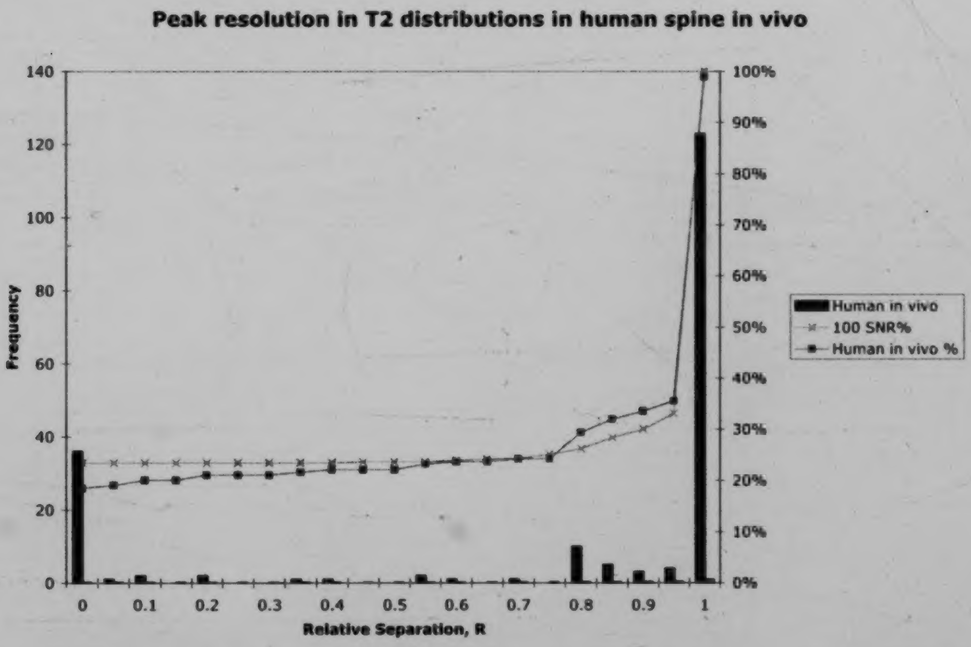

Figure 5.7 Distribution of Peak Resolution, R in T_2 spectra in human spine *in vivo*. Shown for comparison is the data (cumulative % in R values) from the simulation study at 100 SNR, which agrees qualitatively with the measured distribution.

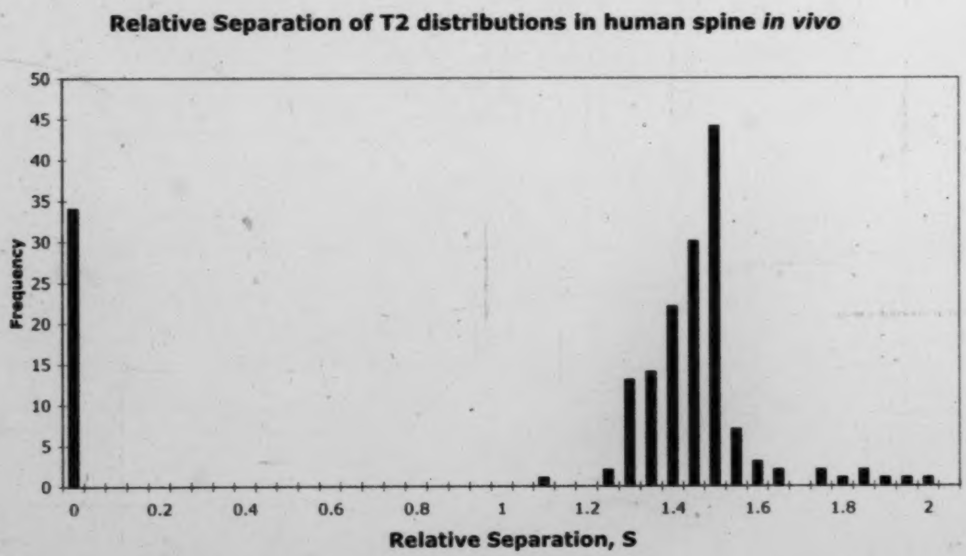

Figure 5.8 Relative Separation, S, of resolved T_2 distributions in human spine *in vivo*. A greater spread in S values is seen about a mean of 1.44 than observed in simulation studies.

A telling comparison is given in figure 5.7, where the cumulative percentage in the distribution of the *R* statistic marks a qualitative agreement with results from the simulation preformed at 100 SNR. This highlights a potential utility of the *R* and *S* statistics in indexing *in vivo* data — where SNR can be difficult to measure — to simulation studies, where the SNR is well defined. For example, in 18.9% of the T_2 distributions in human spine *in vivo*, only a single component was resolved; a measure that interpolates to simulated zero mean Gaussian SNRs of between 100 (24% single component) and 300 (16% single component), if we maintain a stringent expectation of multi-component white matter in all ROIs in the spine *in vivo*.

Results for the *in vivo* calculation of the *S* statistic (figure 5.8), meanwhile, show a greater spread about a mean value of S=1.44 (calculated for all cases with nonzero separation), than simulated counterparts. This is likely due to a distribution of T_2 times for the second compartment *in vivo*, which is not adequately represented by the delta function inputs used in simulation work.

Simulations did accurately predict independence between MWF and *R* (R^2=0.004) and of MWF and *S* (R^2=0.003) observed *in vivo*, with MWF in non separated (*R*,*S*=0; mean±SD 0.22±0.08) cases showing little change when compared to cases where separate components were resolved ($R,S \neq 0$; 0.23±0.08) respectively. The distribution of MWF values is shown below in figure 5.9.

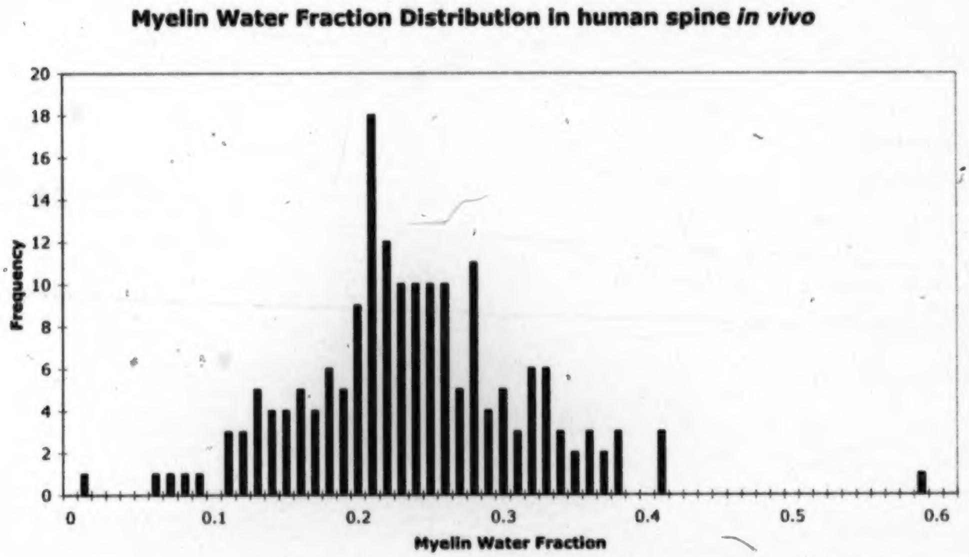

Figure 5.9 Distribution of myelin water fractions in human spine *in vivo*. Mean ± SD was 0.22 ± 0.06.

We note here that physiological variation in myelin content in the spinal cord reported in chapter 4 will contribute substantially to distribution characteristics, especially when differential sampling of spinal cord regions (i.e. greater FOV overlap with thoracic areas) is taken into account. This makes comparisons between myelin water fraction distribution characteristics resolved *in vivo* to those simulated through constant exponential inputs inadvisable. The distribution does reveal in myelin water fraction values far in excess of those reported in other white matter structures [61, 62], which leads us to the next topic in this discussion: accounting for the higher measured MWF in spinal cord relative to those in brain white matter.

5.2 Accounting for higher myelin water fractions in the spinal cord

As mentioned, myelin water fractions measured in the spinal cord were found to be far higher than those measured in brain white matter. A comparison between average MWF values in different brain regions (from [62]) to those resolved in the spinal cord is given in table 5.3.

Table 5.3 Myelin water fractions in brain and spinal cord

Location	Myelin Water Fraction
Corpus callosum, genu	9.86 (0.96)
Corpus callosum, splenium	13.05 (0.96)
Minor Forceps	8.40 (0.89)
Major Forceps	10.11 (0.51)
Internal Capsules	15.00 (0.95)
Average, brain white matter	**11.28**
Cervical spine	21.75 (2.13)
Thoracic spine	24.28 (3.57)
Lumbar spine	11.44 (6.42)
Average: human SC *in vivo*	**21.87 (5.78)**
Average: human SC WM[a] *in vivo*	**25.12 (5.63)**
Average: bovine SC WM *in vitro*	**30.00 (2.67)**
Bovine NMR *in vitro* (cord 1)	**34.00 (1.6)**

Table 5.3 Myelin water fractions in brain [62], and spinal cord (this study). [a]human SC WM values were calculated from SC values, corrected for expected grey matter content.

We consider two general classes of mechanisms that would raise measured myelin water fractions in the spinal cord. Non-biological mechanisms assess the influences of our sampling protocol on measured fractional contributions of the short T_2 to total signal, in particular, the effects of the IR CPMG sequence. But while such mechanisms could be applied towards accounting for higher MWF *in vivo*, they can not explain the values measured in bovine spinal cord *in vitro*. Hence a second class of mechanisms, pertaining to regional differences in myelin biology, entertain the possibility that the elevated values in both human and bovine models may have biological and chemical precedents given known differences in spinal myelin composition.

5.2.1 Non-biological factors

T_1 effects

We touched upon the T_1 effects of the IR-CPMG sequence briefly in chapter 4, where they were discussed in the context of reducing the SNR of our measurements in spinal cord tissue *in vivo*; an effect that depended on the grey matter content of the region of interest. A consequence of that effect is that the fractional contribution of white matter to total signal in IR-CPMG is *greater* than it would be in a CPMG measurement of the same tissue. This difference arises solely due to the differences in T_1 between WM and GM, and should serve to accordingly *increase* the measured myelin water fraction in an IR-CPMG measurement, relative to the CPMG predecessor.

Using the T_1 values listed in table 4.1, we can estimate this amplification effect at the TI used in the human trial. The effect is expected to vary with the relative white matter content of the voxel, with obvious endpoints at zero GM content (at which point WM in both IR-CPMG and CPMG will be contributing 100% of total signal), and 100% GM content (where WM in both cases will contribute 0% to total signal). In between these two endpoints, the relative contribution of white matter in IR-CPMG is greater than it is in CPMG, as can be seen in figure 5.10.

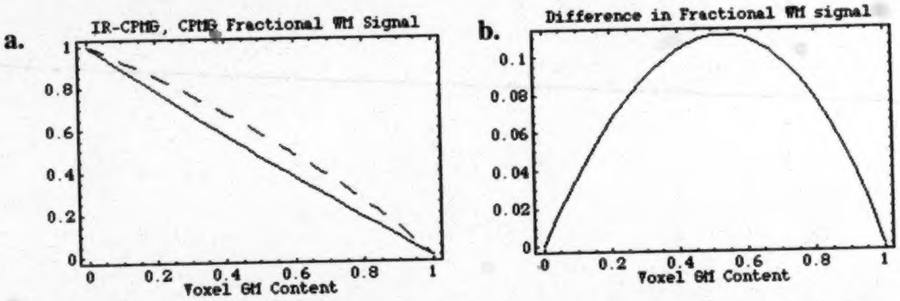

Figure 5.10 (a) Calculated fractional white matter signal in voxels with different GM content. In all voxels between the limiting grey matter compositions, the measured fractional WM signal in IR CPMG (dashed curve) is be greater than in a CPMG experiment (solid curve). The difference between the two experiments (IR-CPMG – CPMG) is plotted in (b).

If we assume that myelin constitutes a constant fraction of the WM signal along the spinal cord (i.e. a uniform WM composition), this effect translates to a corresponding over-estimate of the myelin water fraction in IR-CPMG. Making a correction, however, puts us in the unfortunate position of correcting our measurement of myelin water fraction to relative WM content; the very parameter to which we expect sensitivity. Measured WM areal fractions on myelin stained transverse spinal cord sections ranged from 0.88 (lower pyramidal decussation) to 0.50 (at the Sacral 5 level), translating to a physiologically relevant GM range of 0.12 to 0.50. From the plots above, we can therefore reason that we have likely overestimated the myelin water fraction (relative to a CPMG measurement) by an amount that ranges from 4.3% to 11%. Adjusted myelin water fraction values for the statistically significant 'bins' defined in chapter 4 are shown in figure 5.11.

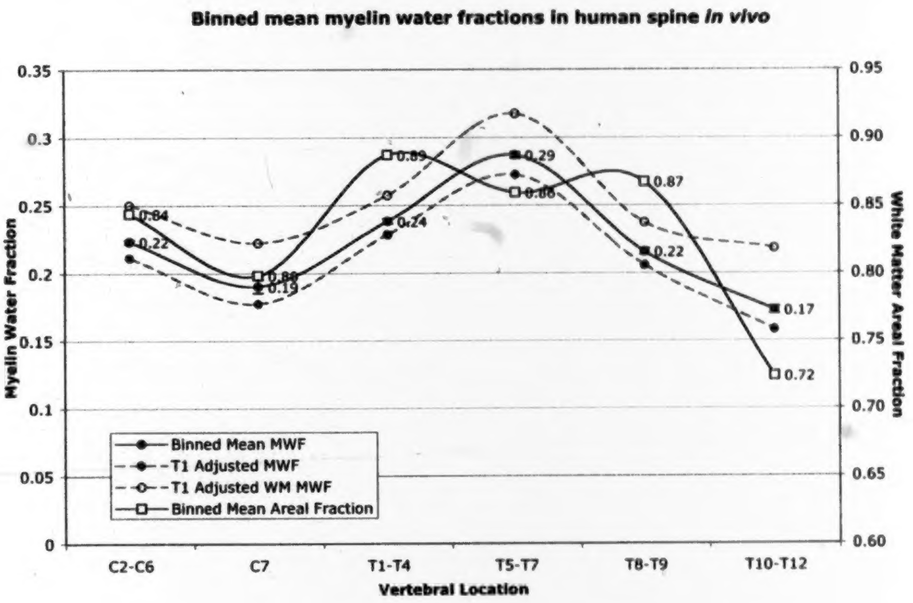

Figure 5.11 Binned myelin water fraction measurements adjusted for T_1 effects. Percent overestimate varies with the areal white matter fraction, which is also plotted. T_1 adjusted white matter values assumed a GM MWF of zero.

Figure 5.11 illustrates the upward bias in myelin water fraction measurement resulting from the T_1 weighting against the grey matter signal. The "T_1 adjusted MWF", plotted above, corresponds (in theory) to the myelin water fraction measurement that would be made with a conventional 32 echo Poon Henkelman CPMG acquisition.

This upward bias of the IR-CPMG sequence was confirmed *in vivo* on an axial head slice, acquired using both conventional CPMG and IR-CPMG sequences. Six regions of interest were drawn in white matter areas, these were co-registered between the two different data sets. Average MWF (± SD) for the CPMG acquisition was found to be 6.6±1.4%, while the same ROIs resolved myelin water fractions of 7.9±2.5% in the IR-CPMG case (an increase of 19±2.1%). A single tailed paired t-test over all six regions of interest indicated significance at $P \leq 0.1$.

It is noteworthy that this effect has likely *reduced* the correlation reported between MWF and white matter areal fraction reported in chapter 4, compared to one that would be measured with a CPMG experiment. Over the physiologically relevant range in GM content, all voxels experience a compensatory T1 effect that overestimates the myelin water fraction that would be measured in a CPMG experiment, by an amount that increases with increasing grey matter content as per figure 5.10.

Interestingly, a corollary to this effect is that in becoming less sensitive to the myelin water *fraction*, we become more selective for the myelin water *signal*, through the T_1 weighting against contributions from other tissues at longer spin-lattice relaxation times. This effect has been exploited in the interest of detecting multi-component T_1 in peripheral nerve *in vitro* [66], and trigeminal nerve *in vivo* [95]. These successes in detecting multi-component T_1 in model nerve systems carry implications for our IR-CPMG experiment: if spin lattice relaxation in spinal cord white matter is multi-exponential *in vivo*, then our sensitivity to myelinic water signal in an IR-CPMG experiment would be increased through a T_1 weighting against the intra and extra axonal components in myelinated white matter. This would lead to an even greater over estimate of measured myelin water fractions in IR-CPMG. Despite the mentioned successes in peripheral nerve systems however, attempts to measure multi-component T_1 through similar integrated T_1-T_2 SR-CPMG (saturation recovery CPMG) in rat brain white matter structures *in vivo* have resolved primarily mono-exponential T_1 [95]; it remains to be seen whether spinal cord tissue is more analogous to peripheral or central nervous system nerve in this respect.

CSF Partial Volume Effect

Motivations behind implementation of the myelin map filter discriminating against proton density (as determined by extrapolated signal at t=0) stemmed from observed effects of the IR preparation pulse on CSF, and the subsequent fit of some CSF voxels to a short T_2. To further investigate the effects of CSF partial voluming we preformed a simple simulation *in situ*.

Non-contiguous ROIs were defined using voxels from SC ROIs used in the regional MWF measurements, and voxels from CSF ROIs that were selected based on their having high (>0.30) or low (<0.05) short T_2 amplitudes. Characteristics of CSF ROIs used are shown in table 5.4, the effect on measured myelin water fractions in combined (i.e. partial volumed) CSF-SC ROIs is shown in figure 5.12.

Table 5.4 Characteristics of CSF ROIs used in a partial voluming simulation

	Short T_2 Fraction	10ms echo signal	No. of pixels in CSF ROI	Average Vol. Ratio (CSF/SC)
CSF 1	0.32	64.1	57	0.31
CSF 2	0.55	42.3	19	0.13
CSF 3	0.03	30.6	100	0.44
CSF 4	0.00	40.6	64	0.33

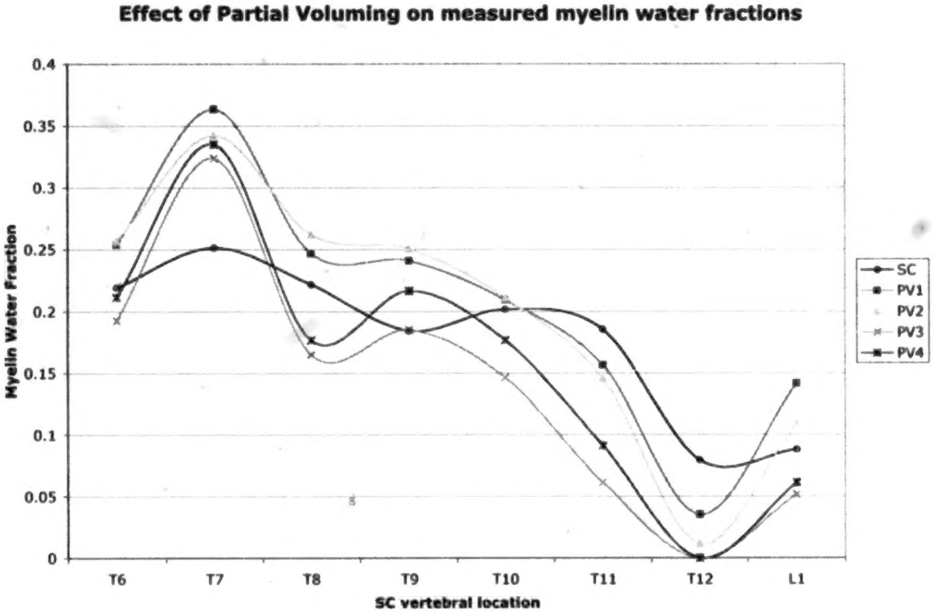

Figure 5.12 Myelin water fractions resolved in partial volumed CSF and SC ROIs. PV1 corresponds to a non-contiguous ROI comprising signal from CSF1, and of the SC at the indicated physiological level.

NNLS inversion of the combined CSF-SC signal revealed surprisingly consistent effects on the measured myelin water fraction, considering the diverse nature of the CSF ROIs used. CSF ROIs with a large 'short T_2' component (i.e. PV1, PV2) did, on average, act to raise the measured myelin water fraction, especially relative to the PV cases corresponding to CSF ROIs with negligible short T_2 fractions (i.e. PV3, PV4). A paired single tail Student's t-test between those two groups reveals significance at $P<5E-5$. However, similar tests between individual PV cases and native SC ROIs revealed only two differences (PV1 and PV3, corresponding to CSF1 and CSF3) that were significant at the $P < 0.10$ level. Average absolute percent change in MWF was surprisingly constant over the different trials (average of 25.4%; range 29.0% to 22.6%), and percent change was found not to correlate with percent CSF content in the ROI volume. Interestingly, the size of the short T_2 component in the CSF ROI did not uniformly bias PV results upwards (expected in the large 'short T_2' component case) or downwards (expected in the small 'short T_2' case), with all PV cases displaying an apparent amplification of the local SC MWF maxima and minima.

This preliminary study requires more supporting work to investigate partial voluming responses in more samples, conjoined with a greater variety of CSF signal. However, the demonstration that CSF partial voluming has the ability to significantly alter measured MWF has dangerous implications for myelin water fraction measurements in an IR-CPMG context.

5.2.2 Biological factors

While T_1 and CSF partial voluming effects could account for some increases in measured IR-CPMG MWF in humans *in vivo*, such mechanisms are not amenable to explaining conventional CPMG *in vitro* measurements. Moreover, there is now considerable inter-study agreement suggesting higher myelin water fractions in the spinal cord in humans [28-30]; in addition the values found here for bovine spinal cord white matter agree with previously measured values in bovine optic nerve [74]. Hence we are left to reason with the possibility that these measurements are indicative of a regional difference in CNS white matter composition, on a scale far greater than interregional variations in the brain. In this section, we avail ourselves of three general areas in which there exists a precedent in the literature to make the claim that the measured myelin water fraction values might accurately reflect regional differences between brain and spine myelination: myelin yields in dissociation experiments, differences in axonal density and fiber morphometry, and regional differences in myelin chemistry.

Myelin content as determined by dissociation

Studies on myelin composition have historically been accomplished through isolation of myelin from homogenized CNS tissue. Use of media of low ionic strength prompts disassociation of the myelin sheath from the axons, and the low density of the myelin sheath allows its isolation through gravimetric centrifugation [96]. In an example of such techniques, Smith and Sedgewick [97] incubated slices of rat nervous system tissue from the cerebrum, thalamic area, cerebellum, brain stem, and spinal cord in Krebs-Ringer bicarbonate buffer. The amounts of myelin recovered, shown in table 5.5, were said to "follow the general trend of myelin content in the brain area", although no further reference is offered against which this claim can be compared.

Table 5.5 Myelin yield in different CNS regions [97]

CNS region	**Total myelin yield (mg dry weight / 100mg slice)**
Cerebrum	5
Thalamus	5.3
Cerebellum	4.1
Brain stem	7.9
Spinal cord	12.6

It is noteworthy that Smith and Sedgewick do not go as far as to suggest that the amount of dissociated myelin is proportional to regional myelin content. Instead, the high myelin yield in the spine is attributed in part to regional differences in myelin stability, which they link to regional differences in protein composition. The findings of Zimmerman *et al* [98] were in qualitative agreement with those of Smith and Sedgewick, the former found that myelin yield in the brainstem was 4 times that of cortical regions.

Axonal density and fiber morphometry

The parallel, tightly packed arrangement of white matter tracts in the spinal cord offers a geometrical basis upon which a higher myelin density might be expected in an image voxel. Interestingly however, literature values suggest that axonal density in the spinal cord is far less than that in other highly ordered CNS white matter structures. In a study on MR characteristics of the spine in MS, axonal density was quantified for normal controls by Bergers *et al.* [99]. The average axonal density for the 11 cervical, 4 high thoracic, and 4 low thoracic samples was found to be 26 989 axons / mm^2 (range: 14,111 to 38,100 axons/mm^2). Meanwhile, in samples from the human medulary pyramid (a structure superior to the spinal cord, but one that shares many of the same white matter tracts) von Keyerlingk and Schramm [100] determined an axonal density of 66 000 axons/mm^2. Both of these sums are paltry, however, when compared to corpus collosum values measured by Evangelou *et al.* [101], where values ranged from 120 000 axons/mm^2 in posterior regions, to 140 000 axons/mm^2 in anterior regions.

However, expectations that myelination might correlate with axonal density ignores important morphological features of myelinated axons, such as regional differences in axon size, or more importantly, fiber (axon + myelin) size. Fiber morphometry is often quantified through the calculation of fiber 'g' ratio:

$$g = \frac{d_a}{d_f} = \frac{d_a}{(2\partial + d_a)} \tag{5.4}$$

where d_a the axon diameter and d_f is the fiber diameter; the calculation of this ratio equivalently gives us a measure of the myelin thickness ∂. A simple geometric argument can show that the cross sectional area ratio (myelin area / axon area) is given by $1\text{-}g^2$; a measure that, despite the observations of tighter myelin packing at higher g ratios [102], we can assume will be related to measured myelin water fraction.

Rather than relying on measurement of g ratios, Hilderbrand and Hahn undertook the painstaking process of counting individual lamellae and measuring interlamellar distances in spinal cords of 8 vertebrate species (cat, rabbit, guinea pig, rat, mouse, frog, and perch). From their data, consisting of histograms in axon size, mean number of lamella, and species-specific average inter-lamellar distance, we can calculate g ratios and the corresponding ratio between myelinic and axonal areal fractions. The distributions of these calculated g ratios, and the corresponding calculated areal fractions are shown in figure 5.13.

Calculated g ratios in the spinal cords of several species

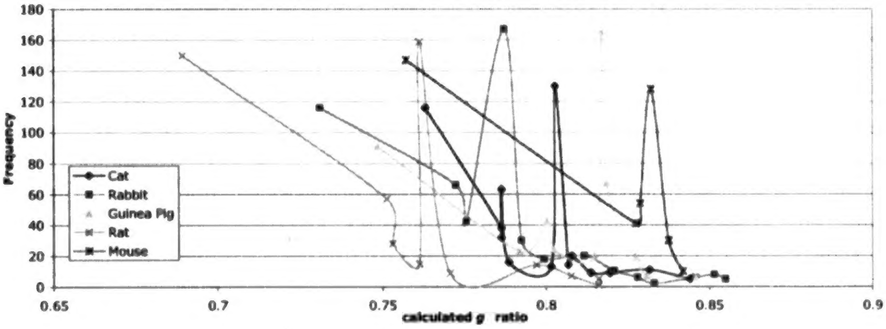

Calculated areal ratio in the spinal cords of several species

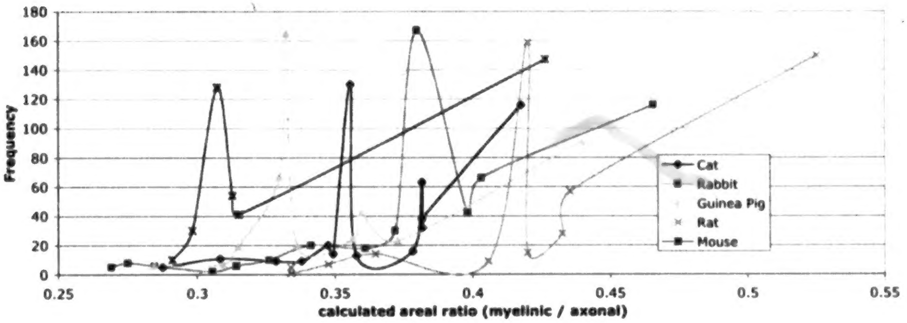

Figure 5.13 Calculated *g* ratios, and corresponding areal fractions from a study on spinal cord fiber morphometry [102]

While no data could be found for similar studies on human spine, morphometry characteristics of the human medullary pyramid, which shares many efferent and afferent white matter pathways with the spinal cord, were characterized by von Keyserlingk [100]. Interestingly, their data suggests that humans may have *g* ratios a factor of 1/2 smaller than those found in other vertebrates. The calculated areal ratios are shown below in figure 5.14, plotted beside those found in the spinal cords in the Hilderbrand study.

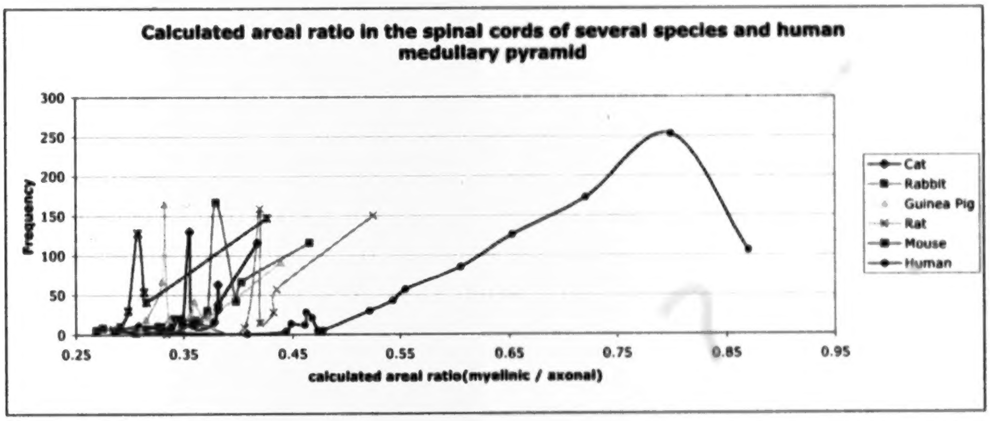

Figure 5.14 Calculated areal ratios in human medullary pyramid relative to those calculated in the spinal cord of lower vertebrates. Spinal cord data from [102], medullary pyramid data from [100].

The difference in area ratios between human medullary pyramid (weighted average 0.70) and the spinal cords of other vertebrates (weighted averages ranging from 0.36 to 0.45) could be indicative of greater myelination in humans, and may partially explain why measured myelin water fractions in human spinal cord were greater than those in Hartley guinea pigs [51]. The only studies found in which numeric values were given for any of the brain white matter areas in table 5.3 was one of mouse corpus callosum [103], where average *g* ratios in control specimens was 0.83 (area ratio 0.31), a value slightly smaller than that from in mouse spinal cord (0.80 , 0.35). Given the apparent discrepancies in human *g* ratio measurements, this trend may or may not translate to human morphometry.

Corpus callosum morphometry differs from that of the spinal cord in one other respect that could have important implications in CPMG measurement: the distribution of axonal size, with the latter showing a shift towards larger axons [104, 105]. Histograms from a study by Amaducci *et al.* are reproduced in figure 5.15.

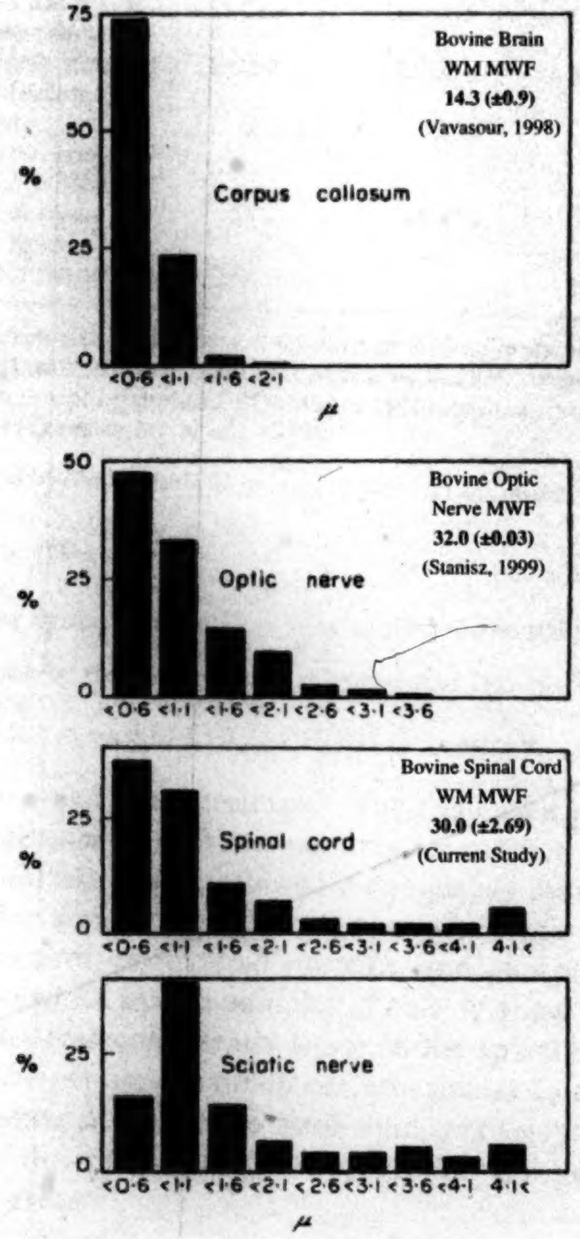

Figure 515 Fiber diameter distribution in different white matter areas of the bovine nervous system, adapted from [105]. Diameter μ is in microns. Myelin water fractions from studies that have examined that are are shown inset where applicable.

It may be possible that the short T_2 component demonstrates greater sensitivity to thicker myelin sheaths; i.e. to large axons with a large number of myelinic lamellae, given the greater expected residency time of myelinic water molecules in such arrangements compared to smaller fibers at similar g ratios. A simple model can illustrate.

The sensitivity of the measured short T_2 component on intercompartmental exchange can be assessed with a simple simulation using a two pool model of white matter. Consider two spin groups of sizes P_1 and P_2, with respective compartmental T_2 times of T_{2a} and T_{2b} respectively. The two spin groups form a closed system; the magnetization lost through exchange by P_1 is gained by P_2 and vice versa. The extent of this exchange can be quantified through a cross-relaxation constant,

$$\frac{1}{T_{cr}} = P_1 k_{12} = P_2 k_{21} \tag{5.5}$$

where k_{12} and k_{21} are the exchange rate constants between the appropriate pools. While this model amounts to a gross oversimplification with respect to the mechanisms, exchange dynamics, and geometrical dependencies involved in T_2, it does serve a didactic purpose in that it appropriately conceptualizes CPMG data as a spatial sum and a time average in spin environments, and it qualitatively describes the effect of exchange with respect to real vs. measured T_2 times, component areal fractions, and component widths. CPMG data was simulated by iteratively evolving the system at discrete timesteps of 0.1ms, to illustrate the effect of increased exchange. Simulated data was then sampled at 32 10ms timesteps at an SNR of 300, and inverted with the same NNLS algorithm used in analysis of MRI data in this study. Results from inversions using T_{2a}=20ms, T_{2b}=80ms, P_1=200, P_2=800 at two different T_{cr} are shown in figure 5.16.

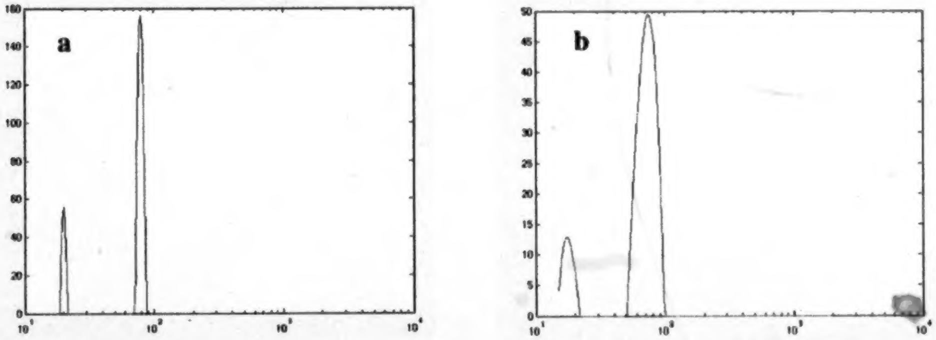

Figure 5.16 CPMG data simulated using a simple 2 pool model. (a) with a T_{cr} of 10 000; measured distribution characteristics are close to expectations (MWF=19.71). (b) When T_{cr} is reduced by a factor of ten, T_2 peaks broaden and shift to the left, and the short T_2 peak decreases in relative magnitude (MWF=14.03).

These simple simulations qualitatively describe effects that have been previously noted using more complicated models of white matter (Bjarnason, personal communication),[74, 82]: a shift towards shorter T_2 times and reduced contribution of the short T_2 component with increased exchange. They illustrate a theoretical basis upon which one might expect that multiple relaxation components in nerve tissue might exhibit a sensitivity not only to myelin content, but to distributions in axonal morphology.

We can elaborate by considering a simple calculation of compartment mixing times. Such a calculation was carried out by Koenig *et al*, who estimated the mixing times between axonal and myelinic components. Given an estimated lower bound membrane permeability of 10^{-4} cm s^{-1} (from sphingomyelin:cholesterol bilayers at 14.5°C [106]) and considering a fiber consisting of 10 lamellae, he calculated a mixing time of 64ms for the axonal and myelinic components [109]. Given that (1) a substantial portion of fibers in a structure contain 10 lamellae or less, (in the spinal cords of various lower vertebrates, such fibers accounted for 20-36% of all fibers examined [102]), and that (2) such a short mixing time would conceivably kill the myelin water signal, it may be possible that some of the myelin water signal derives in part from a temporal averaging of protons that moved from one myelinic compartment to another during the time course of the measurement. Such promiscuity would certainly be conceivable in a tightly packed structure, where proton exchange between myelin sheaths of adjacent fibers would be possible. If this were the case, one would expect that other factors, such as the tortuosity of the intervening extracellular space, might inadvertently affect the myelin water measurement. Moreover, diffusion out of the myelin compartment in smaller fibers would lead to lower measurements of myelin water fraction from nerves at this lower end of the size spectrum, as per the results suggested by the simple two pool model under conditions of increased exchange. Said another way, the 'true' myelin water fraction would be resolved after a cross relaxation correction; in larger fibers, this correction would be minimal, while in smaller fibers, it could be substantial.

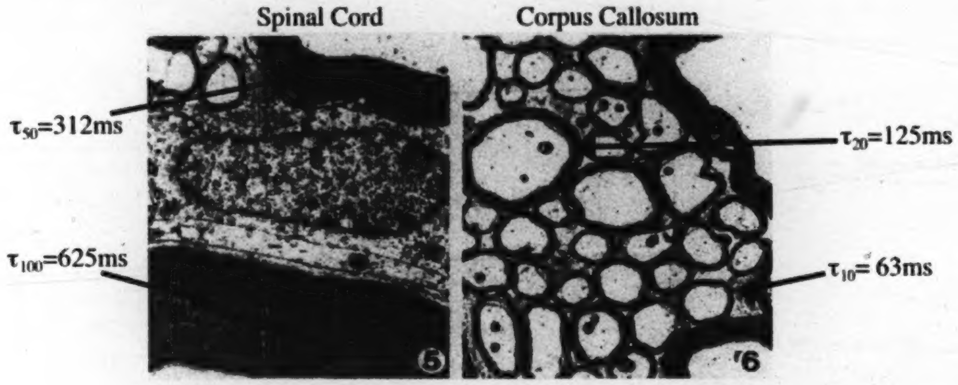

Figure 5.17 Micrographs from feline spinal cord (left) and corpus callosum tissue (right) (adapted from [104]) taken at the same magnification, showing the difference in fiber size distributions between the two white matter structures. Values τ_n indicate expected myelinic residency times in a fiber with n lamellae, as per Koenig's white matter model [109].

Figure 5.17 exemplifies the impact that morphological variation in white matter areas would have on myelinic residency times, thereby illustrating the theoretical basis upon which one might expect that measured myelin water fractions would display a sensitivity to distributions in fiber sizes. If so, indications of a shift towards larger sizes in the spinal cord [104, 105], and in humans in particular [100], could partially account for larger myelin water fractions measured in human spinal cord white matter, even if the true myelin content in those areas is similar.

The suggestion that component amplitude in transverse relaxation distributions could be affected by cellular and supra cellular levels of organization has other solid experimental foundations. In preparations of Red Blood Cell ghosts in aqueous protein solutions, multiexponential transverse decay is only observed when ghosts are confined to regions with dimensions larger than the path length of a water molecule in the inter-echo timescale [50, 107]. A nervous tissue correlate would impose packing and intervening tortuosity restrictions on nerves at the lower end of the size spectrum (where exchange times would require the encounter of multiple myelinic compartments for the resolution of a short T_2 component) while nerves at the higher end of the size spectrum might maintain large enough myelinic residency times to make these supra-cellular effects less important. This is forwarded as a possible reason for some of the variations in myelin water fraction observed in different brain white matter areas, which contain a larger proportion of smaller fibers, and hence might be expected to be more sensitive to this supra-cellular organization. Recently elucidated MWF vs. axonal density relationships (as determined by Bielschovsky staining) in brain white matter areas (Laule and MacKay, unpublished observations) could serve to validate such a hypothesis; with a sharper dependence of MWF on axonal density (i.e. steeper MWF vs. axonal density slope) expected in white matter regions with the lowest fiber sizes. The effect also likely contributes to the higher myelin water fractions measured in spine and optic nerve relative to brain white matter.

Myelin Composition

We can look beyond myelin oganization at the cellular and supra cellular level to its organization at a chemical level in our consideration of regional differences in myelination. While the detection of regional differences in myelin chemistry may seem beyond an imaging modality with special resolutions on the order of a millimeter, the impact of membrane chemistry on the magnetic resonance properties of tissue is significant. Indeed, the chemical attributes of the myelin sheath are recognized as the source of the magnetic resonance properties of white matter relative to grey matter [108-110].

MR relaxation in tissue is complex, and is affected by tissue water content and particularities pertaining to the interaction between water and neighboring tissue macromolecular moieties. Put briefly, relaxation requires a coupling of nuclear spins to local magnetic 'noise' — the fluctuating dipolar fields of neighboring spins. Motion restriction increases the probability of spin-spin exchange, and sites that promote extending binding times – surface hydroxyl, amine and carboxyl groups, for example — are sites which effect dipolar magnetization transfer between water and macromolecular protons [111]. In our consideration of the potential effect of regional differences in myelin chemistry, we examine the two main constituents of myelin: proteins and lipid.

Myelin Protein

The relative ease of purification, and significance in other fields of biology led to an early characterization of the myelin proteins, and revealed the now well established differences between central and peripheral nervous system myelin [112]. Myelin within the CNS is often assumed to be homogeneous, however there exists considerable evidence in the literature that, with respect to protein composition, this is not the case. [113-116]. In particular, studies that have compared cerebral and spinal cord myelin have discovered a increase in the MBP:PLP (myelin basic protein : proteolipid protein) ratio in the spinal cord [113-116]; this difference is especially marked in bovine myelin, as shown in table 5.6.

Table 5.6 Protein content in myelin in brain and spinal cord. (From [116])

Sample	% total protein		
	MBP	Intermediate	PLP
Bovine Brain	34	5	26
Bovine Cord	47	5	21
G.Pig brain	33	3	24
G.Pig Cord	34	3	26
Human Brain	33	4	25
Human Cord	36	4	26

The magnetic resonance implications of the increase in the MBP:PLP ratio are tenuous at best, but we can make some predictions based on the structures of the proteins involved. PLP is one of the most hydrophobic integral membrane proteins, consisting of four membrane spanning domains [117]. The remaining 40% of the residues are hydrophilic [96], but a large number of these consist of hydroxyl residues that are esterfied to lipids, which are present in the PLP complex at a 3 lipid : 1 protein weight ratio. These lipid groups associate via hydrophobic interaction to those form other PLP complexes on the opposing face of the myelin bilayer, contributing to membrane adherence [96]. In contrast, MBP is an 18.5 kDa protein with 12 lysyl and 19 arginyl residues, creating a highly basic protein with a pI of approximately 10.6 [118]. It's highly hydrophilic character leads to a native form that is unfolded in solution, essentially assuming no tertiary structure [96].

In proteins, magnetic coupling occurs through both whole water molecule exchange between hydrophillic binding sites, and proton exchange with protein functions such as amines, amides, and alcohols, although the process is dominated by the former water molecule exchange events [119]. Given that MBP (1) is more hydrophilic, and (2) would offer unhindered access to those hydrophilic residues through its loosely defined tertiary structure; it seems reasonable to assume that an increase in the MBP:PLP ratio would decrease the T_1 of the surrounding water, and likely have a similar effect on T_2. This would favour shorter T_2 times (and higher myelin water fraction) in the spinal cord.

Myelin lipids

The contribution of proteins to the magnetic resonance properties of white matter are underwhelming with respect to the effects of membrane lipids [109, 110, 120]. Koenig *et al.* estimated the water-myelin lipid interaction to be seven fold greater than the analogous protein-water interaction, a value that arises due to the increased interfacial area provided by the multi-lamellar myelin sheath [109]. The effects of individual membrane lipids has also been considered; while the shorter T_1 of myelin water was originally attributed to a higher cholesterol content [108], it has since been shown that galactocerebroside — a lipid present in the myelin sheath at levels almost four times that in grey matter membranes [112] — is likely the greater contributor to the relaxivity and MT of myelinic water [110]. This result stems in part from the contribution of 4 hydroxyl groups to the membrane / water interface by the galactose headgroup relative to the single hydroxyl contributed by cholesterol, and is consistent with the observation that the MT effect increases linearly with the number of hydroxyls per unit area [111].

We suggest here that the effect of cholesterol should not be ignored due to the lesser relative increase (20%) in white vs. grey matter however, as this would ignore asymmetry in myelin lipid composition. While myelin lipid compostion is typically cited as consisting of cholesterol, phospholipids, and galactolipid in ratios from 4:3:2 to 4:4:2 [112], the majority of cholesterol and all of the cerebroside are located in the extracellular membrane face [121]; this would give modest changes in lipid composition, cited in terms concentrations over the entire myelin sheath with respect to other bilayers, potentially large implications with respect to the relaxivity properties of the extracellular face. It is known that cholesterol incoporation into fully hydrated bilayers decreases lipid lateral diffusion and separates the lipid head groups; this creates a "pocket" in which the cholesterol hydroxyl moiety is at the water-hydrocarbon interface [111]. The creation of these 'pockets' could serve an important role in increasing the timescale for interaction between the membrane and myelinic water. Furthermore, the ordering effects of cholesterol in a membrane [122] have been shown to reduce water diffusion through a bilayer; a property which we've seen is particularly relevant with respect to the resolution of a short T_2 component. The magnitudes of such changes could be relevant; increasing the cholesterol : phospholipid ratio by a factor ~ 1.6 in red blood cells resulted in a 3.5 fold decrease in transmembrane water diffusion, as measured by pulse field gradient NMR [123].

Measures of lipid composition in different CNS regions reveal two noteworthy differences between brain and spinal cord. Firstly, spine myelin has a higher lipid:protein ratio than brain myelin [53, 124]. While interaction with myelin lipid is the dominant factor in determining the interfacial relaxation, that measure was cast over the entire contact area of the myelin sheath and compared to typical protein contributions. The relative contribution of myelin proteins to the interfacial relaxation velocity over the large myelin contact area could be substantial, and any statements correlating an increased lipid:protein ratio with relaxation properties would be largely unsubstantiated, and in fact, could be contraindicated. Secondly, an increase in both cholesterol (~20%) and cerebroside (~20%) has been noted in bovine spinal cord myelin [105], although there is some disagreement in the literature [124]. Nonetheless, these determinations would be consistent with greater MT, shorter T_1, and likely a shorter T_2 in the spinal cord.

Other Magnetic Resonance Correlates of Myelin Chemistry

Although the extent to which regional differences in myelin chemistry would affect the magnetic resonance properties of different CNS regions is unknown, there are other magnetic resonance measurements that correlate with expectations based on chemical content. The linear increase in MT effect with surface hydroxyl groups [111] is likely indicative of the expected effect of other hydrophilic moieties. The suggestion that there may be more hydrophilic groups per unit surface area in spinal myelin is consistent with our (unpublished) measures of MT in bovine spine *in vitro*. Magnetization transfer ratios in spinal cord white matter were approximately twice those measured in *in vitro* human brain with the same sequence (Irene Vavasour, unpublished results).

Furthermore, observations of compartmental T_2 times in the garfish resolved significantly shorter myelinic T_2 times in the CNS (34±5ms) relative to the PNS (49±8ms) [54]. We note here that CNS myelin has 50% more cerebroside [96], and has a greater charge density as measured by Inouye and Kirschner [121, 125]. Indeed, given the well established differences in myelin chemistry between the central and peripheral nervous systems, further study entertaining potential magnetic resonance implications of myelin membrane chemistry should focus on measurements in those two branches of the nervous system.

5.3 Conclusions

This study marks a successful implementation of an IR-CPMG sequence on a phased array coil, for the purposes of quantitative T_2 relaxation measurements in the human spinal cord *in vivo*. Myelin water fractions were resolved along the entire imaged length of the spine, and the regional variations in these measurements were found to be in agreement with expected changes in voxel white matter content. While the values resolved for the short T_2 component "myelin water fraction" were in agreement with supporting *in vitro* work on bovine spine, they are higher than those previously resolved in brain white matter *in vivo*. Some of this increase (~4-11%) could potentially arise from T_1 effects of the IR-CPMG sequence, but it is likely that these higher values also reflect a higher myelin content and / or regional differences in myelin composition and cellular morphometry in the spinal cord.

The potential applications of quantitative T_2 measurement in the spinal cord, both in characterizing disease processes and in monitoring neuro-regenerative therapies, should encourage future research in this area. These endeavours will likely focus on efforts to increase the signal to noise, a parameter which can dramatically affect the resolution of T_2 components through NNLS inversion of multi-echo data. Towards these ends, the movement to higher clinical field strengths, initiated with a successful implementation of a 32 echo Poon-Henkelman CPMG sequence at 3.0T (Shannon Kolind, personal communication), is extremely encouraging.

Other techniques for improving signal to noise that are particularly applicable to spinal imaging include modifications of the inversion recovery pulse to incorporate both T_1 and T_2 selectivity [126]. Replacement of the inversion pulse with a composite 90_x-τ-180_y-τ-90_x preparation sequence can result in significant gains in SNR, given an appropriate interpulse delay τ. Using such a sequence, one would expect signal to noise gains on the order of 30% at a TR that permits the acquisition of 32 echoes [126]; our successful implementation of the sequence on the Phillips Intera 3.0T pulse sequence simulation program may hopefully lead to signal to noise gains on the order of 130% relative to those seen in this study. Simulations suggest this would substantially enhance the resolution and reproducibility of T_2 relaxation derived measurements.

Moreover, recent implementations of single voxel CPMG using projection-presaturation [127] may also find themselves suitable for use in the spinal cord, a structure that would be particularly amenable to isolation with a cylindrical voxel. This technique, free from the constraints imposed by the need to spatially encode the signal that hampers CPMG acquisition in imaging sequences, allows the acquisition of CPMG data at signal to noise ratios and sampling densities typical of *in vitro* work. A recent implementation in skeletal muscle *in vivo* allowed the collection of 2000 echoes at a 1.2ms TE, with an SNR of 3500 [89]. The increased resolution of T_2 characteristics using such techniques could serve to complement results from an imaged based method; albeit with the caveat of a significant MT effect arising from presaturative isolation of a single SC voxel.

A primary motivation behind the project was the potential use of these methods in assessing the spatial and temporal characteristics of a therapeutic immunologically induced demyelinating protocol. Estimates indicate that any measurement technique would need to be sensitive to a localized demyelinated lesion approximately 5mm long, where the affected length is almost completely devoid of myelin (Dr. Jason Dyer, personal communication). At the current FOV and acqusition matrix, this would correspond to approximately 5 voxels in the frequency direction, and about 5 voxels in the phase direction. Visualization of demyelination in a region of this volume would be expected, and should allowing spatial and temporal characteristics to be monitored. An ROI encompassing such a volume (~25 voxels at spinal cord maximum width) is smaller than the ROI that was used in this study (~100 voxels); which under current imaging conditions would produce marginal SNR values that may not be suitable for quantitative assessments.

In the future, however, one can envision a T_2 relaxation protocol in spinal cord injury of great clinical benefit, which would conceivably initiate at the time of injury and terminate upon (hopeful) recovery. Recently demonstrated differences between the T_2 distributions of crushed and cut nerves in PNS [56] indicate that comparison of the size of the myelin component, and the position of the intermediate and long components in injured and normal nerve could be capable of discriminating between nerve that is regenerating (and hence would be contraindicating of treatment), and nerve that is not; these *in vitro* determinations could potentially be measured with PP-CPMG *in vivo*. The spatial and temporal characteristics of a subsequent demyelinating therapy could then be characterized with image-based quantitative T_2 techniques: it is hoped that this study may one day be viewed as a necessary first step towards this potential future implementation of multi-echo T_2 measurement, operating as a window to a remarkable healing process.

References

1. Heimer, L., *The human brain and spinal cord : functional neuroanatomy and dissection guide*. 2nd ed. 1995, New York: Springer-Verlag. xiv, 506 p.
2. Campbell, N.A., *Biology*. 4th ed. Benjamin/Cummings series in the life sciences. 1996, Menlo Park, Calif.: Benjamin/Cummings Pub. Co. xxvii, 1206, [64].
3. Barkovich, A.J., *Concepts of myelin and myelination in neuroradiology*. AJNR Am J Neuroradiol, 2000. **21**(6): p. 1099-109.
4. Hildebrand, C., et al., *Myelinated Nerve-Fibers in the Cns*. Progress in Neurobiology, 1993. **40**(3): p. 319-384.
5. Nelson, D.L., M.M. Cox, and A.L. Lehninger, *Lehninger principles of biochemistry*. 3rd ed. 2000, New York: Worth Publishers. 1 v. (various pagings).
6. Alberts, B., *Molecular biology of the cell*. 4th ed. 2002, New York: Garland Science. xxxiv, 1463, [86].
7. Hodgkin, A.L. and A.F. Huxley, *A quantitative description of membrane current and its application to conduction and excitation in nerve*. J Physiol, 1952. **117**(4): p. 500-44.
8. Hausser, M., *The Hodgkin-Huxley theory of the action potential*. Nat Neurosci, 2000. **3 Suppl**: p. 1165.
9. Keirstead, H.S. and J.D. Steeves, *CNS myelin: Does a stabilizing role in neurodevelopment result in inhibition of neuronal repair after adult injury?* Neuroscientist, 1998. **4**(4): p. 273-284.
10. Keirstead, H.S., et al., *In vivo immunological suppression of spinal cord myelin development*. Brain Research Bulletin, 1997. **44**(6): p. 727-734.
11. Hatten, M., et al., *Neuron-astroglial interactions in vitro and their implications for repair of CNS injury*. Central Nervous System Trauma, 1984. **1**(1): p. 15-27.
12. Nijeholt, G., et al., *Spinal cord magnetic resonance imaging in suspected multiple sclerosis*. European Radiology, 2000. **10**(2): p. 368-376.

13. Mottershead, J.P., et al., *High field MRI correlates of myelin content and axonal density in multiple sclerosis - A post-mortem study of the spinal cord.* Journal of Neurology, 2003. **250**(11): p. 1293-1301.

14. Barkhof, F., *The clinico-radiological paradox in multiple sclerosis revisited.* Current Opinion in Neurology, 2002. **15**(3): p. 239-245.

15. McDonald, W.I., et al., *Recommended diagnostic criteria for multiple sclerosis: Guidelines from the International Panel on the Diagnosis of Multiple Sclerosis.* Annals of Neurology, 2001. **50**(1): p. 121-127.

16. Bot, J.C.J., et al., *Differentiation of multiple sclerosis from other inflammatory disorders and cerebrovascular disease: Valus of spinal MR imaging.* Radiology, 2002. **223**(1): p. 46-56.

17. Bot, J.C.J., et al., *Spinal cord abnormalities in recently diagnosed MS patients.* Neurology, 2004. **62**(2): p. 226-233.

18. Lycklama, G., M.A. van Walderveen, and J.A. Castelijns, *Brain and spinal cord abnormalities in multiple sclerosis: correlation between MRI parameters, clinical subtypes, and symptoms.* Brain, 1998. **121**: p. 687-697.

19. Lycklama, G., et al., *Spinal-cord MRI in multiple sclerosis.* Lancet Neurology, 2003. **2**(9): p. 555-562.

20. Vaithianathar, L., et al., *Magnetic resonance imaging of the cervical spinal cord in multiple sclerosis - A quantitative T-1 relaxation time mapping approach.* Journal of Neurology, 2003. **250**(3): p. 307-315.

21. Bot, J.C.J., et al., *The spinal cord in multiple sclerosis: Relationship of high-spatial-resolution quantitative MR imaging findings to histopathologic results.* Radiology, 2004. **233**(2): p. 531-540.

22. Thorpe, J.W., et al., *Spinal MRI in patients with suspected multiple sclerosis and negative brain MRI.* Brain, 1996. **119**: p. 709-714.

23. Thorpe, J.W., et al., *Spinal-Cord Mri Using Multiarray Coils and Fast Spin-Echo .1. Technical Aspects and Findings in Healthy-Adults.* Neurology, 1993. **43**(12): p. 2625-2631.

24. Korzan, J.R., et al., *In vivo magnetic resonance imaging of the human cervical spinal cord at 3 Tesla.* Journal of Magnetic Resonance Imaging, 2002. **16**(1): p. 21-27.
25. Poon, C.S. and R.M. Henkelman, *Practical T2 Quantitation for Clinical-Applications.* Jmri-Journal of Magnetic Resonance Imaging, 1992. **2**(5): p. 541-553.
26. Poon, C.S. and R.M. Henkelman, *180-Degrees Refocusing Pulses Which Are Insensitive to Static and Radiofrequency Field Inhomogeneity.* Journal of Magnetic Resonance, 1992. **99**(1): p. 45-55.
27. Whittall, K.P., A.L. MacKay, and D.K.B. Li, *Are mono-exponential fits to a few echoes sufficient to determine T-2 relaxation for in vivo human brain?* Magnetic Resonance in Medicine, 1999. **41**(6): p. 1255-1257.
28. Minty, E.P., A. MacKay, and K. Whittall. *Measurement of Myelin Water in Human and Bovine Spinal Cord.* in *ISMRM.* 2002. Honolulu, Hawaii.
29. Laule, C., et al. *Cervical cord abnormalities in primary progressive multiple sclerosis: Atrophy and myelin water changes.* in *ISMRM.* 2004. Kyoto, Japan.
30. Wu, Y., et al. *Quantification of myelin water in human cervical spinal cord in vivo.* in *ISMRM.* 2004. Kyoto, Japan.
31. Yung, A.C., et al. *Measurements of myelin water in rat spinal cord in vivo.* in *ISMRM.* 2004. Kyoto, Japan.
32. McDonald, J.W. and C. Sadowsky, *Spinal-cord injury.* Lancet, 2002. **359**(9304): p. 417-425.
33. Network, T.S.C.I., *Facts and figures at a glance.* 2004, National Spinal Cord Injury Statistical Center. p. http://www.spinalcord.uab.edu/.
34. Saunders, N.S. and K.M. Dziegielewska, *Degeneration and regeneration in the nervous system.* 2000, Amsterdam: T&F STM. 348.
35. Keirstead, H.S., et al., *Axonal Regeneration and Physiological-Activity Following Transection and Immunological Disruption of Myelin within the Hatchling Chick Spinal-Cord.* Journal of Neuroscience, 1995. **15**(10): p. 6963-6974.

36. Dyer, J.K., J.A. Bourque, and J.D. Steeves, *Regeneration of brainstem-spinal axons after lesion and immunological disruption of myelin in adult rat.* Experimental Neurology, 1998. **154**(1): p. 12-22.

37. McGowan, J.C., *Technical issues for MRI examination of the spinal cord.* Journal of the Neurological Sciences, 2000. **172**: p. S27-S31.

38. Purcell, E.M. and T. H.C., *Resonance absorption by nuclear magnetic moments in a solid.* Phys. Rev., 1946. **69**: p. 37-38.

39. Bloch, F., *Nuclear Induction.* Phys. Rev., 1946. **70**: p. 460-474.

40. Xiang, Q.S., *Introduction to MRI*, in *Physics 404 Lecture notes*. 2000.

41. Griffiths, D.J., *Introduction to quantum mechanics*. 1995, Englewood Cliffs, N.J.: Prentice Hall. ix, 394.

42. Haacke, M.E., et al., *Magnetic Resonance Imaging. Physical Priniciples and Sequence Design*. 1999: John Wiley & Sons.

43. Hahn, E.L., *Spin Echoes.* Physical Review, 1950. **80**(4): p. 580-594.

44. Carr, H.Y. and E.M. Purcell, *Effects of Diffusion on Free Precession in Nuclear Magnetic Resonance Experiments.* Physical Review, 1954. **94**(3): p. 630-638.

45. Meiboom, S. and D. Gill, *Modified Spin-Echo Method for Measuring Nuclear Relaxation Times.* Review of Scientific Instruments, 1958. **29**(8): p. 688-691.

46. Whittall, K.P. and A.L. Mackay, *Quantitative Interpretation of Nmr Relaxation Data.* Journal of Magnetic Resonance, 1989. **84**(1): p. 134-152.

47. Menon, R.S., M.S. Rusinko, and P.S. Allen, *Proton Relaxation Studies of Water Compartmentalization in a Model Neurological System.* Magnetic Resonance in Medicine, 1992. **28**(2): p. 264-274.

48. Mackay, A., et al., *In-Vivo Visualization of Myelin Water in Brain by Magnetic-Resonance.* Magnetic Resonance in Medicine, 1994. **31**(6): p. 673-677.

49. Vasilescu, V., et al., *Water Compartments in Myelinated Nerve .3. Pulsed Nmr Results.* Experientia, 1978. **34**(11): p. 1443-1444.

50. Menon, R.S. and P.S. Allen, *Application of Continuous Relaxation-Time Distributions to the Fitting of Data from Model Systems and Excised Tissue.* Magnetic Resonance in Medicine, 1991. **20**(2): p. 214-227.

51. Stewart, W.A., et al., *Spin-Spin Relaxation in Experimental Allergic Encephalomyelitis - Analysis of Cpmg Data Using a Nonlinear Least-Squares Method and Linear Inverse-Theory.* Magnetic Resonance in Medicine, 1993. **29**(6): p. 767-775.

52. Kaneoke, Y., et al., *Spin-Lattice Relaxation-Times of Bound Water - Its Determination and Implications for Tissue Discrimination.* Magnetic Resonance Imaging, 1987. **5**(6): p. 415-420.

53. Norton, W.T. and W. Cammer, *Isolation and Characterization of Myelin*, in *Myelin*, P. Morell, Editor. 1984, Plenum Press: New York. p. 155.

54. Beaulieu, C., F.R. Fenrich, and P.S. Allen, *Multicomponent water proton transverse relaxation and T-2-discriminated water diffusion in myelinated and nonmyelinated nerve.* Magnetic Resonance Imaging, 1998. **16**(10): p. 1201-1210.

55. Does, M.D. and R.E. Snyder, *Multiexponential T-2 relaxation in degenerating peripheral nerve.* Magnetic Resonance in Medicine, 1996. **35**(2): p. 207-213.

56. Webb, S., et al., *Is multicomponent T2 a good measure of myelin content in peripheral nerve?* Magn Reson Med, 2003. **49**(4): p. 638-45.

57. Whittall, K.P., et al., *Normal-appearing white matter in multiple sclerosis has heterogeneous, diffusely prolonged T-2.* Magnetic Resonance in Medicine, 2002. **47**(2): p. 403-408.

58. Laule, C., et al., *Evolution of diffuse and focal magnetization transfer abnormalities in multiple sclerosis.* Neurology, 2002. **58**(7): p. A154-A155.

59. Moore, G.R.W., et al., *The short T2 component is absent in chronically demyelinated plaques in formalin-fixed multiple sclerosis brain.* Neurology, 1999. **52**(6): p. A567-A567.

60. Vavasour, I.M., et al., *A serial magnetic resonance study of multiple sclerosis: T2 relaxation, T1 relaxation and magnetization transfer.* Neurology, 1999. **52**(6): p. A360-A360.

61. Vavasour, I.M., et al., *A comparison between magnetization transfer ratios and myelin water percentages in normals and multiple sclerosis patients.* Magnetic Resonance in Medicine, 1998. **40**(5): p. 763-768.

62. Whittall, K.P., et al., *In vivo measurement of T-2 distributions and water contents in normal human brain.* Magnetic Resonance in Medicine, 1997. **37**(1): p. 34-43.

63. Beaulieu, C. and P.S. Allen, *Determinants of anisotropic water diffusion in nerves.* Magn Reson Med, 1994. **31**(4): p. 394-400.

64. Gulani, V., et al., *Apparent diffusion tensor measurements in myelin-deficient rat spinal cords.* Magn Reson Med, 2001. **45**(2): p. 191-5.

65. Pettigrew, D.B. and K.A. Crutcher, *Myelin contributes to the parallel orientation of axonal growth on white matter in vitro.* BMC Neurosci, 2001. **2**(1): p. 9.

66. Does, M.D., et al., *Multi-component T1 relaxation and magnetisation transfer in peripheral nerve.* Magn Reson Imaging, 1998. **16**(9): p. 1033-41.

67. Gareau, P.J., et al., *Magnetization transfer and multicomponent T2 relaxation measurements with histopathologic correlation in an experimental model of MS.* J Magn Reson Imaging, 2000. **11**(6): p. 586-95.

68. Stanisz, G.J., et al., *MR properties of rat sciatic nerve following trauma.* Magnetic Resonance in Medicine, 2001. **45**(3): p. 415-420.

69. Graham, S.J., P.L. Stanchev, and M.J. Bronskill, *Criteria for analysis of multicomponent tissue T2 relaxation data.* Magn Reson Med, 1996. **35**(3): p. 370-8.

70. Fenrich, F.R.E., C. Beaulieu, and P.S. Allen, *Relaxation times and microstructures.* Nmr in Biomedicine, 2001. **14**(2): p. 133-+.

71. Jones, C.K., *T2 Decay Curve Acquisition and Analysis in MRI*, in *Physics and Astronomy*. 2003, University of British Columbia: Vancouver. p. 162.

72. Crawley, A.P. and R.M. Henkelman, *Errors in T2 Estimation Using Multislice Multiple-Echo Imaging.* Magnetic Resonance in Medicine, 1987. **4**(1): p. 34-47.

73. Vavasour, I.M., et al., *Different magnetization transfer effects exhibited by the short and long T(2) components in human brain.* Magn Reson Med, 2000. **44**(6): p. 860-6.

74. Stanisz, G.J., et al., *Characterizing white matter with magnetization transfer and T(2).* Magn Reson Med, 1999. **42**(6): p. 1128-36.

75. Crawley, A.P., R.M. Henkelman, and M.J. Bronskill, *Artifact Suppression in Multislice T2 Imaging.* Medical Physics, 1986. **13**(4): p. 571-571.

76. Woessner, D.E., *Effects of Diffusion in Nuclear Magnetic Resonance Spin-Echo Experiments.* Journal of Chemical Physics, 1961. **34**(6): p. 2057-&.

77. Hennig, J., *Multiecho Imaging Sequences with Low Refocusing Flip Angles.* Journal of Magnetic Resonance, 1988. **78**(3): p. 397-407.

78. Ross, J.S., *Newer sequences for spinal MR imaging: Smorgasbord or succotash of acronyms?* American Journal of Neuroradiology, 1999. **20**(3): p. 361-373.

79. Sternin, E., *Data acquisition and processing: a systems approach.* Review of Scientific Instruments, 1986(56): p. 2043-3029.

80. Meiboom, G. and D. Gill, *Modified spin echo method for measuring relaxation times.* Review of Scientific Instruments, 1958(29): p. 688-691.

81. Jones, C.K., et al., *Linear combination of multiecho data: Short T-2 component selection.* Magnetic Resonance in Medicine, 2004. **51**(3): p. 495-502.

82. Vavasour, I.M., *Magnetic Resonance of Human and Bovine Brain*, in *Physics*. 1998, University of British Columbia: Vancouver. p. 124.

83. Enestrom, S. and A. Hamberger, *Respiration and mitochondrial content in single neurons of the supraoptic nucleus. A correlative study in osmotic stress.* J Cell Biol, 1968. **38**(3): p. 483-93.

84. Baba, Y., et al., *Time after excision and temperature alter ex vivo tissue relaxation time measurements.* J Magn Reson Imaging, 1994. **4**(5): p. 647-51.

85. Chandross, R.J., R.S. Bear, and R.L. Montgomery, *An X-ray diffraction comparison of myelins from the human nervous system.* J Comp Neurol, 1978. **177**(1): p. 1-9.

86. Does, M.D. and R.E. Snyder, *T2 relaxation of peripheral nerve measured in vivo.* Magn Reson Imaging, 1995. **13**(4): p. 575-80.

87. Estilaei, M., et al., *In vitro measurements of water content and T-2 relaxation times in lung using a clinical MRI scanner.* Jmri-Journal of Magnetic Resonance Imaging, 1999. **9**(5): p. 699-703.

88. Riley, H.A., *An atlas of the basal ganglia, brain stem and spinal cord based on myelin stained material.* 1943, Baltimore: Williams and Wilkins Company. 708.

89. Zuleger, S. and J. Staubesand, *Atlas of the central nervous system in sectional planes : selected myelin stained sections of the human brain and spinal cord.* 1977, Baltimore: Urban & Schwarzenberg. 106.

90. Haines, D.E., *Neuroanatomy : an atlas of structures, sections, and systems.* 6th ed. 2004, Philadelphia: Lippincott Williams & Wilkins. xii, 319.

91. Fix, J.D. and C.S. Punte, *Atlas of the human brain stem and spinal cord.* 1981, Baltimore: University Park Press. [92].

92. Perneger, T.V., *What's wrong with Bonferroni adjustments.* Bmj, 1998. **316**(7139): p. 1236-8.

93. Henkelman, R.M., *Measurement of signal intensities in the presence of noise in MR images.* Med Phys, 1985. **12**(2): p. 232-3.

94. Does, M.D. and J.C. Gore, *Rapid acquisition transverse relaxometric imaging.* J Magn Reson, 2000. **147**(1): p. 116-20.

95. Does, M.D. and J.C. Gore, *Compartmental study of T-1 and T-2 in rat brain and trigeminal nerve in vivo.* Magnetic Resonance in Medicine, 2002. **47**(2): p. 274-283.

96. Morell, P., *Myelin Formation, Structure, and Biochemistry*, in *Basic Neurochemistry*, G.J. Siegal, Editor. 1999, Lippincot-Raven: Philidelphia, PA.

97. Smith, M.E. and L.M. Sedgewick, *Studies of the mechanism of demyelination. Regional differences in myelin stability in vitro.* J Neurochem, 1975. **24**(4): p. 763-70.

98. Zimmerman, A.W., et al., *Characterization and protein analysis of myelin subfractions in rat brain: developmental and regional comparisons.* J Neurochem, 1975. **25**(6): p. 749-57.

99. Bergers, E., et al., *Axonal damage in the spinal cord of MS patients occurs largely independent of T2 MRI lesions.* Neurology, 2002. **59**(11): p. 1766-1771.

100. Graf von Keyserlingk, D. and U. Schramm, *Diameter of axons and thickness of myelin sheaths of the pyramidal tract fibers in the adult human medullary pyramid.* Anat Anz, 1984. **157**(2): p. 97-111.

101. Evangelou, N., et al., *Regional axonal loss in the corpus callosum correlates with cerebral white matter lesion volume and distribution in multiple sclerosis.* Brain, 2000. **123 (Pt 9)**: p. 1845-9.

102. Hildebrand, C. and R. Hahn, *Relation between myelin sheath thickness and axon size in spinal cord white matter of some vertebrate species.* J Neurol Sci, 1978. **38**(3): p. 421-34.

103. Stidworthy, M.F., et al., *Quantifying the early stages of remyelination following cuprizone-induced demyelination.* Brain Pathol, 2003. **13**(3): p. 329-39.

104. Remahl, S. and C. Hildebrand, *Changing relation between onset of myelination and axon diameter range in developing feline white matter.* J Neurol Sci, 1982. **54**(1): p. 33-45.

105. Amaducci, L., A. Pazzagli, and G. Pessina, *The relation of proteolipids and phosphatidopeptides to tissue elements in the bovine nervous system.* J Neurochem, 1962. **9**: p. 509-18.

106. Finkelstein, A., *Water and nonelectrolyte permeability of lipid bilayer membranes.* J Gen Physiol, 1976. **68**(2): p. 127-35.

107. Menon, R.S., M.S. Rusinko, and P.S. Allen, *Multiexponential Proton Relaxation in Model Cellular-Systems.* Magnetic Resonance in Medicine, 1991. **20**(2): p. 196-213.

108. Koenig, S.H., *Cholesterol of Myelin Is the Determinant of Gray-White Contrast in Mri of Brain.* Magnetic Resonance in Medicine, 1991. **20**(2): p. 285-291.

109. Koenig, S.H., et al., *Relaxometry of Brain - Why White Matter Appears Bright in Mri.* Magnetic Resonance in Medicine, 1990. **14**(3): p. 482-495.

110. Kucharczyk, W., et al., *Relaxivity and Magnetization-Transfer of White-Matter Lipids at Mr-Imaging - Importance of Cerebrosides and Ph.* Radiology, 1994. **192**(2): p. 521-529.

111. Ceckler, T.L., et al., *Dynamic and Chemical Factors Affecting Water Proton Relaxation by Macromolecules.* Journal of Magnetic Resonance, 1992. **98**: p. 637-645.

112. Morell, P., ed. *Myelin*. 2nd ed. 1984, Plenum Press: New York. 545.

113. Uyemura, K., C. Tobari, and S. Hirano, *Purifications and properties of basic proteins in pig spinal cord and peripheral nerve.* Biochim Biophys Acta, 1970. **214**(1): p. 190-7.

114. Uyemura, K., et al., *Comparative studies on the myelin proteins of bovine peripheral nerve and spinal cord.* J Neurochem, 1972. **19**(11): p. 2607-14.

115. Lees, M.B. and S.A. Paxman, *Myelin proteins from different regions of the central nervous system.* J Neurochem, 1974. **23**(4): p. 825-31.

116. Morell, P., R. Lipkind, and S. Greenfield, *Protein composition of myelin from brain and spinal cord of several species.* Brain Res, 1973. **58**(2): p. 510-4.

117. Stoffel, W., H. Hillen, and H. Giersiefen, *Structure and molecular arrangement of proteolipid protein of central nervous system myelin.* Proc Natl Acad Sci U S A, 1984. **81**(16): p. 5012-6.

118. Beniac, D.R., et al., *Three-dimensional structure of myelin basic protein. I. Reconstruction via angular reconstitution of randomly oriented single particles.* J Biol Chem, 1997. **272**(7): p. 4261-8.

119. Korb, J.P. and R.G. Bryant, *Magnetic field dependence of proton spin-lattice relaxation times.* Magn Reson Med, 2002. **48**(1): p. 21-6.

120. Koenig, S.H., *Molecular basis of magnetic relaxation of water protons of tissue.* Academic Radiology, 1996. **3**(7): p. 597-606.

121. Inouye, H. and D.A. Kirschner, *Membrane interactions in nerve myelin: II. Determination of surface charge from biochemical data.* Biophys J, 1988. **53**(2): p. 247-60.

122. Nezil, F.A. and M. Bloom, *Combined influence of cholesterol and synthetic amphiphillic peptides upon bilayer thickness in model membranes.* Biophys J, 1992. **61**(5): p. 1176-83.

123. Waldeck, A.R., et al., *Effects of cholesterol on transmembrane water diffusion in human erythrocytes measured using pulsed field gradient NMR.* Biophys Chem, 1995. **55**(3): p. 197-208.

124. Svennerholm, L., et al., *Membrane lipids of human peripheral nerve and spinal cord.* Biochim Biophys Acta, 1992. **1128**(1): p. 1-7.

125. Inouye, H. and D.A. Kirschner, *Membrane interactions in nerve myelin. I. Determination of surface charge from effects of pH and ionic strength on period.* Biophys J, 1988. **53**(2): p. 235-45.

126. Wong, E.C., et al., *T(1) and T(2) selective method for improved SNR in CSF-attenuated imaging: T(2)-FLAIR.* Magn Reson Med, 2001. **45**(3): p. 529-32.

127. Saab, G., R.T. Thompson, and G.D. Marsh, *Multicomponent T-2 relaxation of in vivo skeletal muscle.* Magnetic Resonance in Medicine, 1999. **42**(1): p. 150-157.